Sizing of the Series Hybrid-electric Propulsion System of General Aviation Aircraft

A thesis accepted by the Faculty of Aerospace Engineering and Geodesy of the University of Stuttgart in partial fulfilment of the requirements for the degree of Doctor of Engineering Sciences (Dr.-Ing.)

by
Ingmar Geiß
born in Jena

main referee: Prof. Dipl.-Ing. Rudolf Voit-Nitschmann
co-referee: Prof. Dr.-Ing. Stephan Staudacher

Date of defence: 6th October 2020

Institute of Aircraft Design
University of Stuttgart
2020

Danksagung

Die vorliegende Arbeit entstand während meiner Zeit als wissenschaftlicher Mitarbeiter am Institut für Flugzeugbau der Universität Stuttgart.

Mein großer Dank gilt meinem Doktorvater Herrn Professor Dipl.-Ing. Rudolf Voit-Nitschmann, der von Beginn an den Entstehungsprozess der Arbeit begleitet hat. Als Hauptberichter stand er mir bei auftretenden Problemen aus dem Flugzeugvorentwurf mit Rat und Tat zur Seite. Ebenso möchte ich mich ganz herzlich bei meinem Mitberichter Herrn Professor Dr.-Ing. Stephan Staudacher bedanken, der nicht nur im Bereich der Luftfahrtantriebe unterstützte, sondern auch in vielen fruchtbaren Gesprächen und Diskussionen zum Gelingen dieser Arbeit wesentlich beitrug.

Mein besonderer Dank geht an meine Frau Lisa, die mit ihrer Unterstützung maßgeblich zu dieser Arbeit beigetragen hat. Meinen Eltern sowie meinen Freunden möchte ich außerdem für das Korrekturlesen danken. Zudem bedanke ich mich herzlich bei Prof. Dr.-Ing. Andreas Strohmayer, den Kollegen vom Institut für Flugzeugbau und im Besonderen beim Team der bemannten Flugzeugprojekte für die tolle Arbeitsatmosphäre am Institut.

Contents

Abstract

The scope of this thesis is to investigate how series hybrid-electric propulsion systems need to be sized to lower the fuel consumption of aircraft which are typically used in general aviation. Therefore, the characteristics of the individual propulsion elements are identified and suitable trends for mass, power and efficiency are derived from data of existing components. Additionally, part load efficiency and altitude characteristics are investigated. Statistic methods are applied to ensure significant trends.

The fuel consumption of an aircraft depends on the efficiency of the propulsion system as well as on the aircraft's mass and aerodynamic drag. Hence, the influence of an increased propulsion system mass on the aircraft mass and the parasitic and induced drag is investigated. Additionally, the required power and energy reserves are determined to compensate a failure of a combustion engine or a battery pack during take-off. In a further scenario, it is investigated which reserve is required after such component failure during cruise flight. Therefore, an evaluation is carried out to determine the probability of an aircraft position during cruise flight to be within a certain distance to a suitable diversion airport. The study is carried out for Europe and the USA.

The derived trends for the propulsion components, the interactions with aircraft mass and drag as well as the influence of a failure of a propulsion component are implemented into a sizing program in MATLAB. With this program, optimized design points can be determined for the hybrid-electric propulsion system. The type of the combustion engines is varied as well as the type and mass of the battery system in order to identify the propulsion system with the lowest fuel consumption. The optimization of the propulsion system for a 4-seat hybrid-electric aircraft with a cruise speed of 120 knots ($\sim$ 220 km/h) and a range of 800 km results in a fuel burn reduction of 21 % in comparison to a modern, conventional aircraft. An optima is found for a propulsion system, which consists of a diesel engine, sized approximately to the required climb flight power, and a battery system, which provides additional power during take-off. Additionally, the battery system is capable to compensate the power loss after a failure of the combustion engine during take-off. The fuel burn reduction is driven by an aerodynamically improved airframe and a more efficient propeller integration, where the electric motor is integrated in the vertical stabilizer of the aircraft. The combustion engine is used to generate electricity and is placed in the fuselage near the aircraft's center of gravity. A sensitivity study is carried out in order to determine the influence of improvements on component level on the fuel consumption and mass of the hybrid-electric aircraft. As a result, it can be e.g. quantified which influence an increased specific power of electric machines has on aircraft level.

The sizing algorithm for the propulsion system and corresponding aircraft parameters is then applied to a 9-seat aircraft with a speed in cruise flight of 220 knots ($\sim$ 400 km/h) and a range of 3,200 km. The number of the combustion engines is introduced as a further optimization parameter. A reduction in fuel burn of 9 % can be achieved if two diesel engines are applied to drive the generators of the hybrid-electric system. The fuel burn can be even reduced by 24 % if a mass-optimized diesel engine is applied, which is currently developed by the company Safran S.A. The reduction in fuel burn is referenced to the most modern conventional aircraft, which is powered by a turboprop engine. The hybrid-electric aircraft design shows a significantly increased take-off mass, which is however overcompensated by an aerodynamically improved propeller integration and an increased efficiency of the diesel engine. Similarly, a sensitivity analysis is carried out to identify promising developments on component level in order to reduce fuel consumption on aircraft level further.

In order to increase confidence in the gained results of the preliminary designed hybrid-electric aircraft, the data of the conventional reference aircraft are re-calculated with the same sizing algorithm. Furthermore, the estimation of component mass is adjusted with data from an existing aircraft. Similarly, an estimation of the aerodynamic drag is calibrated with a drag polar obtained of the electric aircraft "e-Genius".

Kurzfassung

In der vorliegenden Arbeit wird untersucht, wie serielle hybrid-elektrische Antriebssysteme gestaltet sein müssen, um den Kraftstoffverbrauch von Flugzeugen der allgemeinen Luftfahrt zu senken. Dafür werden die einzelnen Komponenten des Antriebssystems analysiert und Trends für Masse, Leistung und Effizienz aus bestehenden Daten abgeleitet. Zudem werden das Teillastverhalten und die Höhenabhängigkeit der Komponenten betrachtet. Die Signifikanz der abgeleiteten Trends wird mit statistischen Methoden nachgewiesen.

Der Kraftstoffverbrauch eines Flugzeugs wird von der Effizienz des Antriebssystems beeinflusst, aber auch vom aerodynamischen Widerstand und dem Gewicht des Flugzeugs maßgeblich mitbestimmt. Daher wird untersucht, wie sich ein erhöhtes Gewicht des Antriebssystems auf die Masse und den parasitären und auftriebsabhängigen Widerstand des Flugzeugs auswirkt. Zusätzlich werden die benötigten Leistungs- und Energiereserven bestimmt, um den Ausfall eines Verbrennungsmotors oder einer Batterieeinheit während des Startvorgangs zu kompensieren. Ein weiteres Szenario wird untersucht, bei dem ein solcher Ausfall während des Reiseflugs auftritt und eine Reserve notwendig ist, um einen Ausweichflugplatz zu erreichen. Dafür wird in einer Studie die Wahrscheinlichkeit bestimmt, mit welcher sich das Flugzeug im Reiseflug innerhalb einer bestimmten Distanz zu einem geeigneten Ausweichflugplatz befindet. Die Untersuchung wird für Flugzeugpositionen und Flugplätze in Europa und in den USA durchgeführt.

Die abgeleiteten Trends der Antriebskomponenten sowie die Interaktion zwischen Flugzeuggewicht, aerodynamischen Widerstand und Ausfällen im Antriebssystem werden in einem Entwurfsprogramm implementiert, welches in MATLAB programmiert ist. Mit diesem kann ein optimierter Auslegungspunkt für das hybrid-elektrische Antriebssystem bestimmt werden. Die Art der Verbrennungskraftmaschinen sowie die Leistung und Masse des Batteriesystems werden dabei variiert, um das hybrid-elektrische Antriebssystem mit dem geringsten Kraftstoffverbrauch zu identifizieren. Wird die Optimierung für ein viersitziges hybrid-elektrisches Flugzeug mit einer Reisegeschwindigkeit von 120 Knoten ($\sim$220 km/h) und einer Reichweite von 800 km durchgeführt, kann eine Verringerung des Kraftstoffverbrauchs um 21 % erreicht werden, wenn als Referenz ein modernes, konventionell angetriebenes Flugzeug dient. Für das betrachtete Flugzeug wird das Optimum bei einem Antriebssystem gefunden, das aus einem Dieselmotor, der circa den Leistungsbedarf des Steigflugs deckt, und aus einem Batteriesystem besteht. Dieses stellt zusätzliche Leistung und Energie im Startvorgang bereit und ist in der Lage einen Ausfall des Verbrennungsmotors zu kompensieren. Der reduzierte

Kraftstoffverbrauch ist maßgeblich beeinflusst von einer aerodynamisch günstigeren Rumpfform und einer effizienteren Propellerintegration, wobei der elektrische Motor im Seitenleitwerk installiert ist. Die Verbrennungskraftmaschine, die im Rumpf nahe am Flugzeugschwerpunkt verbaut ist, wird genutzt, um einen Generator anzutreiben, der elektrische Leistung erzeugt. Nachfolgend wird eine Sensitivitätsanalyse durchgeführt, um den Einfluss zu bestimmen, den Verbesserungen im Bereich der Antriebskomponenten auf den Kraftstoffverbrauch und die Abflugmasse des Flugzeugs haben. So kann z.B. quantifiziert werden, welchen Einfluss eine verbesserte Leistungsdichte von elektrischen Motoren auf Flugzeugebene hat.

Die Entwurfsrechnung wird im Anschluss auf ein neunsitziges Flugzeug mit einer Reisegeschwindigkeit von 220 Knoten (∼400 km/h) und einer Flugreichweite von 3200 km angewendet. Als zusätzlicher Optimierungsparameter wird dabei die Anzahl der Verbrennungskraftmaschinen eingeführt. Der Kraftstoffverbrauch kann um 9 % verringert werden, wenn zwei Dieselmotoren eingesetzt werden, die Generatoren antreiben. Eine Reduktion um 24 % wird erreicht, wenn ein gewichtsoptimierter Dieselmotor eingesetzt wird, den die Firma Safran S.A. aktuell entwickelt. Die Kraftstoffersparnis bezieht sich dabei auf das modernste, konventionell angetriebene Flugzeug, welches mit einem Turboprop-Triebwerk und gleicher Flügelspannweite ausgestattet ist. Die hybrid-elektrischen Flugzeuge besitzen dabei eine signifikant höhere Abflugmasse, welche jedoch überkompensiert wird von einer günstigeren Propellerintegration und einer erhöhten Effizienz des Dieselmotors. Eine Sensitivitätsanalyse wird durchgeführt, um Entwicklungsrichtungen auf Komponentenebene zu identifizieren, die den Kraftstoffverbrauch auf Flugzeugebene weiter reduzieren.

Um die Plausibilität der Rechnung zu gewährleisten, werden die verwendeten, konventionellen Vergleichsflugzeuge mit der gleichen Entwurfsrechnung, die auch für die Optimierung verwendet wird, nachgerechnet. Zudem wird die Zusammensetzung der Flugzeugleermasse mit den Daten eines bestehenden Flugzeugs kalibriert. Weiterhin wird die Berechnung der Widerstandspolaren mit Messdaten, die in der Erprobungskampagne des Flugzeugs „e-Genius“ gewonnen wurden, abgeglichen.

List of Figures

List of Tables

Nomenclature

Symbols

b	Wingspan	[m]
C_{Earth}	Circumference of Earth	[km]
C_{exp}	Proportionality factor	[-]
C_{fe}	Flat-plat skin friction coefficient	[-]
c_D	Drag coefficient	[-]
c_{D0}	Parasitic drag coefficient	[-]
$c_{D0,c}$	Component parasitic drag coefficient	[-]
$c_{D,misc}$	Drag coefficient for miscellaneous drag	[-]
$c_{D,LP}$	Drag coefficient for leakage and protuberance	[-]
ci	Confidence interval	
c_L	Lift coefficient	[-]
c_P	Specific heat capacity	[$\mathrm{J/kg \cdot K}$]
D	Aerodynamic drag	[N]
D_0	Parasitic drag	[N]
D_i	Drag due to lift	[N]
d	Length of great circle arc	[km] or [NM]
E	Energy	[Wh]
E_s	Mass specific energy	[$\mathrm{Wh/kg}$]
e	Oswald factor	[-]
F	Cumulative frequency	[-]
FF_c	Component form factor	[N]
f	Fuel consumption per passenger and per 100 km	[$\mathrm{kg/100\,km}$]
f_i	Reduction factors	[-]
g	Acceleration of gravity	[$\mathrm{m/s^2}$]
H	Flight altitude	[m] or [ft]
H_{crit}	Critical flight altitude for piston engines	[m] or [ft]
Δh_t	Specific enthalpy	[$\mathrm{J/kg}$]
I	Electrical current	[A]
I_N	Nominal electrical current	[A]
k	Drag due to lift factor	[-]
k_{TO}	Take-off parameter	[$\mathrm{m^3 \cdot W/kg^2}$]

k_p	Factor for lift-dependent drag of two-dimensional airfoil	[-]
k_β	Number of regression coefficients	[-]
$^{L}/_{D}$	Lift-to-drag-ratio	[-]
$M(x)$	Number of data points below the threshold x	[-]
m	Mass	[kg]
$m_{A/C}$	Momentary mass of the aircraft in flight	[kg]
m_{MTO}	Maximum take-off mass	[kg]
$m_{s,Cable}$	Length specific mass of electric cable	[kg/m]
$\Delta m_{Bat,i}$	Required battery mass for flight segment i	[kg]
$\Delta m_{Fuel,i}$	Required fuel mass for flight segment i	[kg]
n	Sample size	[-]
n_{Bat}	Number of battery packs	[-]
n_{ICE}	Number of combustion engines	[-]
P	Power	[W]
p_0	Coefficient of battery cell characteristic	[kW/kg]
p_1	Coefficient of battery cell characteristic	[kW/Wh]
P_s	Mass specific power of propulsion component	[$^{\mathrm{W}}/_{\mathrm{kg}}$]
P_{sh}	Shaft power of electric motor driving a propeller	[W]
$p_{sh,Cruise}$	Mass specific shaft power required in cruise flight	[$^{\mathrm{W}}/_{\mathrm{kg}}$]
$\left({}^{P_{max}}/_{m_{MTO}}\right)$	Power loading on aircraft level, referenced to propeller shaft	[$^{\mathrm{W}}/_{\mathrm{kg}}$]
Q_c	Component interference factor	[-]
q	Dynamic pressure	[Pa]
R	Aircraft range	[km] or [NM]
S_{HTP}	Reference area of horizontal stabilizer	[m^2]
S_{TO}	Battery power split at take-off	[-]
S_{VTP}	Reference area of vertical stabilizer	[m^2]
S_w	Wing reference area	[m^2]
$S_{wet,c}$	Wetted surface of component	[m^2]
$\boldsymbol{se}$	Matrix containing standard deviations	
se_i	Diagonal elements of the matrix $\boldsymbol{se}$	
s_{TOFL}	Take-off field length	[m]
T	Temperature	[K]
T_0	Ambient temperature	[K]
T_{t4}	Total temperature between combustion chamber and turbine	[K]

ΔT	Temperature difference	[K]
t	Time	[s]
Δt_i	Duration for segment i	[s]
t_s	Student's inverse cumulative distribution function	[-]
$t\text{-}test$	Numeric value of t-test	[-]
U	Voltage	[V]
V	Volume	[m^3]
v	True airspeed of aircraft	[m/s]
$\boldsymbol{X}$	Design matrix	
$\boldsymbol{X^t}$	Transposed design matrix	
$\boldsymbol{X^{-1}}$	Inverse of design matrix	
$\boldsymbol{x}$	Vector of predictor values	
$\boldsymbol{x^t}$	Transposed vector of predictor values	
x_i	Elements of the vector $\boldsymbol{x}$	
$\boldsymbol{y}$	Response vector	
y_i	Elements of the vector $\boldsymbol{y}$	

Greek symbols

α	Significance level	[-]
α_{Deg}	Capacity fade factor of battery cells	[-]
α_{Int}	Integration factor of battery cells	[-]
$\boldsymbol{\beta}$	Vector of regression coefficient	
β_i, γ_i	Coefficients of linear regression	
γ	Climb angle	[rad]
δ	Drag increase due to non-elliptic lift distribution	[-]
ζ	Angle of great circle	[°]
η	Efficiency	[-]
η_I	Efficiency of propeller integration	[-]
η_P	Efficiency of propeller	[-]
η_{P+I}	Product of efficiency propeller and its integration	[-]
Λ	Aspect ratio of wing	[-]
λ	Air-fuel ratio	[-]
ξ_{Bat}	Battery mass fraction	[-]
ξ_{Fuel}	Fuel mass fraction	[-]
π	Mathematical constant π	[-]
ρ	Air density	[$^{kg}/_{m^3}$]
ρ_0	Standard air density according to ISA at 15°C and H = 0 m	[$^{kg}/_{m^3}$]
$\rho_{Radiator}$	Volumetric density of radiator	[-]
σ	Standard deviation	
ϕ	Latitude	[°]
ψ	Longitude	[°]

Indices

Bat	Battery
EM	Electric motor including its inverter
EM,MCP	Maximum continuous power of electric machine
Gen	Generator including its converter
GT	Gas turbine
HTP	Horizontal tail plane
ICE	Internal combustion engine
TO	Take-off
PD	Power distribution (of electric power)
Prop	Propeller
RPM	Revolutions per minute
sh	Shaft of electric motor driving propeller
VTP	Vertical tail plane

Abbreviations

AIAA	American Institute of Aeronautics and Astronautics
CFD	Computational fluid dynamics
CS	Certification specifications
CO_2	Carbon dioxide
ECU	Electronic control unit
HPDE	High Power Density Engine
ICE	Internal combustion engine
ISA	International standard atmosphere
NASA	National Aeronautics and Space Administration
OEI	One engine inoperative
OPR	Overall pressure ratio
TC	Type certificate
TET	Turbine entry temperature

Chapter 1

Introduction

An energy-efficient aircraft contributes to resource conservation and to the reduction of carbon dioxide emissions. General aviation aircraft, which are driven by electric motors, need in certain applications less shaft power than equivalent aircraft, which are driven by combustion engines. However, the disadvantage of purely battery-powered electric aircraft is the low maximum range, which results from the low mass specific energy of the present rechargeable batteries ($\sim$ 260 Wh/kg) [1]. This specific energy is significant lower than the specific energy of liquid fuels ($\sim$ 11,900 Wh/kg) [2]. In order to achieve an energy-efficient aircraft with sufficient range, a combination of an electrically propelled airframe with a generator system containing a conventional internal combustion engine is a promising solution, where the aim of the aircraft design is to combine the advantages of both systems.

The sizing of a hybrid-electric propulsion system possesses a high degree of design parameters and configurations. Several types of internal combustion engines with different characteristics can be applied. E.g. a diesel engine has a high degree of efficiency, but weighs more than a gasoline engine [3] and considerably more than an aviation gas turbine, if engines with similar power ratings of about 200 kW are compared. As a result, either a heavy internal combustion engine system with a high degree of efficiency or a light system with a low degree of efficiency can be installed. Furthermore the combustion engine can be sized to the aircraft's take-off power or it can be downsized to cruise power. In this case, more power and energy from the battery system is required for take-off and climb, resulting in a heavier battery system. For the battery system different types of battery cells are available, which either possess an increased mass specific energy or an increased mass specific power. As the amount of propulsion components increases, component failures have to be taken into account in order to achieve an Equivalent Level of Safety compared to existing conventional aircraft. These required reserves, which are necessary to compensate failures of propulsion components, affect the mass of the propulsion system and consequently the aircraft's mass and fuel burn. The task of aircraft designers is to find optima for these new degrees of freedom and to identify synergistic combinations for the propulsion system.

Chapter 2

State of the art

2.1 Impact of electric motors on aircraft design

In table 2.1 an exemplary comparison is given for the mass and the volume of a modern piston engine and an electric motor. The motors are applied in general aviation aircraft and belong to the power class of 70 kW. It can be observed that the electric motor is lighter and more compact than the piston engine with the equivalent power rating. As a result, it is feasible to place the electric motor at positions where installation space would not be sufficient for the piston engine. Furthermore, the electric motor can be integrated further away from the airplane's center of gravity, as it has less impact on the weight and balance of the aircraft. Several realized aircraft[1] exploit these advantages by integrating an electric motor in the vertical tail. If a piston engine would be placed in the vertical stabilizer, the wing would have to be positioned backwards in order to achieve a correct position of the centre of gravity. Consequently, the lever arms of the stabilizers decrease and their surfaces increase [4], which leads to a higher wetted area and more drag [5]. Further, the engine nacelle has to be significantly larger as the combustion engine with its auxiliary systems requires more volume. As a result, the integration efficiency of the propeller decreases [5]. The described consequences can be observed in the amphibian airplane "Seawind 300C". A different approach was realized with the first version of the aircraft "Pöschel P 300" in 1971. A piston engine was installed in the fuselage near the aircraft's center of gravity and the mechanical power was transferred by a shaft system to a propeller installed in the vertical tail. The P 300 was tested in flight, but the shaft system proved to be heavy and difficult in operation due to temperature limitations of its angular gears.[2] As a result, the shaft system was removed from the aircraft. The electric motor is a novel element in aircraft design, possesses particular characteristics and has already enabled unique aircraft layouts for one and two-seat aircraft.

---

[1] e.g.: Sunseeker II, icaré 2, Sunseeker Duo and e-Genius

[2] G. Pöschel, personal communication, 7th July 2017

Type	**Model**	**Power**	**Mass**	**Volume**
Gasoline piston engine	Rotax 912 iS Sport [6]	73.5 kW	72 kg	$\sim$ 180 liter
Electric motor	Siemens SP70D [7]	70 kW	26 kg	$\sim$ 18 liter

Table 2.1: Exemplary comparison of a piston engine to an electric motor

According to [8] 92 % of the piston engine aircraft sold worldwide from 1995 to 2018 had a single combustion engine installed and 8 % were equipped with two piston engines. One reason for the low number of installed engines is the negative influence of an increased number of combustions engines on the maintenance cost, which is considered on preliminary aircraft design level by different methods e.g. AEA1989 in [9] or [4]. As electric motors possess fewer components to be prone to wear, reduced maintenance effort can be expected. The data presented in [10] indicates that an automotive electric motor including its power electronics possesses one fourth of the maintenance cost compared to a conventional combustion engine. Furthermore, the number of auxiliary systems, which are necessary to operate an electric motor is reduced as no exhaust system, no air filters and no firewalls are necessary. This lowers the effort to integrate motors in unconventional positions of the aircraft. As a result of the lowered maintenance effort and the reduced number of auxiliary systems it may be economically feasible to propel a general aviation aircraft with more than two motors.

Several preliminary aircraft research projects, described in section 2.2, aim to exploit the described advantages and seek to leverage aerodynamic benefits by integrating motors at unconventional positions. The associated research in the aerodynamic effects has begun initially unrelated to the consideration of electrically propelled aircraft. The following approaches are pursued:

Wing tip mounted propellers

With wing tip mounted propellers the wake of the wing shall be influenced through a counter-rotating motion. Propellers mounted to wing tips were investigated already in 1967, where [11] found that a wing tip mounted propeller, turning in opposite direction to that of the wing vortex, increases the maximum lift coefficient and decreases the wing drag. In 1987, [12] investigated how a pusher turbo-prop engine can be installed at a wing tip to increase propulsive efficiency and reduce induced wing drag. In 2018, [13] determined in wind tunnel tests, that wing tip propellers in tractor configuration lead to a drag reduction from 5 % to 15 % compared to a conventional wing. In 2019, CFD simulations determined that pusher wing tip propellers increase the propulsive efficiency of the propeller by 7.5 % to 16 % depending on the investigated thrust level [14].

Distributed propulsion on wing
[15] investigated the increased lift of a wing, which is exposed to a propeller slipstream. This effect is utilized in [16], where propellers are investigated, which are distributed along the wingspan and used as a high-lift system. In [17] the results of a computational CFD simulation indicate that the maximum lift coefficient of a wing equipped with flaps can be raised from $c_{L,max} = 2.6$ to $c_{L,max} = 4.4$ by distributing propellers along the wingspan. This increased maximum lift coefficient can be used to reduce the wing size, which is necessary to achieve a required stall speed.

Propulsive fuselage
The propulsive efficiency shall be increased, as the slowed down boundary layer of the fuselage is accelerated by a fan installed in the rear part of the fuselage. The results from [18] show that compared with a propeller installed in a turbo-prop nacelle, the suggested fuselage fan possesses an efficiency which is increased by 4 to 6 %. In [19] two different approaches are investigated: in the first, the rear fan is used solely to fill the wake of the fuselage. In the second approach, the rear fan fills the wake of the fuselage and provides additionally the required thrust for flight. Power savings up to 10% were identified relative to conventional podded power plants sized for identical fan inlet areas. Different forms of technical implementation are summarized in [20], both with combustion engines or electric motors.

Propeller integrated into the vertical stabilizer
By integrating the motor in the vertical stabilizer, the integration efficiency is increased, higher propeller diameters can be realized and the size and weight of the landing gear can be reduced. As a result the required shaft power for a sustained flight is lowered [21].

2.2 Research in hybrid-electric aircraft design

Several aircraft design research projects aim to identify synergistic benefits between the described effects and the different propulsion components on preliminary aircraft design level. The NASA investigates distributed electric propulsion with the demonstrator "X-57 Maxwell" shown in Fig. 2.1. The aircraft features propeller at the wing tips as well as span-wise distributed propellers, which are acting as high-lift propellers.

Figure 2.1: Aircraft concept "X-57 Maxwell" in its "Mod 4"-phase by NASA, image source: [22]

With the latter a maximum lift coefficient of at least $c_{L,max} = 3.95$ shall be achieved on aircraft level according to [17]. Consequently, less wing size is needed to achieve the required stall speed of 58 knots and the wing reference area can be reduced in size. As a result, the maximum lift-to-drag ratio L/D is shifted towards the cruise speed, giving the aircraft an aerodynamic advantage over its conventional reference aircraft "Tecnam P2006T". According to [22] this increases L/D in cruise flight in the order of magnitude of 35 %. The smaller wetted area of the wing reduces parasitic drag whereas the numerous motor nacelles increase the parasitic drag. The wing tip mounted propellers of "X-57 Maxwell" shall reduce the induced drag. During cruise flight, solely these propellers provide thrust – all other propellers are retracted via a folding mechanism.

In [23] a series hybrid-electric version of a Cessna 172 is investigated. Two versions are preliminary designed: a first version represents a plain replacement of the combustion engine with an electric motor. A modified version is equipped with electric motors at the wing tips to reduce induced drag. Further, propellers driven by electric motors are distributed along the wing span to increase the maximum lift coefficient and a single electric motor is additionally installed in the aft of the fuselage, which is powering a pusher propeller. Three different battery technology levels are investigated for the mass specific energy of the battery cells ranging from 250 Wh/kg to 1000 Wh/kg. The efficiency of the combustion engine is set constant to 350 g/kWh, which equals to 24 %.

In [24] a hybrid-electric aircraft with a seating capacity of 19 is designed preliminary. The aircraft is designed to carry out transport missions with flight ranges below 200 km with energy stored in a battery system only. For flights with longer ranges up to 3,000 km, a range extender system based on two gas turbines is used to generate the necessary power. The mass specific energy is assumed to be 230 Wh/kg. It has been presumed in the investigation, that the increased battery mass of 2,018 kg has little effect onto the mass of the structural components of the aircraft. The authors predict that the fuel consumption is lower on all flight range below 1,200 km with respect to the reference aircraft Dornier Do 228.

The aircraft concept PEGASUS [25] identified a synergistic combination of the mentioned features for the class of a regional aircraft with 48 passengers. PEGASUS stands for "Parallel Electric-Gas Architecture with Synergistic Utilization". The aircraft concept is propelled by five electric motors and two gas turbines. Each gas turbine is coupled directly with an electric motor and installed at the wing tips of the aircraft. The driven propellers at the wing tips possess an increased propulsive efficiency of 18 %. Two more electric motors are installed on the inboard section of the wing, providing power during take-off and climb. However, during cruise these electric motors are stopped and the propellers are folded. As a result, the lift distribution at the corresponding wing position is not distorted by the swirl of the turning propeller and the lift distribution can be maintained in its ideal form in cruise flight. A fifth electric motor is installed at the rear of the fuselage capturing the boundary layer of the fuselage increasing the effective propulsive efficiency by a magnitude of 10 %. A significantly increased maximum take-off mass of 31 % and 65 % compared to the conventional propulsion baseline aircraft was found. The authors assume a specific energy of the battery of 500 Wh/kg.

In [26] the hybridization of a regional aircraft for 48 passengers is investigated. Three battery options are investigated as technology scenarios with a specific energy between 650 Wh/kg and 1000 Wh/kg and a specific power of 0.4 kW/kg and 1 kW/kg. With these technology levels a tank-to-wheel reduction of 8 % to 22 % for a 350 NM transport mission is reached.

2.3 Advantages of the electric aircraft e-Genius

In the following section it shall be shown which advantage an airframe can offer, which is optimized for an integration of a single electric motor compared to an airframe which is designed for a single combustion engine. The consideration is based on the integration of the electric motor in the vertical tail with the aim to reduce the required shaft power

Figure 2.2: Preliminary aircraft concept "Parallel Electric-Gas Architecture with Synergistic Utilization" PEGASUS investigated by NASA, image source: [25]

for flight. Fig. 2.3 shows the aircraft "Valentin Taifun" propelled with a single, internal combustion engine and the aircraft "e-Genius", where the electric motor is installed in the vertical stabilzer. The combustion engine of the Valentin Taifun is placed in front of the pilot close to the centre of gravity, due to its high relative weight. Thus the air flow is blown from the propeller over the fuselage, which results in higher friction and pressure drag. In addition, the propeller diameter is limited by the length of the landing gear. A smaller propeller diameter leads to an increased propeller disc loading which lowers the propeller efficiency in this aircraft class [4]. A larger propeller can only be realized through a larger and therefore heavier landing gear. An electric motor with the same power is lighter, more compact and can be integrated aerodynamically efficient in the vertical tail. In this case, the propeller is not limited by the length of the landing gear and can be designed with a larger diameter which leads to a higher propeller efficiency η_P. Further, the landing gear can be reduced in its size and can be equipped more easily with a retraction mechanism, which leads to lower parasitic drag. Furthermore, the forward part of the fuselage can possess a more aerodynamic shape which results in a better glide ratio $\frac{L}{D}$. Additionally the integration efficiency η_I is increased as the airflow of the propeller is only blown over the nacelle of the small electric motor and the vertical stabilizer.

Installing the electric motor in the vertical stabilizer results in the described advantages but possesses some disadvantages too. Firstly, the thrust generated by the propeller is not pointing through the center of gravity. As a consequence, a change in the generated propeller thrust leads to a change in the longitudinal moment of the aircraft. This was investigated in the flight test campaign of the electric aircraft e-Genius

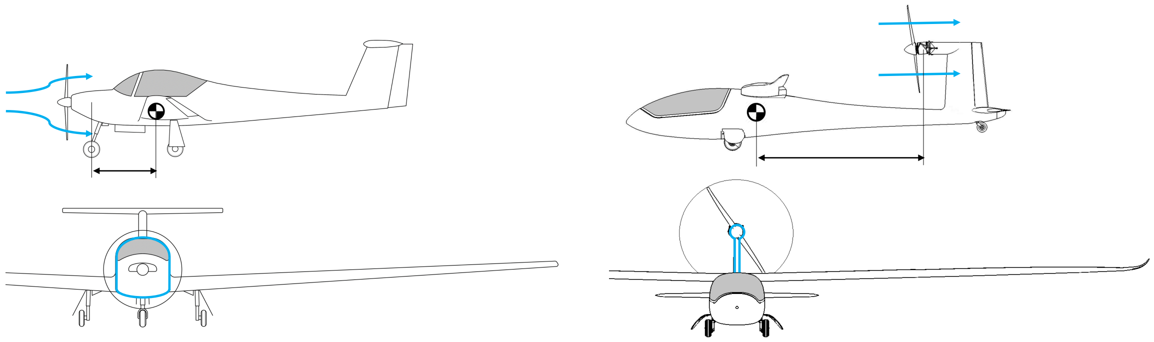

Figure 2.3: Comparison of the conventional airplane "Valentin Taifun 17E II" equipped with a combustion engine to the airplane "e-Genius" which is propelled by an electric motor

Parameter	**Value**
Empty mass	450 kg
Battery mass	280 kg
Payload (pilot + passenger)	180 kg
Max. take-off mass	910 kg
Max. shaft power of electric motor	75 kW
Wing area	14.56 m^2
Wing span	16.9 m
Cruise speed (TAS in 8000 ft.)	180 km/h
Required shaft power for cruise	18.9 kW
Product of propeller and integration efficiency $\eta_P \cdot \eta_I$	0.82
Product $\frac{L}{D} \cdot \eta_P \cdot \eta_I$ (@ cruise speed 180 km/h)	23.6

Table 2.2: Data of the battery powered e-Genius

of the University of Stuttgart. It was shown that the pilot is able to counter the moment change by the elevator. Another result of the elevated thrust axis is that the trim drag rises slightly as the horizontal stabilizer has to generate more downforce in order to counter the additional longitudinal moment. However this drag rise is overcompensated by the described increase of glide ratio $\frac{L}{D}$, propeller efficiency η_P and propeller integration efficiency η_I of the aircraft configuration. As a result the e-Genius requires a significant lower shaft power for cruise flight as listed in table 2.2 than comparable, conventionally powered aircraft do. In section 4.1.4 the product $\frac{L}{D} \cdot \eta_P \cdot \eta_I$ of different conventional, single engine aircraft is determined and compared to the parameter of the electric aircraft.

2.4 Advantages of the series hybrid-electric aircraft e-Genius

With the Breguet range equation the possible advantages and disadvantages of conventional and electric aircraft can be depicted. The equation relates the energy stored on board an aircraft to the range which it can fly in horizontal flight with this energy. The formula contains the product $\frac{L}{D} \cdot \eta_P \cdot \eta_I$, which describes the overall aerodynamic efficiency in powered cruise flight. Formula 2.1 shows the Breguet equation[3] for conventional aircraft driven by a combustion engine and formula 2.2 shows the corresponding range equation for battery powered aircraft [27]. Further, the equations contain the specific energy $E_{s,Fuel}$ and $E_{s,Bat}$ of the energy storage system.

$$R_{Fuel} = \frac{L}{D} \cdot \eta_P \cdot \eta_I \cdot \eta_{ICE} \cdot \frac{E_{s,Fuel}}{g} \cdot \ln \frac{1}{1 - \frac{m_{Fuel}}{m_{MTO}}} \tag{2.1}$$

$$R_{Battery} = \frac{L}{D} \cdot \eta_P \cdot \eta_I \cdot \eta_{EM} \cdot \frac{E_{s,Bat}}{g} \cdot \frac{m_{Bat}}{m_{MTO}} \tag{2.2}$$

In table 2.3 the parameter $\frac{L}{D} \cdot \eta_P \cdot \eta_I$ and the specific energy E_s of the conventional propelled Valentin Taifun are compared to the battery powered e-Genius. Although the product $\frac{L}{D} \cdot \eta_P \cdot \eta_I$ of the electric e-Genius is significantly increased, it cannot compensate the lower specific energy of battery cells $E_{s,Bat}$, which is 45 times lower than the specific energy of liquid fuels $E_{s,Fuel}$.

Term	**Valentin Taifun**	**e-Genius**
$\frac{L}{D} \cdot \eta_P \cdot \eta_I$	12.0	23.6
E_s (specific energy)	$E_{s,Fuel} = 11,300\,{}^{Wh}/_{kg}$	$E_{s,Bat} = 230\,{}^{Wh}/_{kg}$

Table 2.3: Specific energy E_s and the parameter $\frac{L}{D} \cdot \eta_P \cdot \eta_I$ of a conventional single-engine aircraft compared to an optimized electrically powered aircraft

In case of the electrically propelled e-Genius, a series hybrid-electric aircraft can combine the advantages of both systems. In this sense the increased aerodynamic parameter $\frac{L}{D} \cdot \eta_P \cdot \eta_I$ of the optimized electric airframe can be combined with the superior energy density of liquid fuels. Thereby the motor which drives the propeller is an electric motor and the energy storage consists of a battery system and a generator system, which transforms liquid fuel into electric power. In contrast to a parallel hybrid-electric system, the internal combustion engine is not mechanically connected

---

[3] Breguet equation for constant lift coefficient and constant true airspeed

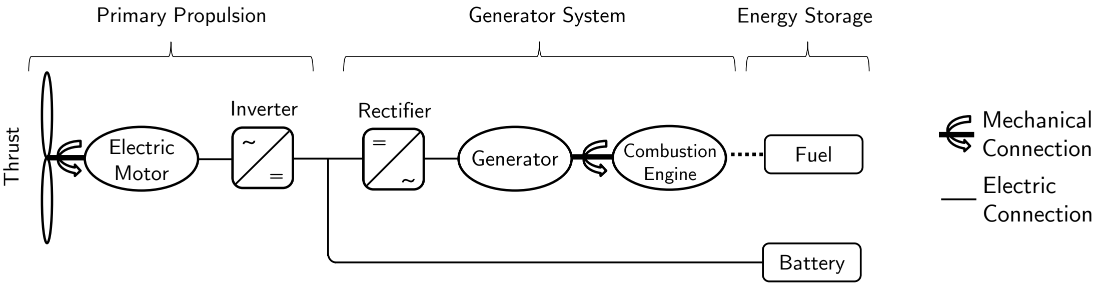

Figure 2.4: Schematic system layout of a series hybrid-electric propulsion system

to the propeller or fan shaft, as shown in schematic system layout in Fig. 2.4. An exemplary realization of a series hybrid-electric aircraft with an optimized airframe is shown in Fig. 2.5, where the combustion engine is installed near to the center of gravity inside the fuselage, but the propeller is driven by an electric motor which is placed in the vertical stabilizer of the aircraft.

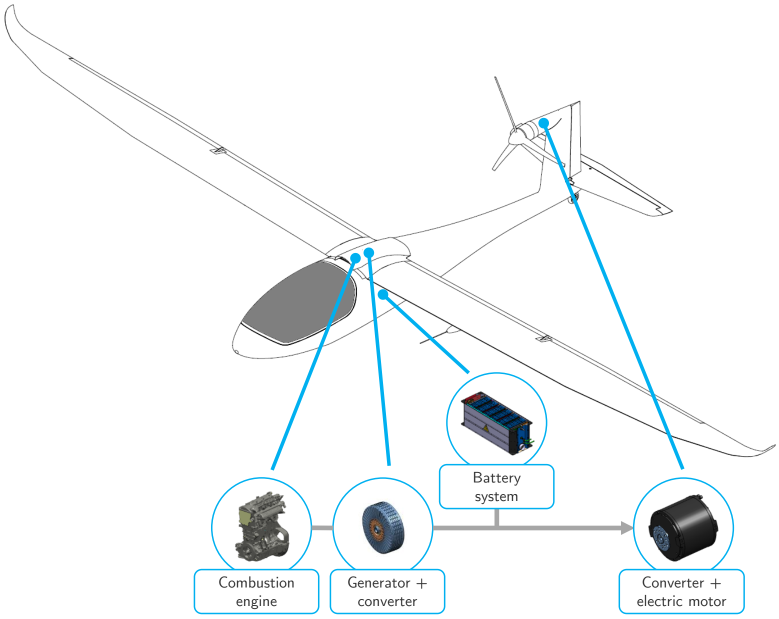

Figure 2.5: Application of a series hybrid-electric propulsion system in the aircraft e-Genius

2.5 Scope of the thesis

The scope of this thesis is to identify an optimized sizing for the propulsion system of series hybrid-electric aircraft, where the electric motor is installed in the vertical tail. Two transport missions are derived from two typical use-cases in the general aviation: a four-seat aircraft flying with a cruise speed of 120 knots ($\sim$ 220 km/h) and a nine-seat aircraft traveling with a cruise speed of 220 knots ($\sim$ 400 km/h). In order to derive optimized configurations of the hybrid-electric propulsion system, the characteristics of the individual components shall be evaluated by data of existing components analyzed statistically in a transparent manner. A special focus shall be set onto the parameters, which are most relevant for the preliminary aircraft design: scaling of mass and efficiency as well as part load characteristics and influence of altitude on power and efficiency. For the sake of simplicity, the interaction between mass specific energy and mass specific power of battery cells is often neglected in preliminary aircraft design. In order to incorporate this effect into the sizing calculation, a battery model is derived from data of existing modern battery cells. All auxiliary systems, which are required for the operation of the hybrid-electric propulsion system e.g. cooling systems, cables, housings,etc. shall be included as well into the preliminary aircraft design loop in order to improve the quality of the results. The characteristics of the components shall be investigated in the relevant power range from $\sim$50 kW to $\sim$2,000 kW. Furthermore, the interaction between additional mass of the propulsion components and consequential mass growth on aircraft level shall be evaluated. Further, the impact of an increased aircraft mass on the aerodynamic parameters shall be investigated. The influence of possible component failures onto the required power and energy reserves, which have to be designed as allowances into the hybrid-electric propulsion system shall be explored. These allowances shall enable an Equivalent of Safety in a possible certification process at a later stage. The gained knowledge shall be incorporated into an aircraft sizing scheme, where an optimized sizing of the propulsion system for each investigated transport mission can be derived. Optimized parameters shall be provided for: type, number and power rating of combustion engine as well as the required type and size of the battery system. Due to the interactions between propulsion system and aerodynamic parameters and structural component mass, the corresponding parameters are iterated in the design process continuously. The resulting hybrid-electric aircraft shall be compared to corresponding modern, conventionally propelled aircraft. In order to make a sound comparison, the hybrid-electric aircraft shall achieve similar handling characteristics and flight performance as the corresponding conventional aircraft. Lastly, a sensitivity study shall be carried out in order to identify the influence of technology improvements onto the fuel consumption of the hybrid-electric aircraft.

Chapter 3

Characteristics of the propulsion components

3.1 Statistical evaluation of trends

In order to evaluate the scaling laws of propulsion components, the data of existing components is used to derive trend curves. A multiple linear regression is applied to identify trend curves. An advantage of the linear regression is that the coefficient of determination R^2 can be used to assess the quality of the fit. It describes which proportion of the total variance can be explained by the regression model e.g. $R^2 = 0.9$ indicates that 90% of the variance in the examined data can be explained by the regression model [28]. According to [29] the values for R^2 in table 3.1 can be used to evaluate the magnitude of correlation in mass estimation of aerospace structures. A high coefficient of determination R^2 indicates a suitable trend curve – however, an increased R^2 can be also the result of a trend curve which contains a high number of regression coefficients [28]. As a result the regression starts to model the random errors of the data rather than the actual trend. In order to prevent this effect called overfitting, the "leave-one-out"-cross validation is applied. In this validation, one data point of the data set is left out and consequently the error between the resulting trend curve and the data point left out is calculated [30]. This is repeated for all points of the data set and the sum of errors is calculated. With this sum of errors, the predicted coefficient of determination R^2_{Pred} can be calculated [31]. Trend curves which suffer from overfitting will result in a low predicted coefficient of determination R^2_{Pred}. The value of R^2_{Pred} can be interpreted similarly to the value of R^2.

Coefficient of determination R^2	**Magnitude of correlation**
0 - 0.2	not given
0.2 - 0.5	weak
0.5 - 0.75	medium strong
0.75 - 0.95	strong
0.95 - 1	direct linear or inversely related

Table 3.1: Coefficient of determination for aerospace structures according to [29]

The process to calculate and ensure a statistical significant trend curve is described subsequently, taking the relationship between the power setting P of a gas turbine and the corresponding efficiency η_{GT} at that power setting as an example. The power setting P is expressed as a fraction $^{P}/_{P_{max}}$, where P_{max} denotes the maximum rated power. Accordingly the efficiency η_{GT} is expressed as a fraction of the maximum achievable efficiency $^{\eta_{GT}}/_{\eta_{GT,max}}$. In order to ensure a trend curve which is reflecting the trend correctly, the following selection criteria were applied:

- Only turboshaft engines were investigated, which are applied in aviation
- Measurements were obtained under sea level conditions

Furthermore, the following assumptions were made to ensure valid trend curve.

- The influence of inlet losses is regarded as marginal
- The same percentage of shaft power is extracted for the operation of an accessory drive and a bleed air system

The data of three gas turbines meeting the selection criteria was found: the Allison Model 250 C30 [32], the PW127F [33] and the PT6A-2 [34]. The data is plotted in Fig. 3.1 and the trend curve in equation 3.1 is postulated to be suitable. The statistical significance will be proven at a later stage by the means of statistic measures.

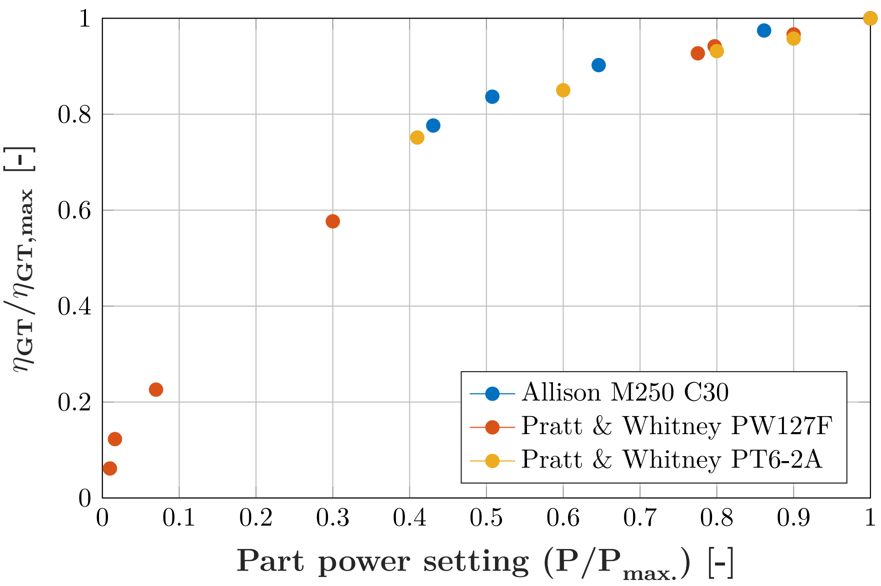

Figure 3.1: Data of three turboshaft engines: impact of part power setting on efficiency of gas turbines

$$^{\eta_{GT}}/_{\eta_{GT,max}} = \beta_0 + \beta_1 \cdot \left(^{P}/_{P_{max}}\right) + \beta_2 \cdot \left(^{P}/_{P_{max}}\right)^2 + \beta_3 \cdot \left(^{P}/_{P_{max}}{}^3\right) \tag{3.1}$$

The non-linear equation 3.1 can be transformed into a multiple linear regression model through replacing each function of the independent variable $(^{P}/_{P_{max}})$ by an individual independent variable x_i as shown in equation 3.2 [35].

$$\boldsymbol{x^t} = \begin{pmatrix} x_1 & x_2 & x_3 \end{pmatrix} = \begin{pmatrix} ^{P}/_{P_{max}} & \left(^{P}/_{P_{max}}\right)^2 & \left(^{P}/_{P_{max}}\right)^3 \end{pmatrix} \tag{3.2}$$

With the sample data of the existing gas turbines the design matrix $\boldsymbol{X}$ and the vector $\boldsymbol{y}$ is constructed. The part power settings are the predictor values and are placed into the design matrix $\boldsymbol{X}$ – each row of the matrix contains one data point of the sample. The corresponding part load efficiencies of the gas turbines are placed into the rows of the response vector $\boldsymbol{y}$ in such way that equation 3.3 can be written.

$$\boldsymbol{y} = \boldsymbol{X} \cdot \boldsymbol{\beta} \tag{3.3}$$

$$\text{with} \qquad \boldsymbol{X} = \begin{pmatrix} 1 & x_{1,1} & x_{2,1} & x_{3,1} \\ 1 & x_{1,2} & x_{2,2} & x_{3,2} \\ \vdots & \vdots & \vdots & \vdots \\ 1 & x_{1,n} & x_{2,n} & x_{3,n} \end{pmatrix} \qquad \text{and} \qquad \boldsymbol{y} = \begin{pmatrix} y_1 \\ y_2 \\ \vdots \\ y_n \end{pmatrix} = \begin{pmatrix} \left(^{\eta}/_{\eta_{max}}\right)_1 \\ \left(^{\eta}/_{\eta_{max}}\right)_2 \\ \vdots \\ \left(^{\eta}/_{\eta_{max}}\right)_n \end{pmatrix} \tag{3.4}$$

With the design matrix $\boldsymbol{X}$ and the vector $\boldsymbol{y}$, the vector of the estimated regression coefficients $\boldsymbol{\beta}$ can be calculated using equation 3.5.

$$\boldsymbol{\beta} = (\boldsymbol{X}^t\boldsymbol{X})^{-1}\boldsymbol{X}^t\boldsymbol{y} \qquad \text{with} \qquad \boldsymbol{\beta} = \begin{pmatrix} \beta_0 \\ \beta_1 \\ \vdots \\ \beta_n \end{pmatrix} \tag{3.5}$$

In this example, the trend curve in equation 3.1 was found to be suitable with an predicted coefficient of determination of $R^2_{Pred} = 0.994$. The trend curve is plotted in Fig. 3.2 along with the 95 % confidence interval for a new observation, which describes the uncertainty that a new observation is predicted correctly.

The trend curve is reviewed subsequently for plausibility. When operating the gas turbine at its highest power setting, the highest overall pressure ratio OPR and the highest turbine inlet temperatures T_{t4} are reached, which leads to the maximum efficiency of the gas turbine cycle as described in section 3.2. As the power setting is reduced, OPR and T_{t4} decrease which lowers the efficiency of the gas turbine cycle.

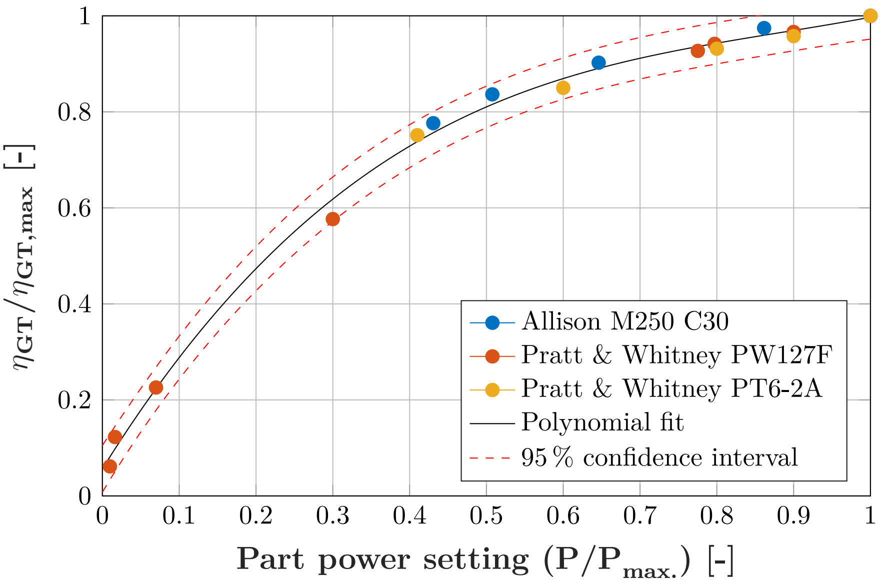

Figure 3.2: Trend curve and prediction bounds of impact of part power setting onto efficiency of gas turbines

Further, the efficiencies of compressor and turbine vary for different power settings. In [36] and [37] it can be observed, that compressor and turbine pass an individual peak of efficiency as the power setting is decreased. At low part power settings the low efficiency of the thermodynamic cycle as well as the lowered component efficiencies lead to a significantly reduced gas turbine efficiency.

The 95 % confidence interval ci is calculated with equation 3.6 [30]. The vector $\boldsymbol{x}$ contains the predictor values where the upper and lower predictions bounds are calculated. σ is the standard deviation and t_s is the value of Student's inverse cumulative distribution function calculated with $n - k_\beta$ degrees of freedom and for a confidence level of $(1-{}^{\alpha}/_{2})$. In the investigated trend curve for the efficiency at part power setting, the sample size is $n = 18$ and the number of regression coefficients β is $k_\beta = 4$. Further, the common significance level of $\alpha = 0.05$ is applied. The calculated observation prediction bounds are shown as red lines in Fig. 3.2.

$$ci = \boldsymbol{x'} \cdot \boldsymbol{\beta} \pm t_{s,n-k_\beta,1-\alpha/2} \cdot \sigma \cdot (1 + \boldsymbol{x'(X'X)^{-1}x}) \tag{3.6}$$

$$\sigma = \frac{1}{n-1} \sum_{i=1}^{n} (y(x_i) - y_i)^2 \tag{3.7}$$

In the following, the significance of each regression coefficient β_i is investigated – as a result the model can potentially be reduced in size, as the impact of some coefficients

Coefficient β_i	**Value**	**Unit**	**Standard deviation** se_i	**t-test**	**p-value**
β_0	0.05658	[-]	0.0140	4.04	0.0006
β_1	2.567	[-]	0.1417	18.12	0.0000
β_2	-2.612	[-]	0.3410	7.66	0.0000
β_3	0.9858	[-]	0.2181	4.52	0.0002

Table 3.2: Statistic on regression coefficients

is not significant. The estimated standard deviations se_i of the regression coefficients are the diagonal elements of the matrix $\boldsymbol{se}$ in equation 3.8. In table 3.2 the estimated standard deviations of the regression coefficients β_i for the trend curve of the part power efficiency are listed.

$$\boldsymbol{se} = \sqrt{\sigma^2 \cdot \left(\boldsymbol{X'X}\right)^{-1}} \tag{3.8}$$

With a t-test the significance of each regression coefficient β_i is proven [30][28]. In the applied t-test the regression coefficient β_i is divided by its standard deviation se_i as shown in equation 3.9. With the resulting value of the t-test a p-value can be calculated which is used to quantify the significance of the coefficient by comparing it to the common significance level of $\alpha = 0.05$. In table 3.2 the t-tests and the corresponding p-values of the coefficients are given. As all p-values are lower than the chosen significance level, all coefficients can be considered statistically significant.

$$t\text{-}test = \frac{\beta_i}{se_i} \tag{3.9}$$

As a last step, the random characteristics of the predictions errors produced by the trend curve are investigated. The residual plot in Fig. 3.3 shows the difference between the observed values and the estimated values by the regression curve over the fitted range of the independent variable. It is used to investigate if the magnitude of the errors are randomly distributed. By verifying this, biased fitted curves are prevented, which would not reproduce the trend appropriately [38]. Furthermore, in the histogram shown in Fig. 3.4 the distribution of the magnitude of the errors can be reviewed – a normal distribution of the residuals is a prerequisite of a valid trend curve. A χ^2-test is used to test the distribution for a normal distribution at a confidence level of 0.95. In the investigated example a normal distribution is proven by the χ^2-test and it can be assumed that the determined trend curve represents the trend correctly.

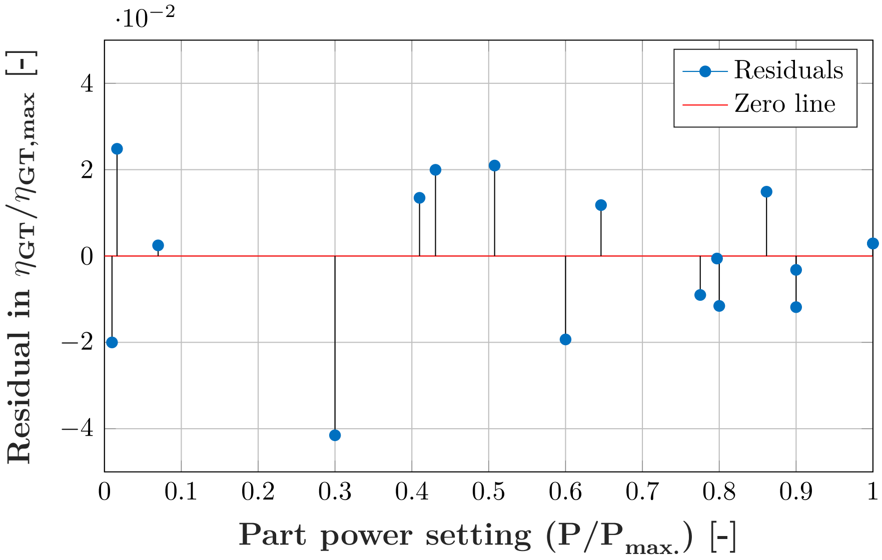

Figure 3.3: Residuals over the fitted range of the independent variable $^{P}/_{P_{max}}$

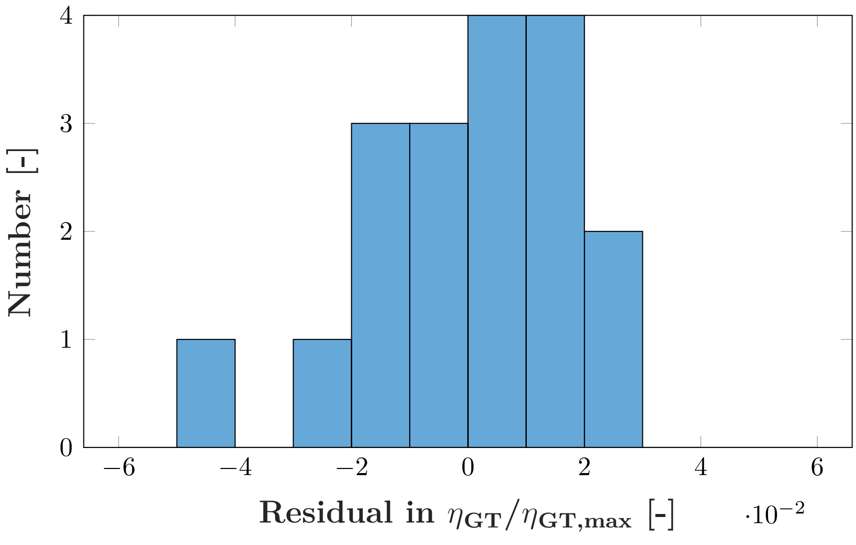

Figure 3.4: Distribution of the magnitude of errors in the predicted variable $^{\eta_{GT}}/_{\eta_{GT,max}}$

The determined trend represents the data of the investigated technology and does not possess universal validity. Gas turbines which are equipped with innovative technologies might not be covered by the determined trend curve. Special caution and consideration has to be applied if a trend curve is used to extrapolate characteristics beyond the data set from which the trend curve was derived.

The described procedure to identify statistically significant regression curves is applied to trend curves used in this dissertation. In the following sections the primary components of the serial hybrid-electric propulsion system are statistically assessed by the described methods.

3.2 Gas turbines

3.2.1 Efficiency scaling effects

Gas turbines in aviation can be classified into turbojet, turbofan, turboprop and turboshaft engines. Turboshaft and turboprop engines are suitable for the application in a series hybrid-electric propulsion system as they produce mechanical shaft power, which can be converted by a generator into electric power.

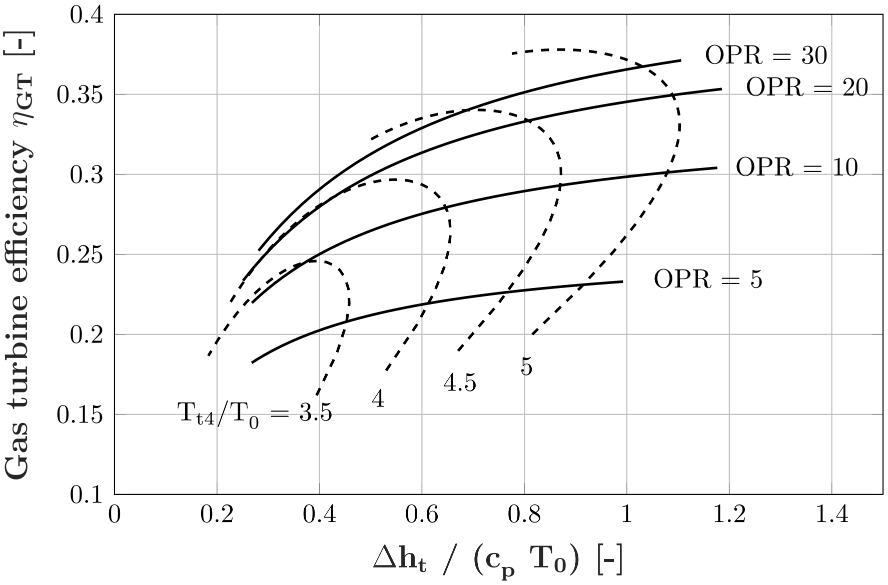

Figure 3.5: Influence of specific work output $\Delta h_t / c_p \cdot T_0$, overall pressure ratio (OPR) and ratio between turbine entry total temperature and ambient temperature T_{t4}/T_0 on efficiency of the gas turbine η_{GT}

According to [37] the efficiency of a gas turbine cycle is influenced by the overall pressure ratio (OPR) and the turbine entry temperature T_{t4}. The OPR describes the pressure increase achieved by the compressors of the engine, whereas T_{t4} marks the temperature of the gas entering the turbine after being burnt in the combustion chamber. In Fig. 3.5 the calculated gas turbine efficiency η_{GT} is plotted versus the

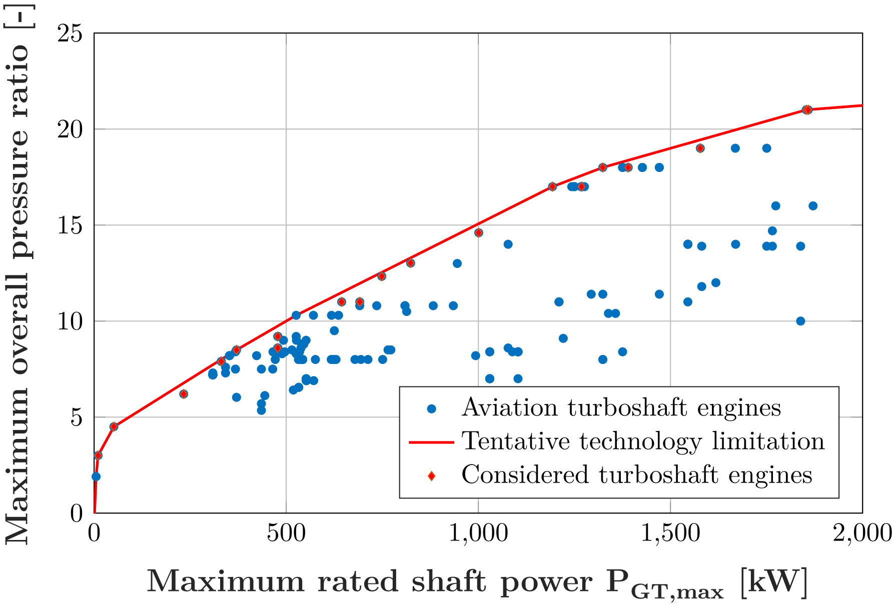

Figure 3.6: Maximum overall pressure ratio (OPR) achieved by turboshaft engines developed between 1955 and 2009 plotted versus the maximum rated power with data from [39]

specific work output ${}^{\Delta h_t}/{}_{c_p \cdot T_0}$ [1]. The influence of the OPR and the ratio between turbine entry total temperature and ambient temperature ${}^{T_{t4}}/{}_{T_0}$ is shown. It can be observed that for a specific ratio of ${}^{T_{t4}}/{}_{T_0}$, different OPRs are required in order to maximize either gas turbine efficiency or the parameter ${}^{\Delta h_t}/{}_{c_p \cdot T_0}$. Furthermore, it can be seen that OPR and ${}^{T_{t4}}/{}_{T_0}$ have to be increased simultaneously to achieve an increased gas turbine efficiency.

In order to investigate aviation gas turbines, the data of 204 turboshaft and turboprop engines, which were developed between 1955 and 2009, was obtained from [39] and [40]. In Fig. 3.6 the maximum OPR achieved by the engines is plotted versus the corresponding maximum output power at sea level. It can be observed that the highest realized OPR for a certain rated power increases with rising rated power of the engines. A reasoning for this tentative technology limitation is discussed later herein.

In order to obtain trend curves of gas turbines, which are relevant for the application in hybrid-electric aircraft, the data set was reduced. Firstly, only gas turbines were considered which are located close to the tentative technology limitation of the OPR in Fig. 3.6 and consequently achieve a high efficiency of the gas turbine cycle. Addition-

---

[1] Assumptions according to [37]: isentropic efficiency of compressor $\eta_c = 0.86$; isentropic efficiency of each turbine $\eta_t = 0.89$; mechanical efficiency of each shaft $\eta_m = 0.99$; combustion efficiency $\eta_m = 0.99$; combustion chamber pressure loss: 6 %; turbine entry total temperature: $T_{t4} = 1300$ K

ally, data points reflecting engines with a mainshaft gear box were eliminated, because the mass of the additional gear box increases the engine mass significantly. This can be shown exemplary by considering the mass of the engines CT7-5A2 and CT7-2D1 produced by General Electric. Both engines consist of the same base engine with a similar power rating and the same OPR. However, the mass of the engine CT7-5A2 is increased by 68 % as it contains a gear box, which reduces the speed of the output shaft from 20,000 RPM to 1,384 RPM. As this reduction gear box is not required for driving electric generators, only data points reflecting solely the engine are considered for the application in a hybrid-electric propulsion system. In addition, engines with an output shaft positioned at the same location as the exhaust pipe were not considered, as current electric generators are not able to withstand the increased exhaust temperatures from gas turbines.

For the remaining gas turbines, the numerical data can be found in table B.1 in the appendix. The maximum gas turbine efficiency $\eta_{GT,max}$ is plotted versus the maximum rated shaft power $P_{GT,max}$ in Fig. 3.7. It can be observed, how the gas turbine efficiency increases with rated power. A trend curve, which is shown in equation 3.10, was derived from the data. Although a logarithmic term is present in the equation, the methods of linear regression can be applied, as the regression coefficient β_1 is a linear factor [35]. In table 3.3 the regression coefficients with the respective p-values are listed. Moreover, table 3.3 contains the applicable units of the obtained empiric equation.

The obtained relation is checked subsequently for plausibility. The compressor and the turbine of a gas turbine require a small annular tip clearance between rotor blade tip and the outer casing. Under the assumption that the tip clearance of these components is a parameter resulting from mechanical tolerances and stays in the same order of magnitude for small and large blades, a small blade height is more affected by a pressure loss due to the tip clearance than a larger blade. Hence, a small gas turbine with a small blade height and a low rated power is more affected by tip clearance losses. Furthermore, the efficiency of the gas turbine cycle is influenced by the OPR and ${}^{T_{t4}}/{}_{T_0}$ as described in Fig. 3.5. However, increasing the OPR for a gas turbine with low rated power would decrease the blade height below a feasible size with the tip clearance staying constant. Hence, gas turbines with lower rated power tend to feature a lower OPR as shown in Fig. 3.6, which results in a lower η_{GT}. Another contributing factor is that gas turbines with a lower internal diameter are associated with lower Reynolds numbers of the internal flow. The lower Reynolds number leads to relatively larger boundary layers and results in more associated losses in the flow.

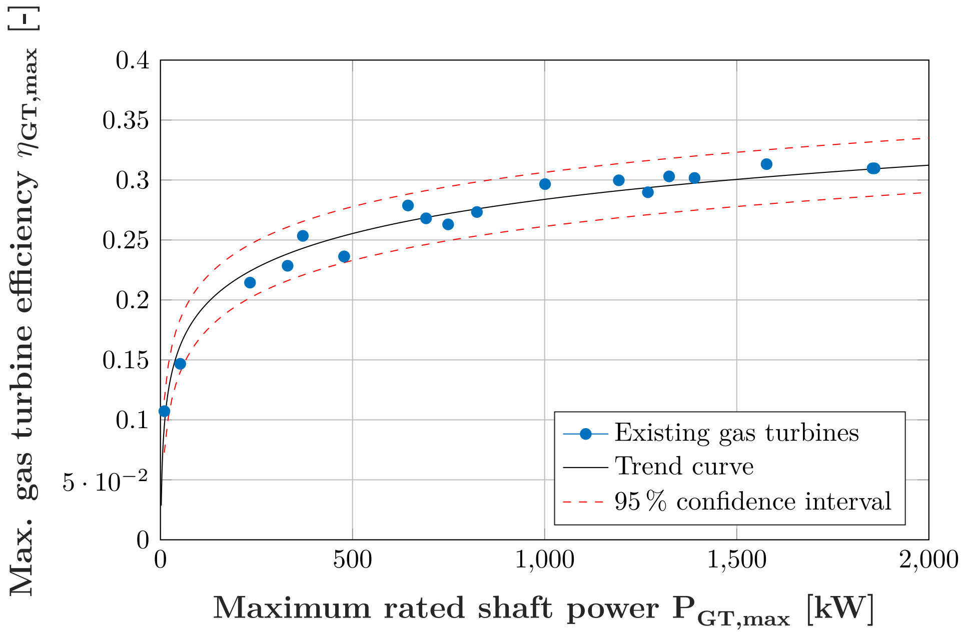

Figure 3.7: Maximum gas turbine efficiency plotted versus maximum rated shaft power (both at sea level) of the considered turboshaft engines

$$\eta_{GT,max} = \beta_1 \cdot \ln\left[\frac{P_{GT,max}}{(1\,kW)}\right] \tag{3.10}$$

Symbol	Unit
$\eta_{GT,max}$	$[-]$
$P_{GT,max}$	$[kW]$

Coefficient	Value	Unit	p-value
β_1	0.04117	[-]	0.000

Table 3.3: Units and regression coefficient for the trend curve of the maximum efficiency of the investigated gas turbines $\eta_{ICE,max}$ with $R^2_{pred} = 0.9618$

According to [41] and [42] an increased flight altitude has a beneficial impact on the efficiency of a turboprop engine. The data provided by [41] is shown in Fig. 3.8 and a trend curve, given in equation 3.11, for the relative improvement of the gas turbine efficiency $\eta_{GT,max}/\eta_{GT,max,H=0}$ is derived to model this characteristic. To justify the trend, different effects have to be considered as the efficiency of the gas turbine is influenced by several effects. Firstly, the air density and the ambient air temperature T_0 decrease with increasing altitude – standardized values are given in [43]. Under the assumption that a constant shaft speed is applied for all flight altitudes, the non-dimensional shaft speed $N/\sqrt{T_0}$ of the gas turbine increases because the ambient air temperature T_0

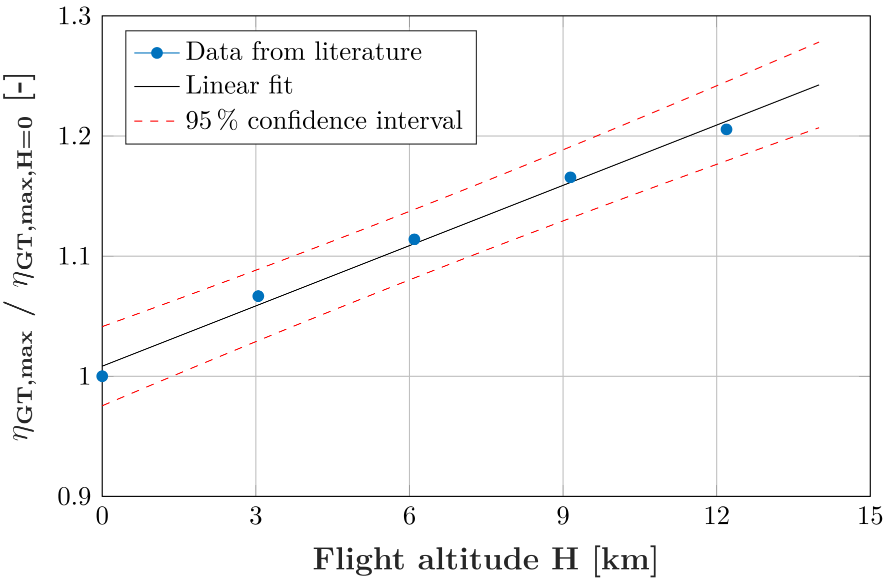

Figure 3.8: Impact of flight altitude on maximum gas turbine efficiency with data from [41]

decreases. As a result, the efficiency of the compressor is lowered [36] [37]. Furthermore, the kinematic viscosity of the ambient air increases as flight altitude is increased [44] – as a result, the Reynolds number decreases and the associated losses due to the relatively larger boundary layer increase. However, the raised non-dimensional shaft speed $^{N}/_{\sqrt{T_0}}$ enables a higher overall pressure ratio delivered by the compressor [36] [37]. As shown in Fig. 3.5, an increased overall pressure ratio in combination with an increased temperature ratio $^{T_{t4}}/_{T_0}$ leads to a higher efficiency of the gas turbine. With the presented data it is concluded that the effects which increase the gas turbine efficiency outweigh the effects which deteriorate the efficiency of the gas turbine when flight altitude is increased.

$$^{\eta_{GT,max}}/_{\eta_{GT,max,H=0}} = \beta_1 + \beta_2 \cdot H \tag{3.11}$$

Symbol	Unit
$^{\eta_{GT,max}}/_{\eta_{GT,max,H=0}}$	$[-]$
H	$[km]$

Coefficient	Value	Unit	p-value
β_1	1.005	$[-]$	0.0006
β_2	0.01785	$[^{1}/_{km}]$	$1 \cdot 10^{-6}$

Table 3.4: Units and regression coefficients for the trend curve of the relative improvement of the gas turbine efficiency due to increased flight altitude with $R^2_{pred} = 0.9659$

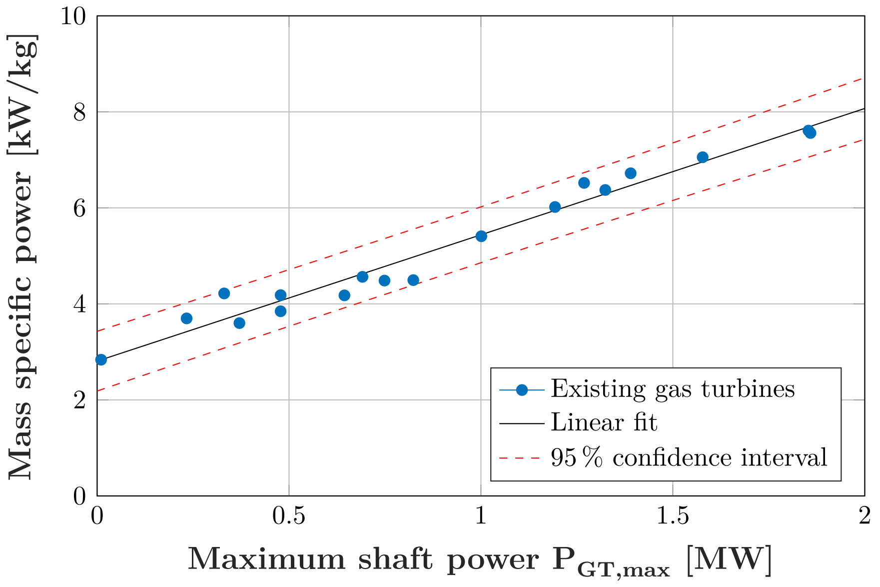

Figure 3.9: Mass specific power plotted versus take-off power of investigated gas turbines

3.2.2 Power scaling effects

In Fig. 3.9 the mass specific power $\left({}^{P_{GT,max}}\!/_{m_{GT}}\right)$ of the gas turbines is plotted as a function of the maximum power $P_{GT,max}$ of the engines selected in section 3.2.1. The mass specific power is calculated by dividing the power of the gas turbine by its corresponding mass. A linear trend with a positive gradient can be observed, which means that the considered gas turbines get relatively lighter the higher the corresponding rated power is. A linear trend curve, which is shown in equation 3.12, can be obtained.

$$\left({}^{P_{GT,max}}\!/_{m_{GT}}\right) = \beta_0 + \beta_1 \cdot P_{GT,max} \tag{3.12}$$

Symbol	Unit
$\left({}^{P_{GT,max}}\!/_{m_{GT}}\right)$	$\left[{}^{kW}\!/_{kg}\right]$
$P_{GT,max}$	$[MW]$

Coefficient	Value	Unit	p-value
β_0	2.834	$\left[{}^{kW}\!/_{kg}\right]$	$0.24 \cdot 10^{-12}$
β_1	2.622	$\left[{}^{kW}\!/_{kg \cdot MW}\right]$	$0.20 \cdot 10^{-12}$

Table 3.5: Units and regression coefficients for the trend curve of the mass specific power $\left({}^{P_{GT,max}}\!/_{m_{GT}}\right)$ of the investigated gas turbines with $R^2_{pred} = 0.9630$

As the flight altitude increases the maximum power of a gas turbine decreases, which is commonly referred to as "power lapse". In Fig. 3.10 it can be observed, how the maximum power output of a gas turbine, which is not flat-rated, decrease as flight altitude increases. The empiric equation 3.13 given by [41] is used to describe the

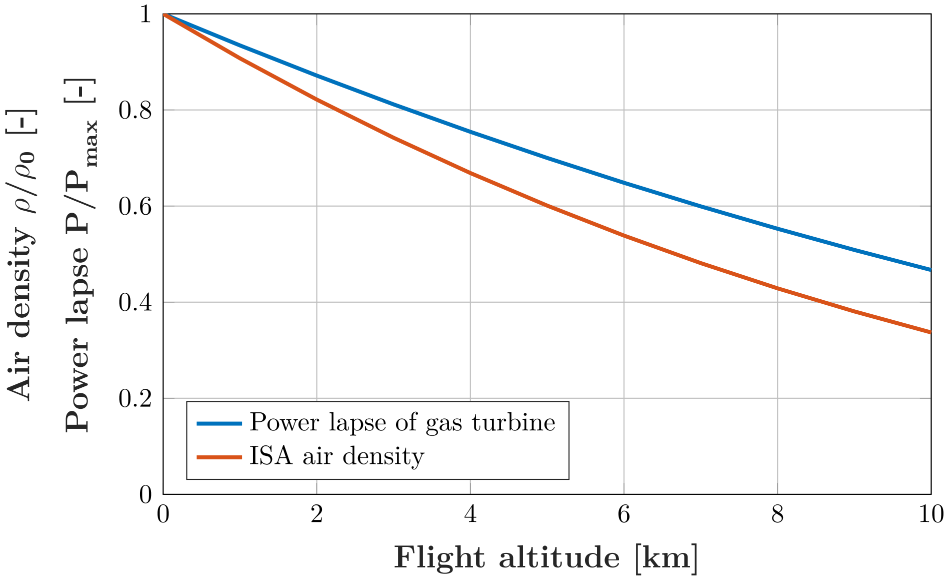

Figure 3.10: Power lapse of gas turbine [41] and ISA air density [43] plotted versus flight altitude

power lapse for gas turbines. The equation was obtained with data of a "typical turboprop engine". Additionally, the change of air density of the atmosphere as standardized by [43] is plotted as a reference.

$$\frac{P_{GT,max,H}}{P_{GT,max,H=0}} = \left(\frac{\rho_H}{\rho_{H=0}}\right)^{0.7} \tag{3.13}$$

To justify the trend, different effects have to be taken into account. As described in section 3.2.1, an increased flight altitude leads to an increased efficiency of the gas turbine. Under the assumption of a constant propeller speed, the raised non-dimensional shaft speed ${}^{N}/_{\sqrt{T_0}}$ enables a higher overall pressure ratio delivered by the compressor [36] [37]. As shown in Fig. 3.5, an increased overall pressure ratio in combination with an increased temperature ratio ${}^{T_{t4}}/_{T_0}$ leads to a higher specific work output ${}^{\Delta h_t}/_{c_p \cdot T_0}$. However, in order to calculate the power output of the gas turbine P_{GT}, the specific work output ${}^{\Delta h_t}/_{c_p \cdot T_0}$ is multiplied by the following parameters: the mass flow rate, the ambient temperature T_0 and the specific heat capacity c_P. As flight altitude is increased, the ambient air temperature T_0 and ambient air density ρ are reduced [43], where the latter results in a lower mass flow rate. According to the equation given in [41], the combination of all relevant effects leads to a reduction of the maximum power as shown in Fig. 3.10, where the gradient of the curve of ${}^{\rho_H}/_{\rho_{H=0}}$ is steeper than the gradient of the curve of ${}^{P_{GT,max,H}}/_{P_{GT,max,H=0}}$.

3.3 Piston engines

Several types of piston engines with different characteristics can be applied in hybrid-electric propulsion systems. In this chapter diesel and gasoline engines are investigated which are used in aerospace applications.

3.3.1 Diesel engines

The data of seven turbocharged, 4-stroke and direct injected diesel engines applied in aviation was obtained and used to analyze the component characteristics. The raw data can be found in table B.2. All engines have a type certificate with the exception of the engine "OM660", which is applied in ultralight airplanes where the engine is certified as part of the airplane.

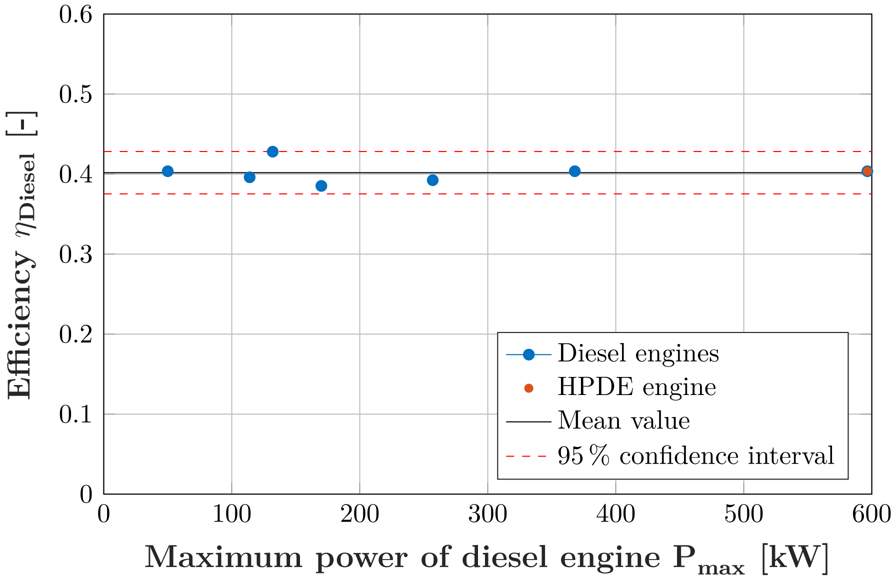

Figure 3.11: Engine efficiency of diesel engines plotted versus maximum rated power

The mean value of the efficiency of the investigated engines is $\eta_{Diesel} = 0.4017$ with a standard deviation of $\sigma = 0.0135$. In Fig. 3.11 it can be observed that the efficiency η_{Diesel} does not correlate with the maximum output power rating P_{max} of the engines. With a t-statistic, it can be confirmed that a correlation between η_{Diesel} and P_{max} is statistically not significant. This is a major difference to the efficiency of gas turbines, which varies as a function of power as discussed in chapter 3.2. Differently to the overall pressure ratio of gas turbines, the compression ratio is not influenced in the investigated power class by the rated power of the engines. According to [3] the efficiency of the

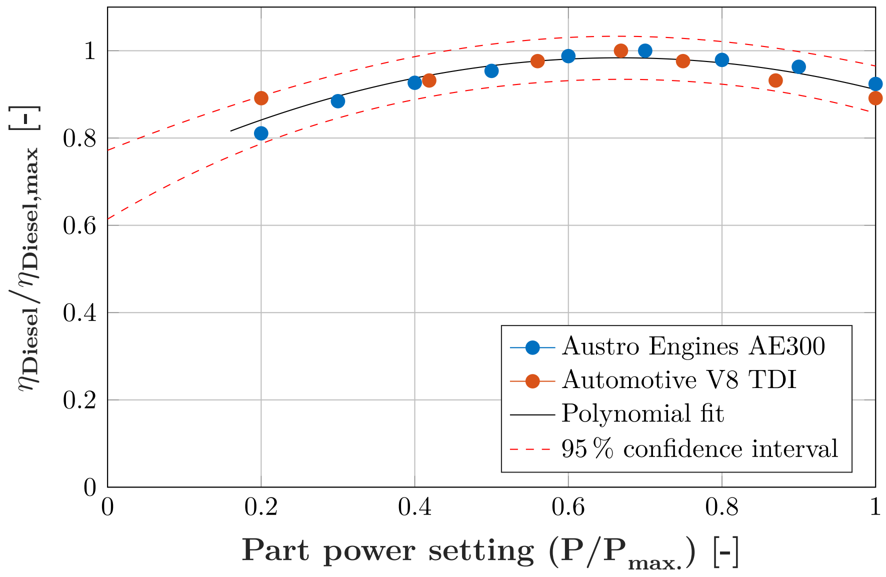

Figure 3.12: Influence of part power setting on the efficiency of diesel engines

thermodynamic cycle increases with the compression ratio up to a value where friction losses and deteriorating combustion chamber geometries decrease the efficiency of the engine. A further difference to gas turbines is that in piston engines, oil lubricated piston rings are applied to seal the cylinders for compression.

The efficiency of piston engines depends on the torque and revolution speed setting. Because the output power of the engine equals the product of torque and revolution speed, different combinations of both parameters can be applied to achieve the same output power. In the following section, the combination of both parameters is applied which features the best efficiency for a specific power setting. This is feasible, as in a serial hybrid-electric aircraft the revolution speed of the combustion engine can be chosen independently from the propeller revolution speed. It can be observed that low power settings are associated with low revolution speeds and high power settings with increased revolution speeds.

In Fig. 3.12 the influence of a part power setting onto the efficiency of the diesel engine η_{Diesel} is shown. A flat peak of η_{Diesel} can be observed at a part power setting of about 70 % of the maximum power. Equation 3.14 was found statistically significant with $R^2 = 0.8477$ and $R^2_{Pred.} = 0.6754$. To justify the trend, several effects have to be considered. The friction loss in a piston engine as well as pressure losses in its air intake system are primarily dependent on the revolution speed [3]. As high power settings are associated with high revolution speeds, the efficiency of the engine decreases. For low power settings, which are associated with low revolution speeds, the magnitude of the friction losses decreases – however, due to the lower output power, the ratio between friction losses and output power increases [3] and consequently the efficiency is lowered.

$$\eta_{Diesel}/\eta_{Diesel,max} = \beta_0 + \beta_1 \cdot \left(\frac{P}{P_{max}}\right) - \beta_2 \cdot \left(\frac{P}{P_{max}}\right)^2 \tag{3.14}$$

Symbol	Unit
$\eta_{Diesel}/\eta_{Diesel,max}$	[-]
P/P_{max}	[-]

Coefficient	Value	Unit	p-value
β_0	0.693	[-]	$0.0000 \cdot 10^{-5}$
β_1	0.8726	[-]	$0.2839 \cdot 10^{-5}$
β_2	0.6546	[-]	$0.6985 \cdot 10^{-5}$

Table 3.6: Units and regression coefficients for the trend curve of the efficiency at part power setting with $R^2 = 0.8477$ respectively $R^2_{pred} = 0.6754$

In Fig. 3.13 the mass of the diesel engines is plotted as a function of the rated maximum output power. The trend in equation 3.15 was found statistically significant. It can be observed that the mass grows linearly with increasing power rating – however, the presence of a dead mass is indicated by the factor β_0. The obtained linear regression function is used to calculate the trend for the mass specific power as shown in the right chart of Fig. 3.13. In order to perform a suitable comparison to gas turbines, it was required to consider the wet mass of the piston engines including all necessary accessories. As some sources state only the dry mass, an estimation of the mass of the engine fluids was needed. This was done by scaling the known engine fluid mass of the engines OM660 and CD-155 and taking the output power as a scaling factor.

$$m_{Diesel} = \beta_0 + \beta_1 \cdot P_{ICE,max} \tag{3.15}$$

Symbol	Unit
m_{Diesel}	$[kg]$
$P_{ICE,max}$	$[kW]$

Coefficient	Value	Unit	p-value
β_0	56.84	$[kg]$	0.0063
β_1	0.9595	$[kg/kW]$	0.0000

Table 3.7: Units and regression coefficients for the trend curve of the mass of diesel engines with $R^2_{pred} = 0.9686$

In Fig. 3.13 the engine "HPDE" is included, which is a diesel engine currently developed by the company Safran S.A. [45]. HPDE stands for "High Power Density Engine" and is a technology demonstrator which was successfully tested on ground. Safran states that the HPDE engine "is a new world class Jet A piston engine leader in power

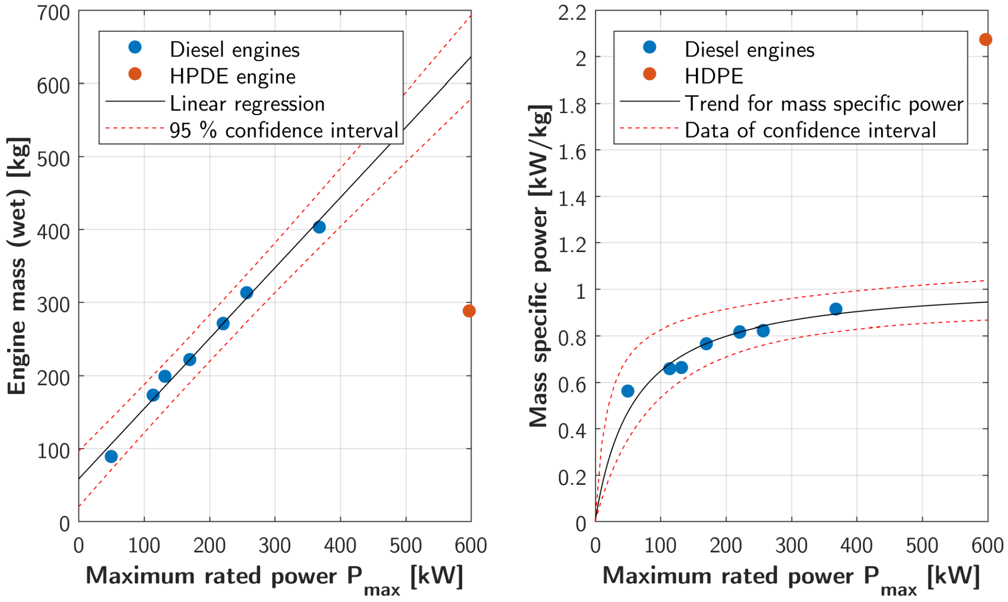

Figure 3.13: Mass of diesel engines plotted versus maximum rated power (left); mass-specific power calculated with data of linear regression (right)

density, and an ideal solution for the power generation and hybrid propulsion for future small and mid-size commuter-aircraft, rotorcraft and drones". The engine was not included into the calculation of the trend curve as it is still in the prototype phase. However, it will be used at a later stage in the process of the preliminary aircraft sizing as a technology scenario.

Piston engine assemblies require an engine mount which consists of e.g. a space frame and shock mounts. In addition, the installation of an air induction system is needed, which consists of air ducts from the inlet of the engine fairing to the engine itself and the duct support structure. From data given [46] for eight single engine aircraft equipped with a piston engine[2] it is deduced that the additional engine installation mass depends on the mass of the applied piston engine. For an installation the required additional mass is determined to be 12.2 % of the mass of the piston engine with a standard deviation of $\sigma = 2.2\,\%$.

With increasing flight altitude, the maximum power of naturally aspired piston engines decreases as the density of the ambient air lowers and less air molecules enter the cylinder. Turbochargers are used in aviation to counteract the reduced air density at altitude. The value of the critical altitude of turbocharged engines describes up to

---

[2] Data available for: Cessna 150, Cessna 172, Cessna 175, Cessna 182, Beech J-35, Rockwell 112 TCA, Cessna 210J

which altitude the engine can deliver its normal rated power. If the flight altitude is increased further, the maximum power output is reduced similarly to naturally aspired piston engines.

For the turbo-charged diesel engines AE300 and CD-155 the power available at a specific altitude is available [47] [48]. In Fig. 3.14 the fraction between available power and maximum rated power at sea level P/P_{max} is plotted versus the flight altitude. The mean value for the critical altitude is $H_{crit} = 2,743\,m$ and will be used in the consideration of turbo-charged diesel engines. For the loss of power for higher altitudes than the critical altitude, a mean power loss of 7.6 percentage points of rated maximum power per 1,000 m was determined. This value is in the same order of magnitude as the standardized reduction of ambient air density according to ISA, which is 7.8 percentage points per 1,000 m of flight altitude. This can be justified as the maximum power of a diesel engine correlates to maximum torque at a specific engine speed, where the maximum torque is driven by the maximum amount of diesel entering the cylinder [49]. The maximum amount of diesel is limited by the lowest practical air-fuel ratio λ, which is driven by the soot limit of the diesel combustion. The soot limit is associated with a significantly increased amount of unburnt diesel leaving the combustion chamber. Consequently, as the minimum air-fuel ratio λ is limited, the maximum amount of fuel entering the combustion chamber depends on the density of the ambient air. As a result, the maximum power decreases above the critical altitude due to the decreasing ambient air density.

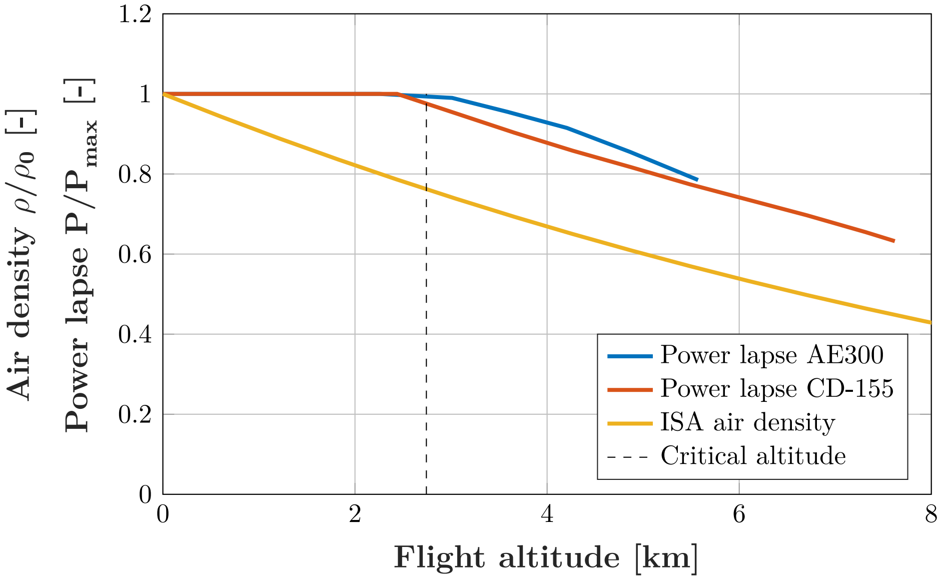

Figure 3.14: Power lapse of diesel engines AE300 [47] and CD-155 [48] and ISA air density [43] plotted versus altitude

3.3.2 Gasoline engines

The data of 17 gasoline 4-stroke engines based on the Otto cycle is investigated. All engines have a type certificate and are applied in general aviation aircraft which are in production in the year 2019. In Fig. 3.15 the maximum efficiency is plotted versus the maximum rated power: it can be observed that the efficiency of the gasoline engines is lower than the efficiency of the diesel engines. This can be justified by the consideration of several effects. Firstly, the efficiency of the idealized thermodynamic cycle of gasoline engines, the Otto cycle, is lower than the idealized Diesel cycle, when the same maximum pressure and temperature are applied [50]. Secondly, the efficiency of both cycles benefit from an increased compression ratio [50]. However, for the investigated gasoline engines, which possess a carburettor or a indirect fuel injection system, the compression ratio is limited due to spontaneous self-ignition of the fuel-air-mixture which leads to so called "engine knocking" [51]. As a result, the turbo-charged gasoline engines possess a mean compression ratio of only 7.4. According to [51] the compression ratio of modern gasoline engines is limited to $\sim$ 10. For the investigated turbo-charged diesel engines a mean compression ratio of 16.7 can be determined. Compared to diesel engines, the efficiency of the investigated gasoline engines is lowered further, as the engines are equipped with a throttle valve, which contributes an additional air intake loss.

In Fig. 3.15 it can be observed that the maximum efficiency of the investigated gasoline engines varies considerably more compared to the efficiency of the diesel engines. If all gasoline engines are taken into account, the standard deviation of the maximum efficiency is $\sigma_{gasoline} = 0.0277$ compared to the corresponding value of diesel engines $\sigma_{diesel} = 0.0135$. A reason could be that not all gasoline engines are equipped with an electronic control unit (ECU) and a turbocharger which is the case for the investigated diesel engines. Nonetheless, no correlation could be found between the presence of an ECU or a turbocharger and the maximum achievable efficiency of the engine. However, in contrast to diesel engines, gasoline engines can be operated in a fuel rich mode [52] without the excessive formation of soot. In the fuel rich operation the air-fuel ratio λ drops below the value of stoichiometric combustion of $\lambda = 1$ and less oxygen is present in the combustion chamber than it is required for a complete combustion. As a result, not all fuel can be burnt, which decreases the fuel efficiency. Instead the remaining fuel is vaporized and increases the cooling of the engine components. The extent to which a gasoline engine uses this fuel rich operation affects the resulting efficiency. The fuel rich operation cannot be applied to diesel engines as the corresponding combustion requires air-fuel ratios $\lambda > 1$ [53] in order to prevent the excessive formation of soot. Apart from the described differences, it can be observed that similarly to diesel engines

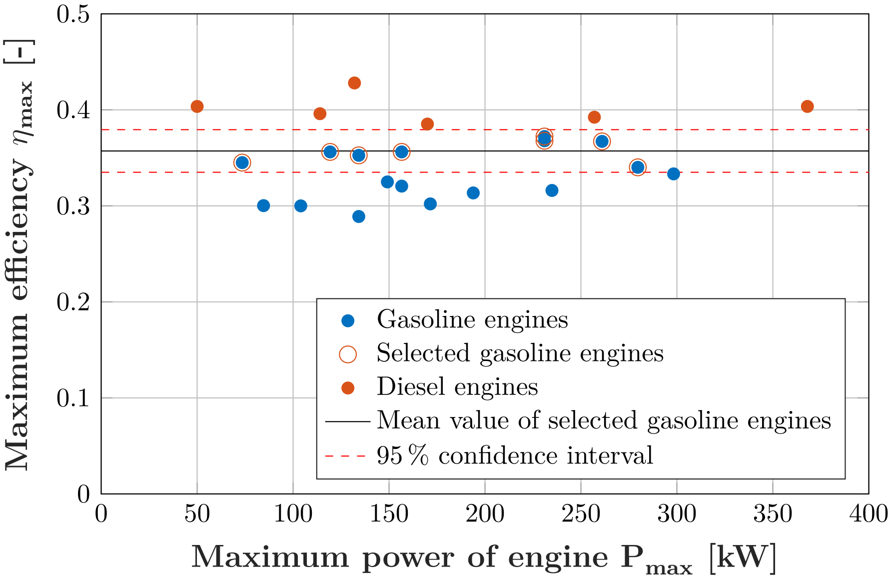

Figure 3.15: Efficiency of gasoline and diesel engines plotted versus maximum shaft power, data of the considered gasoline engines can be found in table B.3

no significant correlation between maximum power and observed maximum efficiency is found in the investigated power range of the gasoline engines.

In order to estimate the potential of the efficiency of gasoline engines accurately, only gasoline engines are used for the further investigation which are in the upper 50-percentile of the maximum efficiencies η_{max} as shown in Fig. 3.15. The mean value of the resulting data set is $\eta_{max} = 0.3572$ with a standard deviation of $\sigma_{gasoline} = 0.0113$, which is in the same order of magnitude as the corresponding value of diesel engines $\sigma_{diesel} = 0.0135$. The determined efficiency is plausible, as it is slightly lower than the maximum efficiency of gasoline engines $\eta_{max} = 0.36$ stated in literature of [3].

In Fig. 3.16 the mass specific power is plotted versus the maximum power of the engines. For comparison purposes the mass specific power of diesel engines is plotted as a reference. It can be observed that the specific power of the investigated gasoline engines is higher than the specific power of the diesel engines – consequently, a gasoline engine possesses a lower mass than a diesel engine, if both have the same output power. This can be justified with the lower compression ratio of the gasoline engines, which leads to lower internal pressure loads. As a result the engine block requires less load bearing structure. A statistically significant influence of the maximum rated power on the specific power of the gasoline engines is not given – the mean mass specific power of the considered gasoline engines is 1.043 kW/kg with a standard deviation of $\sigma = 0.078$ kW/kg.

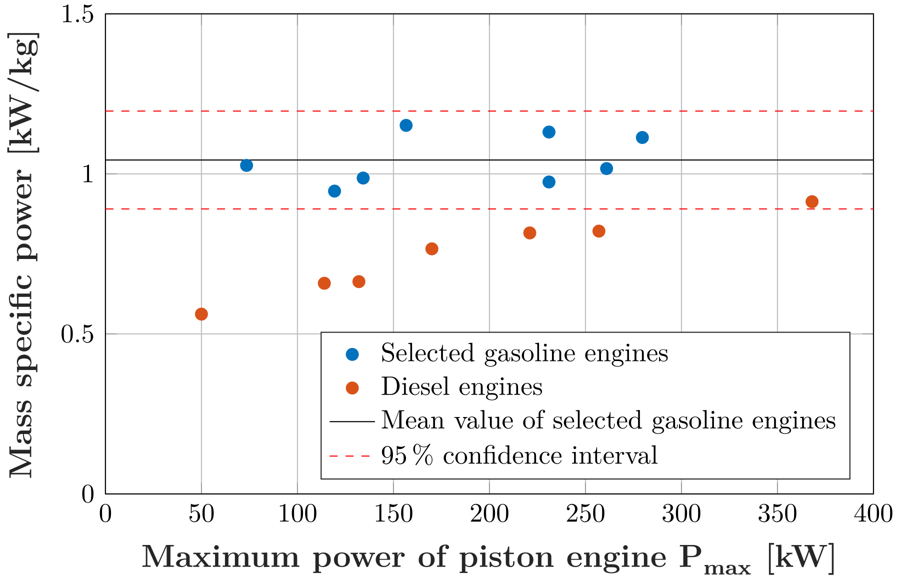

Figure 3.16: Mass specific power of gasoline and diesel engines plotted versus maximum shaft power, data summarized in table B.3

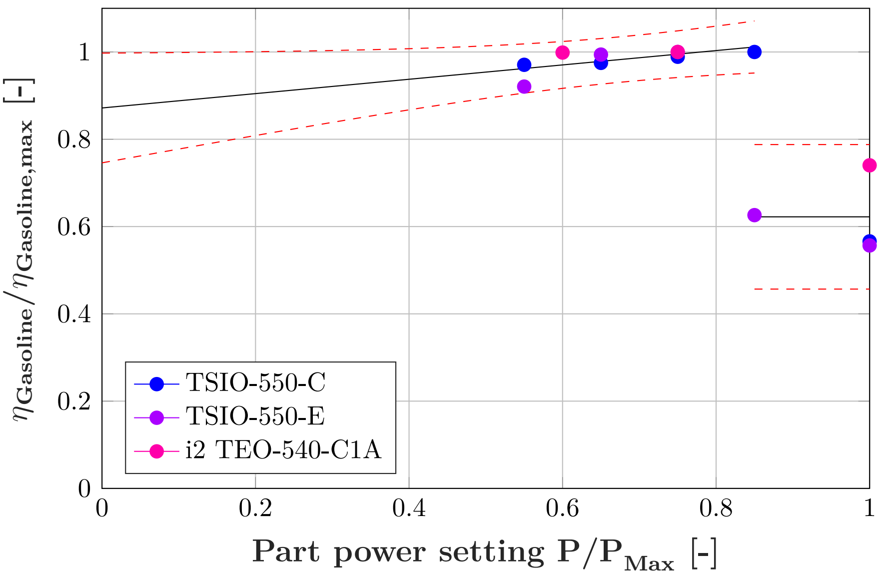

Figure 3.17: Influence of part power setting on the efficiency of turbo-charged gasoline engines [54] [55]

When operating gasoline engines, the best efficiency is usually not reached at full power setting. In Fig. 3.17 the influence of the part power setting on the efficiency of the investigated aviation gasoline engines is shown. For the investigation only gasoline engines equipped with a turbo-charger are used in order to make an appropriate comparison to diesel engines, which are all turbo-charged. The mean critical altitude of the investigated turbo-charged gasoline engines is $H_{crit} = 2,844\,m$ ($\sigma = 1155\,m$) and is in the same order of magnitude as the critical altitude of the investigated diesel engines.

In Fig. 3.17, it can be observed that the turbo-charged gasoline engines achieve the highest efficiency between 60 % and 80 % of the maximum power. Differently to diesel engines, the efficiency at full power setting is considerably lower than the best efficiency. The trend can be justified by the consideration of several effects – similar to diesel engines, the fraction between friction losses and power output is increased at low part power settings and thus the engine efficiency is reduced. For gasoline engines further throttle losses occur at low part power settings, as the partially closed throttle valve contributes an increased pressure loss. Contrary, at higher part power settings, which are associated with higher revolution speeds, the timing of ignition has to be postponed in order to avoid engine knocking, which leads to a lower efficiency [3]. The significantly reduced efficiency at maximum power setting is mainly a result of the fuel rich operation of the gasoline engines, in which the cooling of the engine is increased by the vaporization of unburnt fuel. Consequently, the efficiency at maximum power setting is considerably lower than the efficiency at part power setting, which is a different characteristic compared to diesel engines as shown in Fig. 3.12.

3.3.3 Summary of piston engines and gas turbines

In table 3.8 the characteristics of the considered piston engines and the investigated gas turbines with an output power up to 2 MW are summarized. It can be observed that the piston engines achieve a higher efficiency compared to the gas turbines in the considered power class. The magnitude of the efficiency of the piston engines depends strongly on whether a Otto or Diesel thermodynamic cycle is applied – an impact of the rated power on the achievable efficiency is not statistically significant. The investigated piston engines are, however, considerably heavier as their mass specific power is lower compared to the investigated gas turbines. Differently to piston engines, a tentative technology limitation was identified for the gas turbines, where the maximum observed overall pressure ratio correlates significantly with the maximum rated power. Similarly, the maximum observed efficiency and the mass specific power of the gas turbines increase with increasing rated power. A further difference to the piston engines is a beneficial effect of the flight altitude on the efficiency of the gas turbine.

	Piston engines	**Gas turbines**
Achievable efficiency	~40.2 % (diesel) ~35.7 % (gasoline)	from 10.7 % to 31.3 %
Mass specific power	0.6 kW/kg to 0.9 kW/kg (diesel) ~1.0 kW/kg (gasoline)	2.8 kW/kg to 7.7 kW/kg
Best efficiency at	~ 75 % power	~ 100 % power
Beneficial effect of flight altitude on efficiency	no	yes

Table 3.8: Comparison of the investigated piston engines and gas turbines up to a maximum rated power of 2 MW

3.4 Battery system

3.4.1 Battery cells

The mass specific energy $E_{s,Bat}$ and the mass specific power $P_{s,Bat}$ are two important performance figures of battery cells which are affecting the mass of a hybrid-electric propulsion system. To investigate the relationship between $E_{s,Bat}$ and $P_{s,Bat}$, the data of modern battery cells, which are commercially available, was obtained from the data sheets summarized in table B.4. In order to ensure a statistically significant trend curve, the following selection criteria were applied:

- Investigation of battery cells of the format 18650, which is widely applied in laptops and electric vehicles
- Battery cells with an introduction data later than 2013
- Data obtained from data sheets of the manufacturers
- No re-branded battery cells – only cells from original manufacturers

As the mass of propulsion components has a significant impact on aircraft performance, only battery cells are considered which possess an increased specific energy $E_{s,Bat}$ and/or specific power $P_{s,Bat}$ near the technology envelope shown in the Ragone plot in Fig. 3.18. The discharge capacity of the investigated battery cells is given for different constant discharge currents in the data sheets listed in table B.4. As the cell voltage drops during the discharge process, the discharge power decreases steadily for a constant discharge current. Further, the discharge capacity is typically expressed in ampere-hours – however, in order to calculate the corresponding discharge energy, a mean battery cell voltage is required or, if a precise result is needed, an integration of the discharge curves has to be carried out. Hence, the discharge curves from the data sheets were digitized and the discharge energy was calculated by an integration of the curves. Furthermore, a mean power was calculated and the mass specific power $P_{s,Bat}$ and mass specific energy $E_{s,Bat}$ were determined with the mass of the battery cells. In Fig. 3.18 both parameters are plotted for the different battery cells in a Ragone plot. It can be observed that battery cells with highest mass specific energy reach low specific power compared to cells with lower mass specific energy. A positive convex envelope can be found and a trend curve is calculated for the points which lay on the envelope. The curve states the maximum mass specific power available for a certain mass specific energy and equation 3.16 was found statistically significant.

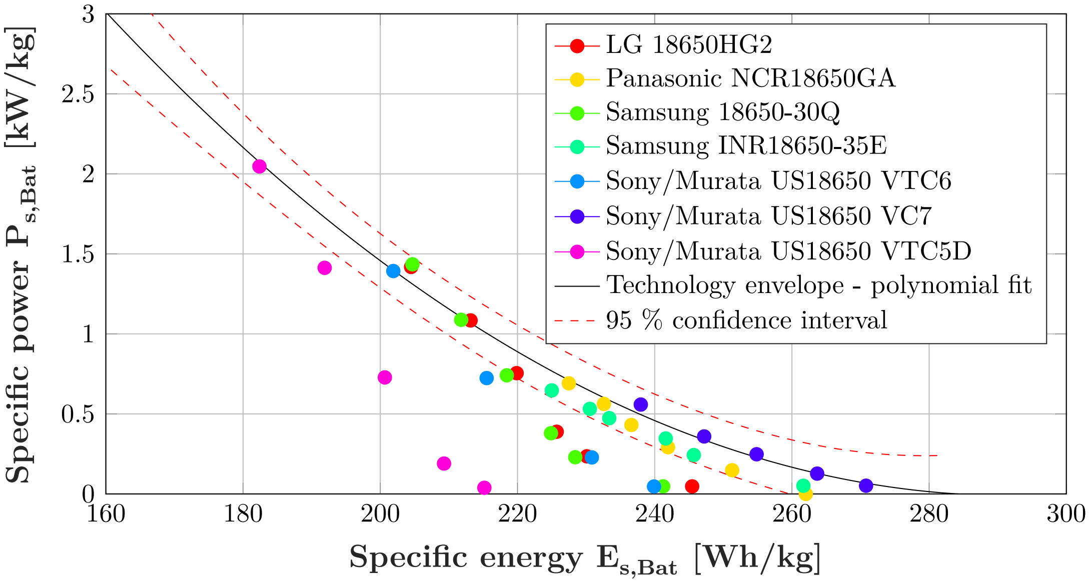

Figure 3.18: Specific energy and power plotted for different battery cells, data from table B.4

$$P_{s,Bat,max} = \beta_0 + \beta_1 \cdot E_{s,Bat,min} + \beta_2 \cdot E_{s,Bat,min}^2 \tag{3.16}$$

Symbol	Unit
$P_{s,Bat,max}$	$[kW/kg]$
$E_{s,Bat,min}$	$[Wh/kg]$

Coefficient	Value	Unit	p-value
β_0	14.78	$[kW/kg]$	$0.0067 \cdot 10^{-3}$
β_1	−0.1013	$[kW/Wh]$	$0.0486 \cdot 10^{-3}$
β_2	0.0001734	$[kW \cdot kg/Wh^2]$	$0.286 \cdot 10^{-3}$

Table 3.9: Units and regression coefficients for the trend curve of the specific power of battery cells with $R^2 = 0.9896$

The specific energy of a particular battery cell decreases as more power is drawn from it. In case of the battery cell "Sony/Murata US18650 VC7", which possesses the highest mass specific energy of the investigated cells, a reduction of approximately 12 % is observed, when the cell is discharged with $P_{s,Bat} = 0.5\,\text{kW/kg}$ compared to when it is discharged with very low mass specific power. In Fig. 3.18 it can be observed that for the investigated battery cells, the reduction of specific energy of a particular battery cell decreases with increasing maximum specific power $P_{s,Bat,max}$ of the battery cell. E.g. the reduction of specific energy of the cell "Sony/Murata US18650 VC7", possessing the lowest maximum specific power, is highest compared to the rest of the battery cells. This relation is investigated by fitting the linear trend curve, shown

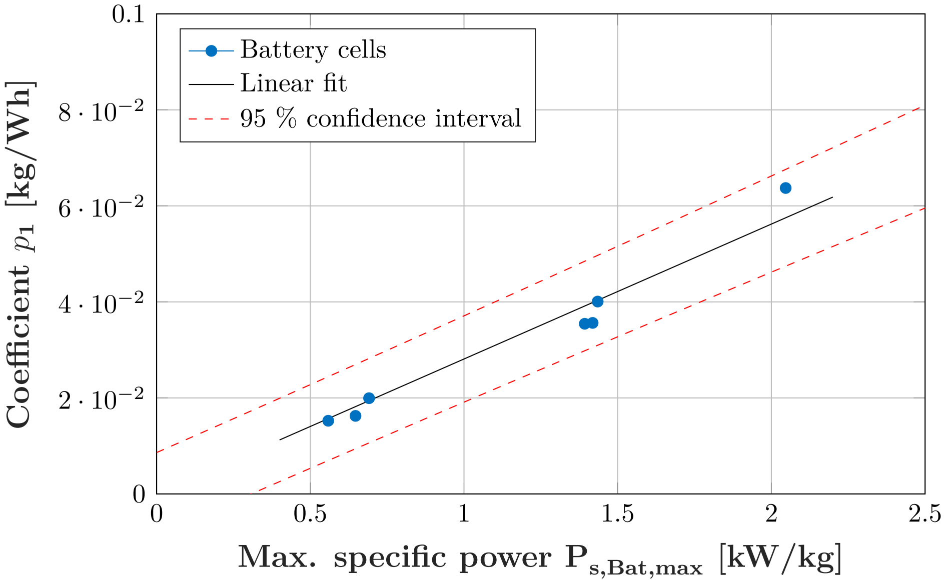

Figure 3.19: Coefficient p_1 plotted versus maximum specific power of corresponding battery cell

in equation 3.17, into the individual data of every battery cell. The coefficient of determination R^2 for each battery cell is given in table B.5 and a strong correlation is found for each cell. When plotting the gradient p_1 of each battery cell as a function of the corresponding maximum specific power $P_{s,Bat,max}$ of the different battery cells, a correlation can be observed as seen in Fig. 3.19 and the linear trend in equation 3.18 was found significant. The identified trend of a reduced discharge capacity, as more power is drawn from the battery cell, is similar to Peukert's law which is applicable for lead-acid batteries. According to [56], Peukert's law is further only valid for battery cells discharged at constant temperature and constant discharge current. However, at high discharge currents the battery cell temperature increases significantly.

$$P_{s,Bat} = p_0 - p_1 \cdot E_{s,Bat} \tag{3.17}$$

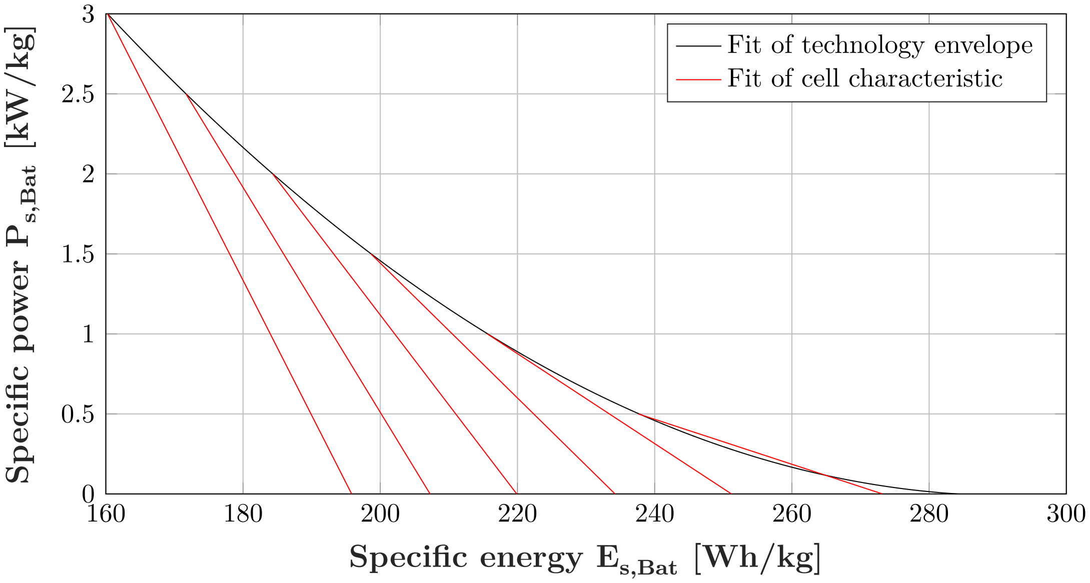

Figure 3.20: Generalized battery cell model containing the technology envelope from equation 3.16 and the cell characteristic from equation 3.17

$$p_1 = \beta_3 \cdot P_{s,Bat,max} \tag{3.18}$$

Symbol	**Unit**
p_1	$[{}^{kW}/_{Wh}]$
$P_{s,Bat,max}$	$[{}^{kW}/_{kg}]$

Coefficient	**Value**	**Unit**	**p-value**
β_3	0.0281	$[{}^{kg}/_{Wh}]$	$3 \cdot 10^{-7}$

Table 3.10: Units and regression coefficients for the trend curve of the coefficient p_1 of battery cells with $R^2 = 0.9579$

The found trends can be justified by considering the power loss during discharge of a battery cell and the associated heat generation. The power loss is proportional to the internal resistance of the battery cell and the square of the discharge current. [57] states that the main limiting parameter for the power output of a lithium ion battery cell is its internal resistance. Similarly, in [58] it is shown that the maximum power of a battery cell is approximately inversely proportional to the battery cell's internal resistance. The internal resistance varies with the state-of-charge of the battery cell as well as its temperature [57]. According to [58] the internal resistance of a battery cell consists of the ohmic internal resistance and the polarization resistance, where "the ohmic resistance comes mainly from the electrode materials, the electrolyte, the resistance of the separator, and the resistance contacting with other elements". Experimental data in [59] shows that battery cells in the 18650-format with high mass specific power possess thinner and therefore longer electrodes than battery cells which are optimized for mass specific energy. As a result, the electrode surface area is larger in these battery cells. As the ohmic resistance is inversely proportional to the cross-sectional area of the conductor [60], in this case the surface area of the electrodes, the internal ohmic resistance of these battery cells is lower. Thus, the power output of these cells can be increased. However, thinner electrodes have the disadvantage that the fraction of inactive components such as insulation and conducting aids are increased lowering the mass specific energy of the battery cell [61].

With equation 3.16 for the envelope of specific energy and specific power and equation 3.17 for the reduction of specific energy of a particular cell, a battery cell model, shown in Fig. 3.20, can be obtained. To verify the model, the coefficient of determination R^2 for each battery cell is given in table B.5 and a strong correlation is found for each cell. Furthermore, in table B.5 the error of the maximum predicted specific energy $E_{s,Bat,max}$ is given, showing low errors. Both parameters indicate that the battery cell model is suitable for the design process of the hybrid-electric propulsion system.

3.4.2 Power requirement for battery systems

The power of battery systems can be calculated by multiplying the mass of the battery system m_{Bat} with the mass specific energy of the battery cells $P_{s,Bat,max}$ and the integration factor α_{Int} as shown in equation 3.19. The integration factor α_{Int} represents the fraction between the mass of the installed battery cells and the mass of the entire battery system. Therefore, the factor describes the required additional mass for mechanical structures, internal wiring, battery monitoring systems, fuses, cooling systems, firewalls etc. The integration factor α_{Int} depends on the requirements of the application and the applied technologies. In table 3.11 integration factors and requirements for two different battery systems are documented. In a serial hybrid-electric aircraft a fraction of the maximum shaft power driving the propeller $P_{sh,max}$ is contributed by the battery system. The fraction between battery power and total shaft power is referred to as power split S_{TO}, defined in equation 3.20, and will be later used as a design parameter to describe the hybrid propulsion system.

$$P_{Bat,max} = \alpha_{Int} \cdot m_{Bat} \cdot P_{s,Bat,max} \tag{3.19}$$

$$S_{TO} = \frac{\eta_{EM} \cdot P_{Bat,max}}{P_{sh,max}} \tag{3.20}$$

Parameter	**System #1**	**System #2**
Integration factor α_{Int}	0.88	0.80
Cooling power	Low	High
Firewall	No	Yes

Table 3.11: Integration factors α_{Int} for different types of battery systems, data gathered in the project e-Genius of the University of Stuttgart

$$P_{sh,max} = \left({}^{P_{max}}\!/_{m_{MTO}}\right) \cdot m_{MTO} \tag{3.21}$$

The required maximum shaft power of an aircraft $P_{shaft,max}$ can be written as the product of maximum take-off mass m_{MTO} and the required power loading $\left({}^{P_{max}}\!/_{m_{MTO}}\right)$. The power loading is an important parameter in airplane design and is the result of a flight performance calculation [62]. By combining equations 3.19, 3.20 and 3.21, a formulation for the required specific power of the battery cells $P_{s,Bat,max}$ can be found as shown in equation 3.22. Similar to the fuel fraction [4], a battery fraction $\xi_{Bat} = \left({}^{m_{Bat}}\!/_{m_{MTO}}\right)$ is introduced, describing which portion of the maximum aircraft mass m_{MTO} is designated to the battery system.

$$P_{s,Bat,max} = \frac{S_{TO} \cdot \left({}^{P_{max}}\!/_{m_{MTO}}\right)}{\xi_{Bat} \cdot \eta_{EM} \cdot \alpha_{Int}} \qquad \text{with} \qquad \xi_{Bat} = \frac{m_{Bat}}{m_{MTO}} \tag{3.22}$$

The required mass specific power on battery cell level $P_{s,Bat,max}$ can be drawn into the Ragone plot as a minimum requirement. Only battery cells which possess a higher mass specific power $P_{s,Bat,max}$ are suitable for the application. In Fig. 3.21, the requirements to the specific power for different battery mass fractions are shown for the electric aircraft e-Genius. With data from table 2.2, a power loading ${}^{P_{max}}\!/_{m_{MTO}} = 71.4$ W/kg is determined[3]. It is assumed that the power required for take-off can be provided solely by the battery system ($S_{TO} = 1$) in order to cover a possible failure of the single combustion engine in the hybrid-electric propulsion system. From the plot, it can be deduced that even if a battery mass fraction of 0.06 would be selected for the hybrid-electric aircraft, battery cells with an increased specific power are required for the application.

---

[3] Further parameters of the calculation: integration factor $\alpha_{Int} = 0.80$, efficiency of electric motor including its inverter $\eta_{EM} = 0.94$

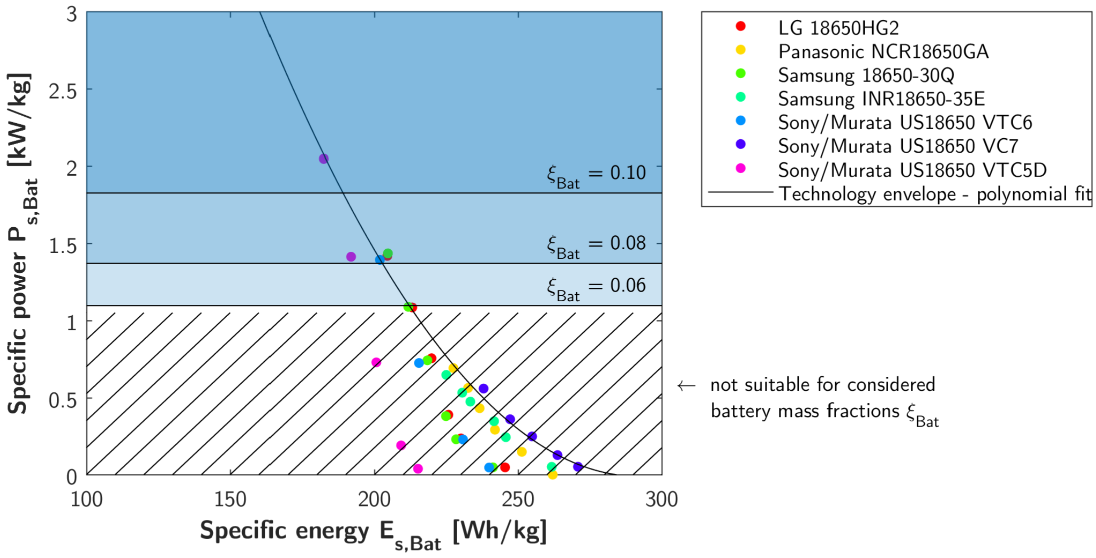

Figure 3.21: Influence of different battery mass fractions on the required maximum specific power on battery cell level for the electric aircraft e-Genius

3.4.3 Energy requirement for battery systems

The required mass specific energy on battery cell level $E_{s,Bat}$ is calculated by dividing the required battery energy on aircraft level E_{Bat} by the considered battery mass fraction ξ_{Bat}, the integration factor α_{Int}, the capacity fade factor α_{Deg} and the aircraft mass m_{MTO} as shown in equation 3.23. With the factor α_{Deg} the impact of a fade of the battery capacity due to charge and discharge cycles is included, as the discharge capacity is limited to a fraction of the maximum capacity in order to increase battery life and reduce battery depreciation cost.

$$E_{s,Bat} = \frac{E_{Bat}}{\alpha_{Int} \cdot \alpha_{Deg} \cdot \xi_{Bat} \cdot m_{MTO}} \qquad \text{with} \qquad \xi_{Bat} = \frac{m_{Bat}}{m_{MTO}} \tag{3.23}$$

The amount of energy a battery cell provides during discharge decreases as more power is drawn from the cell as described in section 3.4.1. In order to determine this specific discharge capacity of the battery cell, a mean power level $P_{Average}$ has to be calculated for the flight mission. An approach in preliminary battery sizing of battery electric cars [63] and smartphones [64] is to assume a weighted arithmetic mean power, which can be calculated by equation 3.24. Consequently, an average mass specific power $P_{s,Bat,avg}$ on battery cell level can be deduced as shown in equation 3.25.

$$P_{Bat,Average} = \sum_{i=0}^{n} \frac{P_{Bat,i} \cdot \Delta t_i}{\Delta t_{Mission,Bat}} = \sum_{i=0}^{n} \frac{E_{Bat,i}}{\Delta t_{Mission,Bat}} \tag{3.24}$$

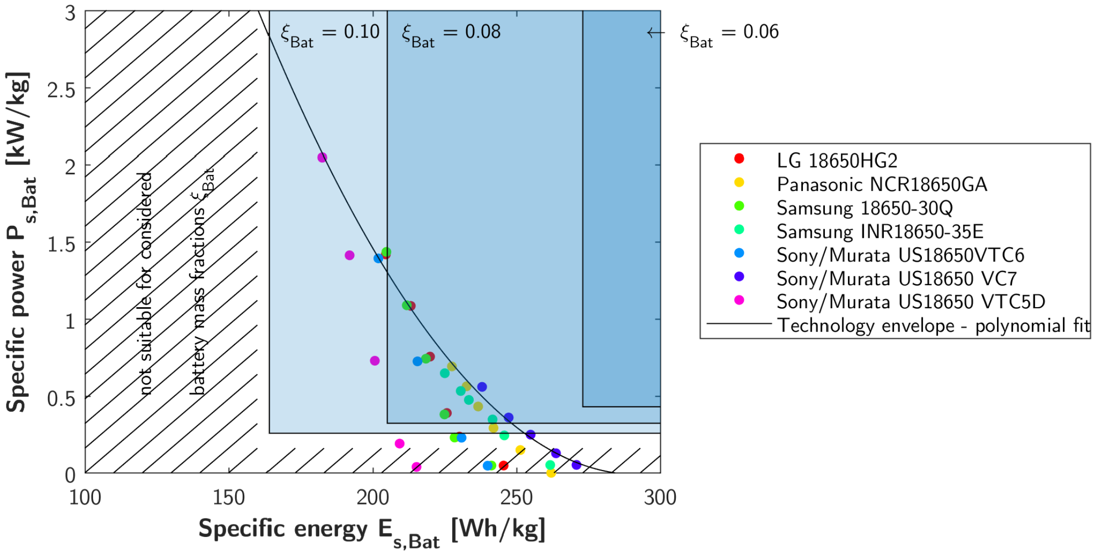

Figure 3.22: Required specific energy and specific power in the Ragone plot for a battery driven reserve flight of the aircraft e-Genius – limitations are plotted for different battery mass fractions

$$P_{s,Bat,avg} = \frac{P_{Average}}{\xi_{Bat} \cdot \eta_{EM} \cdot \alpha_{Int} \cdot m_{MTO}} \qquad \text{with} \qquad \xi_{Bat} = \frac{m_{Bat}}{m_{MTO}} \tag{3.25}$$

The two requirements for the specific energy $E_{s,Bat}$ and the average specific power $P_{s,Bat,avg}$ drawn from the cell, can be plotted into the Ragone plot shown in Fig. 3.22. Consequently, suitable battery cells, which meet the energy demand of the application, can be identified. In Fig. 3.22 the requirements are plotted for three different battery mass fractions – it can be observed how the number of battery cells fulfilling the described requirements drops as the battery mass fraction is reduced. In the exemplary case shown, it can be deduced that a battery mass fraction of $\xi_{Bat} = 0.06$ would not be sufficient as no suitable battery cell would be available. For the calculation of the required battery energy E_{Bat} and the mean battery power level $P_{Bat,Average}$, an e-Genius flight profile is taken as a basis, consisting of a take-off, a climb flight to 1,000 ft altitude and a horizontal flight of 30 minutes with a cruise speed of 150 km/h. By considering this flight profile, the effects of a failure of the combustion engine during take-off in the hybrid-electric propulsion system could be mitigated, because a safe landing including a holding flight can be carried out solely by the battery system. For the calculation, the drag polar given in section 4.1.3 is applied and the aircraft parameters given in table 2.2 are used[4].

---

[4] Further parameters of the calculation: capacity fade factor $\alpha_{Deg} = 0.9$, integration factor $\alpha_{Int} = 0.80$, mean efficiency of electric motor including its inverter $\eta_{EM} = 0.94$

3.5 Electric motor assembly

An electric propulsion system consists of an electric machine, an inverter and various sub-systems shown in Fig. 3.23. In order to compare the mass of a combustion engine to the mass of an electric motor, the mass of these required additional components needs to be taken into account.

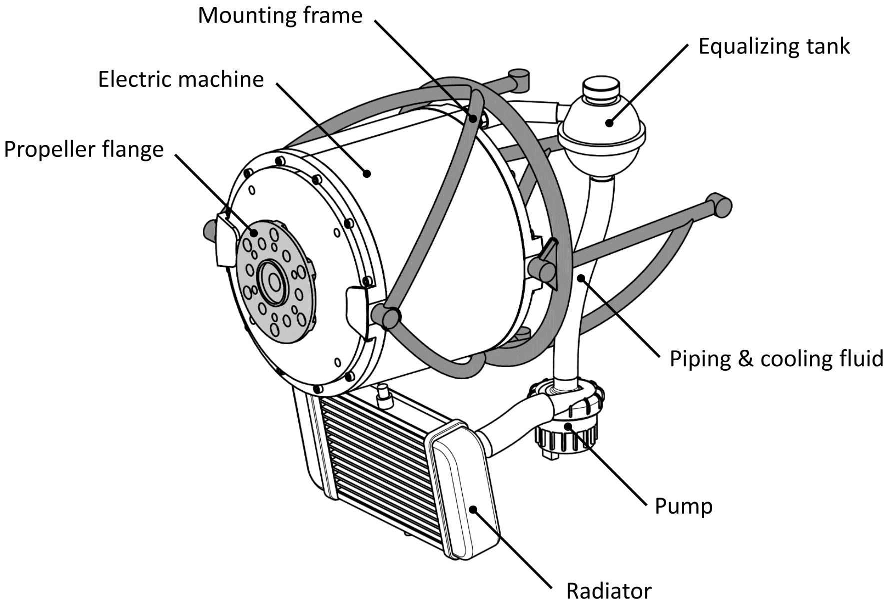

Figure 3.23: Drawing of an aerospace installation of an electric motor with required sub-systems

3.5.1 Electric machine

In a series hybrid-electric aircraft, the propulsive power needed for flight is provided by a propeller which is driven by an electric motor. Furthermore, an electric machine coupled to a combustion engine is applied as a generator. The data of eight electric motors, summarized in table B.6, is investigated, which are designed specifically for aviation propulsion. All motors are synchronous electric machines and drive the propeller directly without a reduction gear box and all motors are equipped with a liquid cooling system. The motors made by "Emrax" are available with air or combined cooling – in order to predict scaling laws correctly, only liquid-cooled models are considered. Furthermore, the electric motors made by Emrax and the "SP260D-A" require an additional adapter for the attachment of a propeller. Consequently, the mass of the motors is increased by a fraction of 15 %, which is derived from data of the project e-Genius

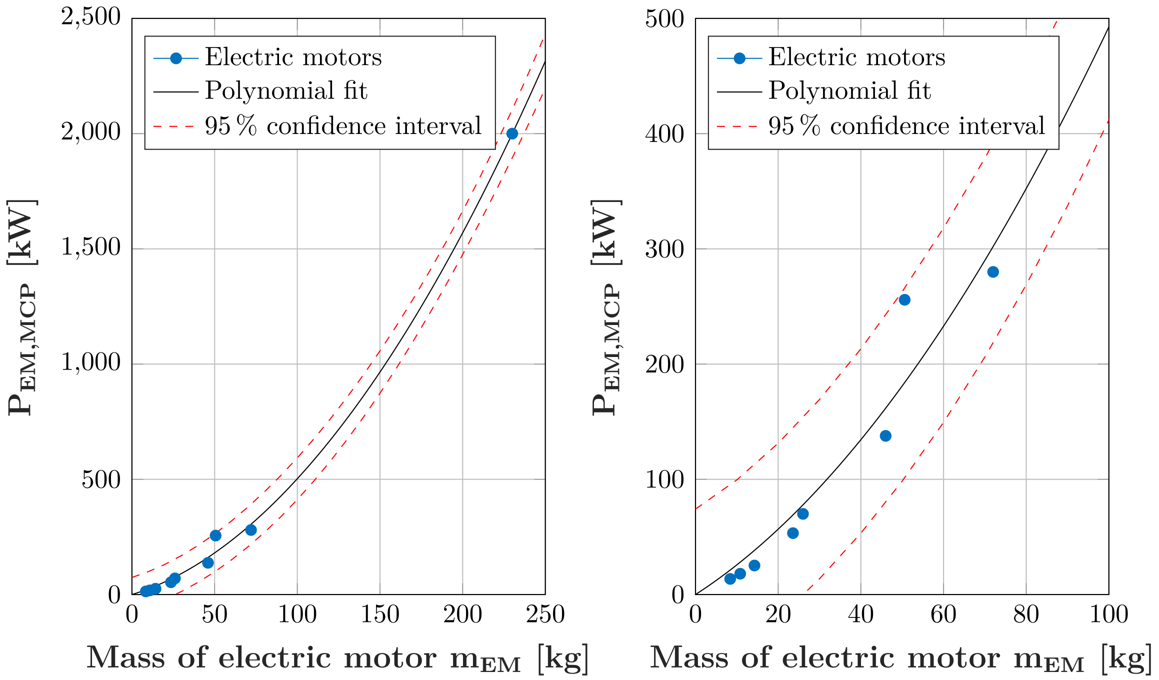

Figure 3.24: Rated power plotted versus mass of electric motors

by the University of Stuttgart. As the electric motors drive the propeller directly, the output power is in some cases limited by the maximum number of revolutions the propeller can operate. Therefore, the rotational speed of the propellers investigated in section 3.7 is used. In Fig. A.4 the propeller rotational speed at highest power rating is plotted versus the corresponding power setting. It can be observed that the maximum revolution speed lowers as the power rating is increased. As a result, the power rating of some electric motors had to be reduced as their maximum power output occurs at higher speeds than a direct driven propeller can be operated.

$$P_{EM,MCP} = \gamma_1 \cdot m_{EM} + \gamma_2 \cdot (m_{EM})^2 \tag{3.26}$$

Symbol	**Unit**
m_{EM}	$[kg]$
$P_{EM,MCP}$	$[kW]$

Coefficient	**Value**	**Unit**	**p-value**
β_1	2.314	$^{kW}/_{kg}$	0.0011
β_2	0.02613	$^{kW}/_{kg^2}$	0.0000

Table 3.12: Units and regression coefficients for the trend curve of the power of the investigated electric motors with $R^2_{Pred} = 0.9941$

In Fig. 3.24 the power of the investigated electric motors is plotted versus the corresponding mass. Two scales are used to evaluate the quality of the fitted curves up to 300 kW and up to 2,000 kW. It can be observed that the specific power increases with increasing power rating of the electric machines. The trend curve in equation 3.26 was found statistically significant. The highest rated power of the investigated electric motors is 280 kW. In order to predict the mass of scaled motors with a higher power rating, the preliminary data [7] of an electric motor, which is currently in development, with a rated power of 2,000 kW is used. In Fig. A.2 the impact of this data point on the gained trend curve is investigated and a low influence is observed.

Several explanations can be found to justify the trend curve in equation 3.26. According to [65] the power of an electric machine is proportional to the length of the rotor, the square of the rotor diameter, the rotor speed and a factor of usage. Accordingly, the power of an electric machine increases if the length of the rotor increases – however, the shape and mass of the end winding stays constant and, consequently, the power to mass ratio improves. Furthermore, a graphic interpretation of the described relation is that the power is related to the volume of the electric machine. The trend curve determined in Fig. 3.24 suggests that the mass of the electric machine is not directly proportional to the volume of the electric machine and no constant volumetric mass density can be assumed. This might be the result of a light weight construction potential which is growing with increasing rated power and allows e.g. the application of hollow drive shafts and mass optimized internal rotor structures.

For the installation of an electric motor a mounting structure is required. In absence of suitable data, it is assumed that, similarly to piston engines, described in section 3.3.1, 12.2 %[5] of the motor mass is required for space frames, motor mounts etc.

In Fig. A.3 the maximum efficiency of the motors is plotted versus the corresponding maximum continuous shaft power. It can be observed that, in contrast to gas turbines, the power rating has no influence on the maximum efficiency. The mean value of the maximum efficiency is $\eta_{EM,max} = 0.954$ with a standard deviation of $\sigma = 0.0085$ for the investigated electric machines. In Fig. 3.25 the efficiency of a synchronous electric machine with its inverter is plotted versus torque setting and shaft speed. A reduced efficiency can be observed for low shaft speeds and increased torque settings. However, when comparing the efficiency at the specific operating points during take-off, climb and cruise flight, it can be observed that efficiencies vary by only 0.74 percentage points as summarized in table B.7. In the sizing process of the hybrid-electric propulsion system, it will be assumed therefore that the electric motor with its inverter possesses the mean efficiency of 94.0 %.

---

[5] Numerical value derived from installation mass data available [46] for: Cessna 150, Cessna 172, Cessna 175, Cessna 182, Beech J-35, Rockwell 112 TCA, Cessna 210J

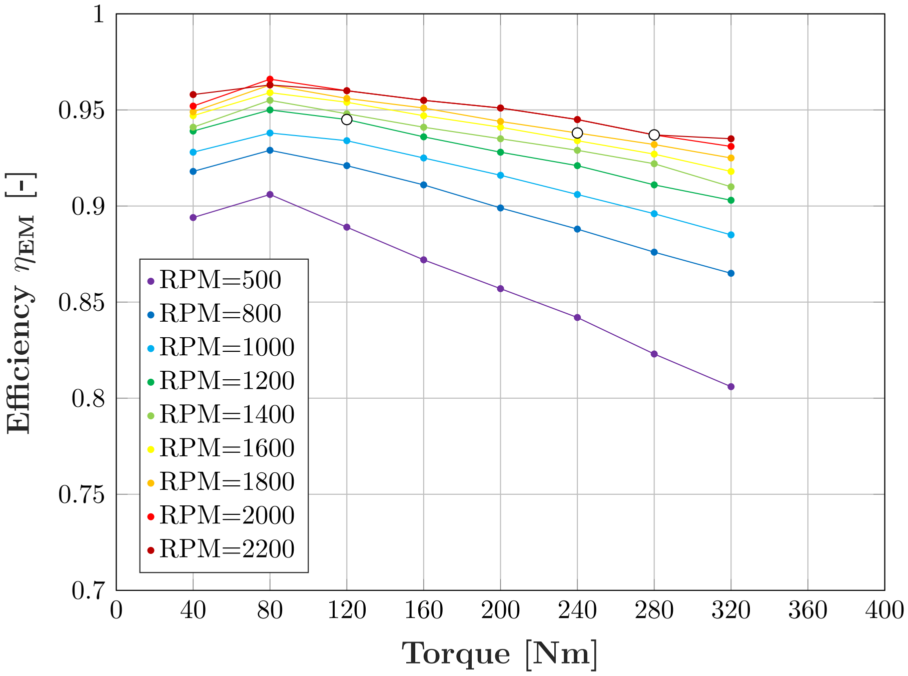

Figure 3.25: Measured efficiency of electric motor "Sineton A0911" with its inverter applied in the electric aircraft e-Genius plotted versus torque and revolution speed

3.5.2 Inverter

All of the investigated motors require an electronic commutation of the electric current via an inverter. Hence, the mass of this motor controller needs to be considered as part of the electric propulsion system. In order to identify the component characteristics, 15 inverters were identified which fulfilled the following criteria: only inverters developed for a mobile application with an environmental protection rating of IP67 or better were included. Further, only inverters with a liquid cooling system and a battery input voltage of at least 450 V were taken into consideration – the corresponding data can be found in table B.8. In Fig. 3.26 the mass of the inverters is plotted versus maximum continuous output power. The trend in equation 3.27 was found significant with a predicted coefficient of determination of $R_{pred} = 0.9177$. The determined trend indicates that the mass of the required inverter elements, such as semiconductor switches, cooling elements, capacitor, housing, electronic circuits and connectors, scales linearly with the maximum continuous power of the inverter. No data is available for inverters with a rated power greater than 205 kW, fulfilling the selection criteria. As a result, the confidence for the results of the trend curve for increased power ratings is reduced, where a extrapolated linear mass growth is assumed.

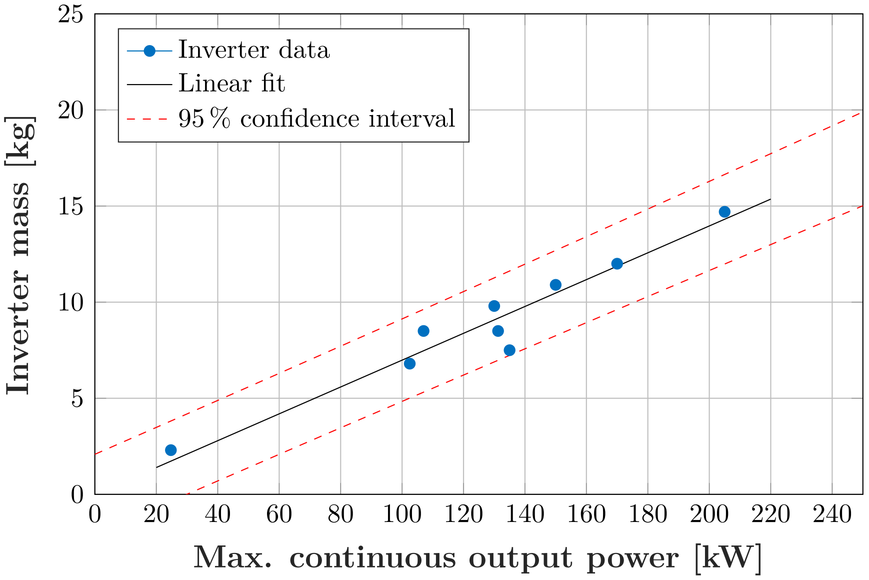

Figure 3.26: Mass plotted versus continuous output power of selected inverters

$$m_{Inv} = \beta_1 \cdot P_{Inv,MCP} \tag{3.27}$$

Symbol	Unit
m_{EM}	$[kg]$
$P_{EM,MCP}$	$[kW]$

Coefficient	Value	Unit	p-value
β_1	0.06966	$^{kg}/_{kW}$	$1.94 \cdot 10^{-9}$

Table 3.13: Units and regression coefficients for the mass trend curve of the investigated inverters with $R^2_{pred} = 0.9177$

According to [66] the maximum achievable efficiency of an inverter depends on the technology of the applied semiconductor devices. Inverters which use silicon based semiconductors achieve an efficiency of 97.1 % whereas inverters which apply silicon carbide based semiconductors achieve an efficiency of 99.1 %. This agrees well with manufacturer data of the silicon based inverter series "DMC5" [67] and the manufacturer data of a silicon carbide based inverter "magniDrive" [68].

3.5.3 Cooling system

The electric motor and the inverter require a cooling system, which increases the overall system mass. All of the investigated electric motors and inverters are designed for the operation with a liquid cooling system. The mass of the additional components is generally not included in the mass of the electric motor – in contrast to the mass of piston engines or gas turbines stated in the type certificate, where the cooling components are included. As no generalized data is available, a more detailed approach is required. In general, a liquid cooling system consists of a radiator, a pump, an equalizing tank, tubing and the cooling fluid where the overall system mass can be calculated with equation 3.28.

$$m_{EM+Inverter,Cooling} = m_{Radiator} + m_{Pump} + m_{Tank} + m_{Tubing} + m_{Coolant} \tag{3.28}$$

In order to estimate the radiator mass, the product of a mean volumetric density and a required radiator volume is assumed to be sufficiently accurate. The mass and the geometrical dimensions of three different radiators, which are made of aluminium and applied in aviation, are used to calculate the mean volumetric density of $\rho_{Radiator} = 0.717\,\mathrm{kg/l}$ (standard deviation $\sigma = 0.022\,\mathrm{kg/l}$) of the radiators.

$$m_{Radiator} = \rho_{Radiator} \cdot V_{Radiator} \tag{3.29}$$

The heat flux $\dot{Q}$, which corresponds in this case to the cooling power $P_{Cooling}$, can be calculated with equation 3.30 [69], by multiplying heat transmission coefficient k, heat exchange area A and temperature difference between cooling fluid and ambiant air ΔT. By dividing equation 3.30 by the matrix volume of the radiator $V_{Radiator}$, equation 3.31 can be derived. According to [53] a radiator which is operated with a 70/30 water/glycol mixture and is cooled by air can achieve a value of $k \cdot A / V_{Radiator} = 3.7 \cdot 10^5\ \mathrm{W/m^3\,K}$. Although [53] describes the preliminary design of a radiator for diesel engines, the parameter ΔT can be adjusted to expected values for electric machines. Consequently, the equation can be applied accordingly to the corresponding radiators. Further, the required cooling power is a function of the power and efficiency of the electric motor and its inverter as expressed in equation 3.32.

$$\dot{Q} = P_{Cooling} = k \cdot A \cdot \Delta T \tag{3.30}$$

$$V_{Radiator} = \frac{P_{Cooling}}{\Delta T \cdot \left(\frac{k \cdot A}{V_{Radiator}} \right)} \tag{3.31}$$

$$P_{Cooling} = (1 - \eta_{EM} \cdot \eta_{Inverter}) \cdot P_{EM} \tag{3.32}$$

By combing equations 3.29, 3.31 and 3.32, equation 3.33 can be derived for the mass of the radiator. With this relation it can be deduced that an increased temperature difference ΔT between cooling fluid and ambient air as well as high efficiencies of electric motor and inverter contribute to a light weight construction as the required radiator mass is decreased.

$$m_{Radiator} = \rho_{Radiator} \cdot \frac{(1-\eta_{EM} \cdot \eta_{Inverter}) \cdot P_{EM}}{\Delta T \cdot \left(\frac{k \cdot A}{V_{Radiator}}\right)} \qquad \text{with} \qquad {}^{k \cdot A}/_{V_{Radiator}} = 3.7 \cdot 10^5 \, {}^{W}/_{m^3 \cdot K} \tag{3.33}$$

According to [53], a mass flow of the cooling fluid through the radiator is required which scales linearly with the radiator volume. In absence of suitable data, it is further assumed that the mass of cooling fluid and the coolant pump scale similarly with the required mass flow. Further, the volume of the equalizing tank grows linearly with the amount of cooling liquid, as it is sized to compensate the expansion of the cooling fluid resulting from temperature changes. Consequently, the mass of the cooling system is estimated as a multiple of the mass of the radiator as shown in equation 3.34. The factor C_{exp} is determined with data summarized in table B.9 gained in the project e-Genius of the University of Stuttgart for a close installation of the cooling system to the electric motor Sineton A0911 and its inverter. The parameter C_{exp} in equation 3.34 represents only a coarse guide value and depends strongly on the final design and installation of the cooling system.

$$m_{EM+Inverter,Cooling} = C_{exp} \cdot m_{Radiator} \qquad \text{with } C_{exp} \sim 5 \tag{3.34}$$

3.6 Electric power distribution

In a hybrid-electric aircraft the electric power needs to be transferred in between electric machines, converters and battery systems. The necessary system consists of cables, connectors and power relays with corresponding housing. According to [70], the electric current I_N, a cable can transfer under standard conditions, depends on the cross-sectional area of the electrical conductor. However, this current does not scale linearly with the cross sectional area as shown in Fig. 3.27. Furthermore, in order to derive the current I a cable can carry under specific operating conditions, reduction factors have to be applied which take into account the effect of an increased ambient temperature f_1, a certain permissible conductor temperature f_2, the type of physical installation f_3 and the influence of an increased frequency of an alternate current f_4 accounting for the skin effect [71], which causes the effective resistance of a cable to rise with increasing frequency. It is assumed in the further consideration that through an appropriate wiring design the reduction factors $f_i = 1$ can be achieved.

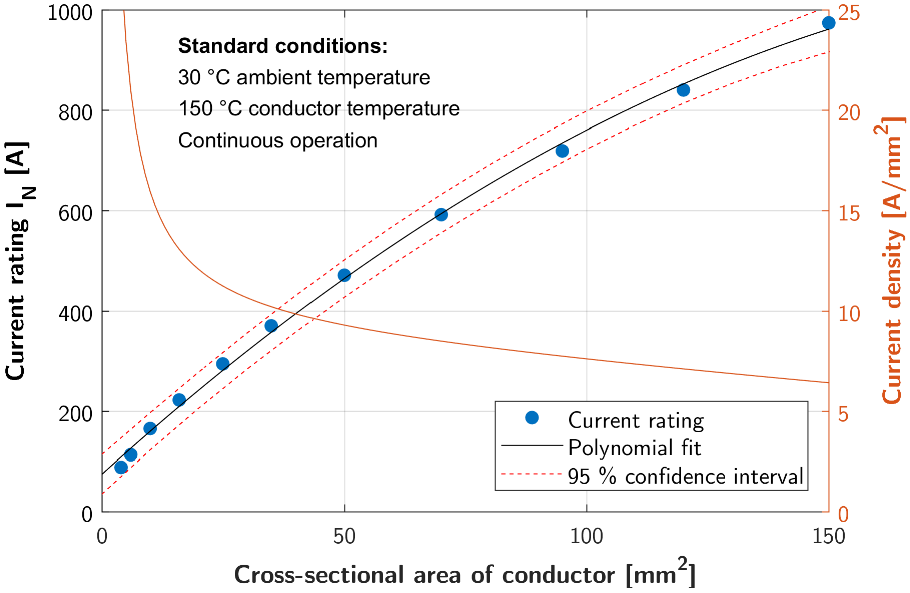

Figure 3.27: Current rating versus cross-sectional area of "Radox 155" cables made from copper [70] with an insulation rated for a maximum voltage of 1500 V direct current / 1000 V alternate current for an installation with unrestricted heat dissipation in air

$$I = I_N \cdot f_1 \cdot f_2 \cdot f_3 \cdot f_4 \tag{3.35}$$

To justify the trend of the decreasing current density in Fig. 3.27, several effects have to be considered. The circumference of a circular cross section has a significant beneficial influence on the heat dissipation in a two dimensional analysis [69]. However, by geometric considerations it can be deduced that conductors with a higher diameter possess a decreased ratio of circumference to cross-sectional area. Consequently, if a constant current density is applied and the cable diameter is increased, the heat generation due to ohmic losses increases more than the heat dissipation does and the conductor temperature rises as a consequence. In contrast, the data given in Fig. 3.27 applies a maximum permissible conductor temperature of 150 °C in order to achieve the same lifetime of the different cables [70] and, as a result, the permissible current density decreases as the conductor diameter is increased. The resistance of a conductor with an increased diameter transferring alternating current is increased even further due to the skin effect [71].

The electric power which a cable cross section can transfer is calculated by multiplying the current I by the voltage U. In Fig. 3.28 the length specific mass of screened power cables [70] is plotted versus the electric power which result from different oper-

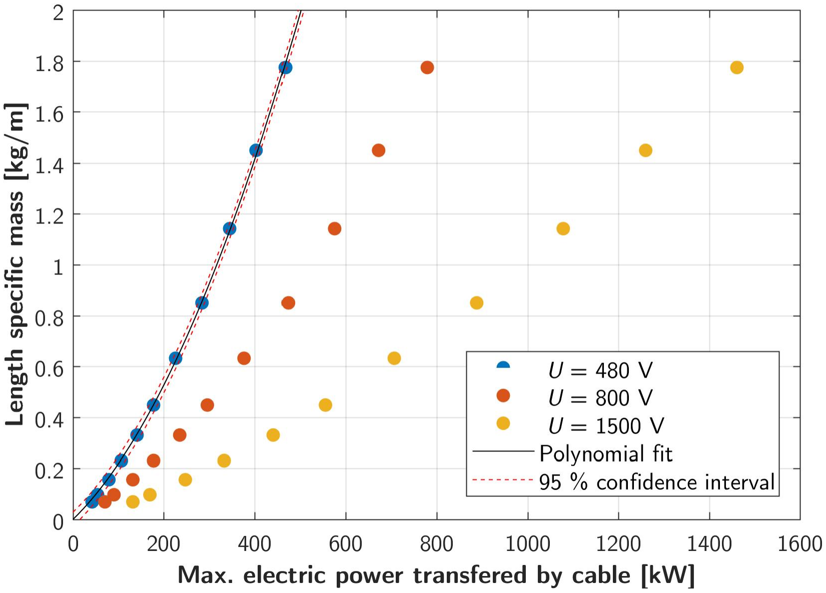

Figure 3.28: Length specific mass plotted versus electric power for different operating voltages

ating voltages. It can be observed that the lowest cable mass is required if the cable is operated with its maximum voltage rating of $U_{Cable,max} = 1,500\,\mathrm{V}$. However, the maximum voltage for the investigated converters in section 3.5.2 is limited to $U = 800\,\mathrm{V}$ – further, the cable cross section needs to be sized to the lowest voltage. In a battery system consisting of lithium-ion battery cells the maximum system voltage of $U_{Bat,max} = 800\,\mathrm{V}$ corresponds typically to the highest cell voltage of $U_{Cell,max} = 4.2\,\mathrm{V}$ [1] whereas the lowest cell voltage of $U_{Cell,min} = 2.5\,\mathrm{V}$ leads to a battery system voltage of $U_{min} \sim 480\,\mathrm{V}$. Consequently, the cable mass corresponding to this voltage is considered for the sizing of the hybrid-electric propulsion system. The polynomial trend curve in equation 3.36 for the length specific cable mass $m_{s,Cable}$ can be derived.

$$m_{s,Cable} = \beta_1 \cdot P_{max} + \beta_2 \cdot P_{max}^2 \tag{3.36}$$

Symbol	Unit
$m_{s,Cable}$	$^{kg}/_{m}$
P_{max}	$[kW]$

Coefficient	Value	Unit	p-value
β_1	0.001646	$^{kg}/_{m\cdot kW}$	$0.18 \cdot 10^{-9}$
β_2	$4.831 \cdot 10^{-6}$	$^{kg}/_{m\cdot kW}$	$0.22 \cdot 10^{-9}$

Table 3.14: Units and regression coefficients for the trend curve of the mass of electric power cables with $R^2_{pred} = 0.9988$

	EV200	**GV350**
Manufacturer	TE Connectivity Ltd.	Sensata Tech., Inc.
Max. DC voltage	900 V	1,000 V
Max. current	500 A	500 A
Mass	0.43 kg	0.39 kg
Max. resistance	0.2 mOhms	0.2 mOhms
Source	[73]	[74]

Table 3.15: Data of high voltage relays

In Fig. 3.27 it can be observed that less current per cross section area can be transferred as the cable area increases. As a result, the cable mass grows disproportionately high with the electric power. In order to reduce this mass growth, it will be assumed in the sizing process that increased electric power can be transferred by multiple cables with a cross section of $150\,\mathrm{mm}^2$.

In [70] the ohmic resistance at a conductor temperature of $20\,^\circ\mathrm{C}$ is given for the specific cross sections. The ohmic resistance is then corrected [72] to the highest permissible conductor temperature of $150\,^\circ\mathrm{C}$. With this data the power loss due to ohmic resistance is calculated at highest rated current I_N and is expressed as a fraction of the corresponding power. In Fig. A.5 this power loss per length of cable is plotted for a mean voltage $U_{Bat,mean} = 640\,\mathrm{V}$. In an exemplary design case, a cable has a length of $2 \cdot 10 = 20\,\mathrm{m}$ and is sized for the maximum power $P_{max} = 300\,\mathrm{kW}$. When this maximum power is applied to the cable, a loss of approx. $0.08\,\%$ is the result, leading to an efficiency of $99.2\,\%$. If only half of its maximum power $P = 150\,\mathrm{kW}$ is applied, the losses lower to $0.02\,\%$ leading to an efficiency of $99.8\,\%$.

In order to disconnect a battery pack after a failure from the electric system, a relay on the positive pole of each battery pack is required. Furthermore, at least one relay in the negative pole of the battery system is necessary in order to be able to disconnect the converters from the electric potential. In table 3.15 the data of two suitable hermetic relays is summarized. Additional mass is required for the housing of the relays and integration elements such as cable lugs, bolts, etc. In the electric aircraft e-Genius this additional mass is in the order of magnitude of the mass of the relays. The investigated relays possess an efficiency of $99.9999\,\%$, taken the maximum stated ohmic resistance, voltage and current as the basis of the calculation.

In order to facilitate a disassembly of the electric components of the propulsion system, cable connectors are applied. The ohmic resistance of the investigated automotive high voltage connectors [75] leads to a mean efficiency of $99.9989\,\%$ (standard deviation $\sigma = 0.0067\,\%$) at the corresponding highest rated electric power transferred by the connector. At this preliminary design stage, these losses are neglected.

3.7 Propellers

The last component in the serial hybrid propulsion chain is the propeller, which converts mechanical shaft power into propulsive power. In contrast to combustion engines, which are rated to output power, propellers are rated to input power. The data of the propellers in table B.10, which are designed for the application in CS-23 airplanes, was investigated. The data set was reduced to propeller blades made from composite, as propellers made out of aluminium are more heavy according to [76] and [77] while achieving similar performance. Further, only variable pitch propellers were considered, where the blade angle can be adjusted in flight in order to achieve the advance ratio necessary to operate the propeller blade at its best efficiency [4]. In Fig. 3.29 the mass specific power is plotted versus the power of the investigated propellers. It can be observed that the specific power increases as the power rating of the propeller is increased. A linear trend curve, shown in equation 3.37, was found suitable to describe the rising mass specific power of the propellers as the input power increases.

$$\left({}^{m_{Prop}}\!/_{P_{sh,max}}\right) = \beta_0 + \beta_1 \cdot P_{sh,max} \tag{3.37}$$

Symbol	Unit
m_{Prop}	$[kg]$
$P_{sh,max}$	$[kW]$

Coefficient	Value	Unit	p-value
β_0	6.991	kg/kW	$0.0002 \cdot 10^{-9}$
β_1	0.01036	kg/kW^2	$0.1983 \cdot 10^{-9}$

Table 3.16: Units and regression coefficients for the trend curve of propeller mass with $R^2_{pred} = 0.8040$

The aspects of the trend found in Fig. 3.29 are discussed subsequently. According to the disk actuator theory [78], the power of a propeller is proportional to the propeller disk area – hence, power scales with the square of the diameter of the propeller blades. Contrarily, an empirical relationship published by [4] relates the power of a propeller to the diameter of its blades to the power of four, which agrees with equations found by [79]. Furthermore, the power depends on the number of blades – however, the influence of the number of blades is lower than the influence of the propeller diameter[6].

---

[6] According to [4], the power of a 4-blade propeller is ~70 % increased compared to a 2-blade propeller with the same diameter

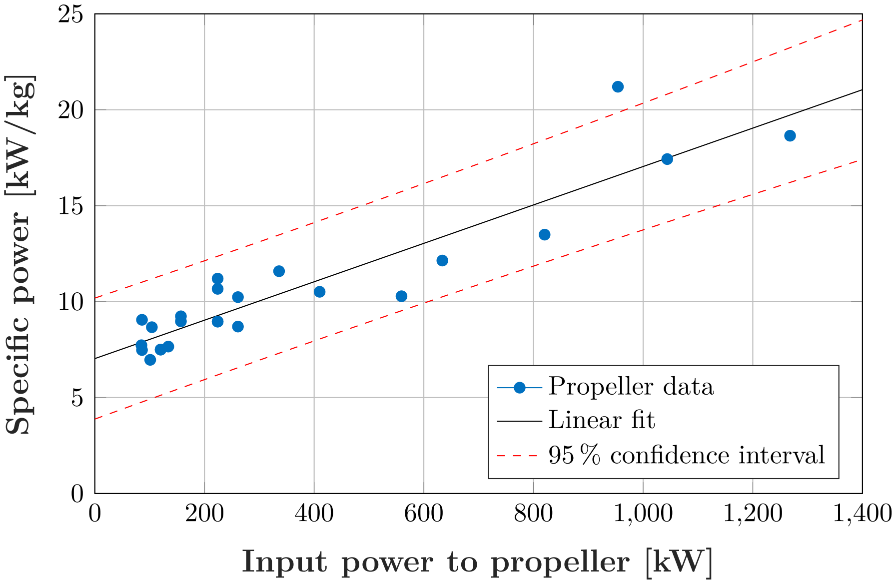

Figure 3.29: Mass specific power plotted versus rated input power of the investigated propellers

The mass of a propeller consists mainly of the load bearing structure, which sustains aerodynamic forces and the resulting bending moments as well as centrifugal forces due to the rotation. Typically, the produced thrust as well as the bending length increases with increasing propeller diameter, resulting in a higher bending moment and requiring more structural mass. However, as the diameter of the propeller blades increases, generally the chord length of the propeller air foil grows. As a consequence, the thickness of the blades increases, assuming the same air foil is applied. The maximum thickness of the blade defines then the height available for the spar structure, which bears the bending moment. According to [80], the area moment of inertia of a rectangular cross section grows with the height to the power of three [80]. Under the assumption that the same bending stress shall be present, less structural mass per bending moment is required when the thickness of the blade increases.

The centrifugal force requires further structural mass and grows proportionally with the radius and the mass of the propeller but is reduced by lower rotational velocities. Accordingly, the force grows by an increased propeller diameter and propeller mass but is reduced by a lower maximum rotational velocity, which is required for large propellers in order to avoid shocks waves at the propeller tips [4]. The trend found in Fig. 3.29 suggests that aspects which increase the specific power outweigh the aspects which decrease the specific power of the propellers as the rated power is increased.

Chapter 4

Sizing correlations of hybrid-electric aircraft

4.1 Interactions between propulsion system and aircraft design

4.1.1 Influence of the propulsion system mass on aircraft mass

The required shaft power P_{sh} for a horizontal flight is given in equation 4.1. It can be observed that P_{sh} is influenced by glide ratio $^{L}/_{D}$, propeller efficiency η_P, efficiency of the propeller integration η_I and the speed v. The shaft power is also a linear function of the momentary aircraft mass $m_{A/C}$. Therefore, an adequate prediction of the aircraft mass is necessary in order to determine the required energy for a flight mission of an hybrid-electric aircraft.

$$P_{sh} = \frac{m_{A/C} \cdot g \cdot v}{^{L}/_{D} \cdot \eta_P \cdot \eta_I} \tag{4.1}$$

$$m_{MTO} = m_{Empty} + m_{Crew} + m_{Payload} + m_{Fuel} \tag{4.2}$$

In preliminary aircraft design the mass break down in equation 4.2 is used for a first estimation of the maximum take-off weight [4], where the mass of the payload $m_{Payload}$ includes the mass of the passengers. A common approach [4] [62] is to apply a constant empty weight fraction depending on the type of airplane and the maximum take-off mass itself. In addition, the fuel fraction can be regarded as constant and can be determined for a specific flight mission by the Breguet range equation and statistical data.

$$m_{MTO} = \frac{m_{Crew} + m_{Payload}}{1 - \left(\frac{m_{Fuel}}{m_{MTO}}\right) - \left(\frac{m_{Empty}}{m_{MTO}}\right)} \tag{4.3}$$

The impact of the payload mass on the maximum take-off mass is determined by equation 4.3. The empty mass fraction $\left(\frac{m_{Empty}}{m_{MTO}}\right)$ takes into account that the structural weight of the fuselage with its subsystems increases in order to carry the additional payload. Furthermore, it factors in that e.g. the wing, empennage and engine group will have an increased weight in order to achieve a similar flight performance during take-off, climb and landing.

Equation 4.3 is, however, not suitable to asses the increase in maximum take-off mass associated with a purely increased propulsion system mass. In a first approach, the equation could be modified in a way that the mass of the propulsion system is not regarded as a part of the empty weight fraction and is moved to the numerator of the equation as described in [81]. Consequently, the empty weight fraction has to be reduced as it does not incorporate anymore the mass of the propulsion system. However, this equation would assume that an increase in payload mass, which are passengers in this case, has the same effect as an increase in the propulsion system mass, neglecting that e.g. the mass of furnishings, air conditioning, windows, doors will not be increased if the mass of the propulsion system is increased. In order to asses more precisely the structural mass growth related to the increased mass of the hybrid-electric propulsion system, the effect onto each component mass of the aircraft has to be determined.

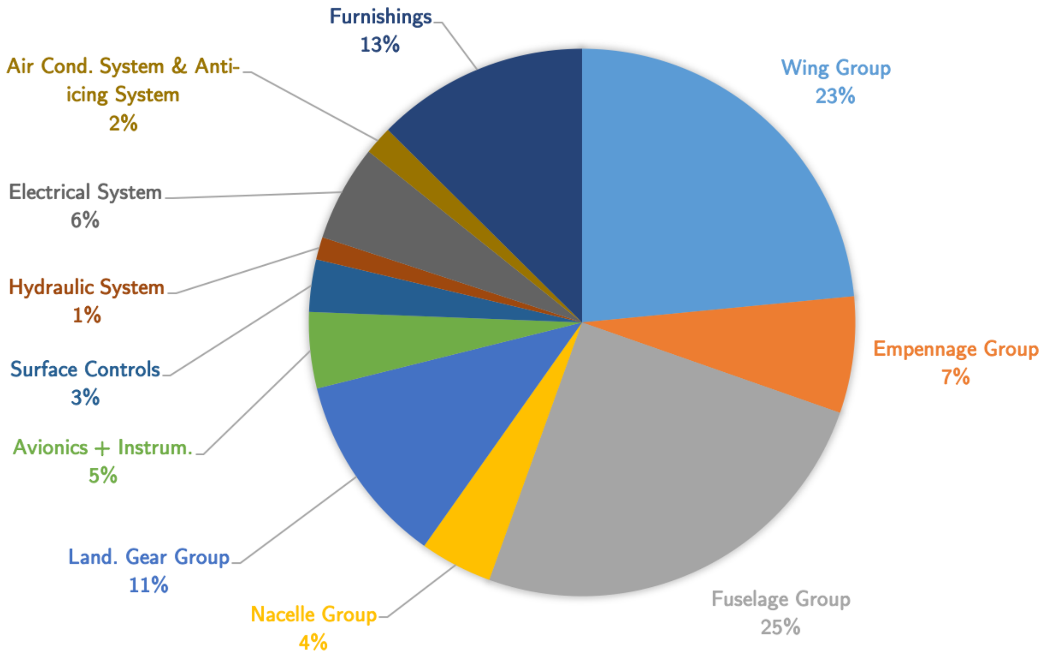

Figure 4.1: Component mass break down of a Rockwell Commander 112 TCA excluding its propulsion system

In Fig. 4.1 a mass break down of the aircraft "Rockwell Commander 112 TCA" is given with data from [46]. The chart shows the percentage each individual aircraft component contributes to the aircraft's empty mass, excluding its propulsion system. The Rockwell Commander 112 TCA is an airplane with the characteristics of a modern four-seat aircraft as it possesses a low, cantilever wing and a retractable landing gear. Further, it has a certification according to FAR23 and a maximum take-off mass of 1340 kg. In aircraft design literature [46] and [4], empiric equations are given for the estimation of component mass and the aircraft components which are affected by a change in the aircraft design parameters can be identified. In the present case, these aircraft design parameters are: maximum take of mass m_{MTO}, wing reference area S_w, aspect ratio Λ, fuel mass m_{Fuel} and the areas of the vertical and horizontal stabilizer S_{VTP} and S_{HTP}. In the following example, the mass of the wing is investigated. By dividing the empiric formula for the wing mass m_{Wing} given in [4] by the same empiric formula with parameters for a known reference aircraft $m_{Wing,0}$, equation 4.4 can be deduced assuming that the remaining parameters[1] are equal for both aircraft. If the parameters $m_{Wing,0}$, $S_{w,0}$, A_0 and $m_{MTO,0}$ are known for the reference aircraft, an estimation of the wing mass for the given aircraft parameters S_w, A and m_{MTO} can be calculated. By using the data of an existing, structurally comparable aircraft, the precision of the mass estimation is increased. The mass growth factors C_m, which are derived as shown in equation 4.5 from the component mass formulas in [4], are summarized in table 4.1.

$$\frac{m_{Wing}}{m_{Wing,0}} = \frac{{S_w}^{0.758} \cdot \Lambda^{0.6} \cdot {m_{MTO}}^{0.49}}{{S_{w,0}}^{0.758} \cdot {\Lambda_0}^{0.6} \cdot {m_{MTO,0}}^{0.49}} \tag{4.4}$$

$$m_{Wing} = \underbrace{\left({}^{S_w}\!/_{S_{w,0}}\right)^{0.758} \cdot \left({}^{A}\!/_{A_0}\right)^{0.6} \cdot \left({}^{m_{MTO}}\!/_{m_{MTO,0}}\right)^{0.49}}_{C_{m,Wing}} \cdot m_{Wing,0} \tag{4.5}$$

The mass of the hybrid-electric propulsion system can be calculated by considering the mass of each component of the propulsion system as listed in table 4.2. As described in chapter 3 the required mass for mounting frames, cooling systems, etc. is included in this mass. As the equations involved in the calculation of propulsion system mass are non-linear, the maximum take-off mass is determined with an iterative calculation.

$$m_{Propulsion} = m_{ICE} + m_{Bat} + m_{EM} + m_{Gen} + m_{PD} + m_{Prop} \tag{4.6}$$

---

[1] In this particular case the remaining parameters are: taper ratio, ultimate load factor, sweep, dynamic pressure at cruise and relative thickness of airfoil.

Mass group	**Factor for mass growth C_m**
Wing group	$\left(S_w/S_{w,0}\right)^{0.758} \cdot \left(\Lambda/\Lambda_0\right)^{0.6} \cdot \left(m_{MTO}/m_{MTO,0}\right)^{0.49}$
Horizontal tailplane group	$\left(m_{MTO}/m_{MTO,0}\right)^{0.414} \cdot \left(S_{HTP}/S_{HTP,0}\right)^{0.896}$
Vertical tailplane group	$\left(m_{MTO}/m_{MTO,0}\right)^{0.376} \cdot \left(S_{VTP}/S_{VTP,0}\right)^{0.873}$
Fuselage group	$\left(m_{MTO}/m_{MTO,0}\right)^{0.177}$
Nose landing gear group	$\left(m_{MTO}/m_{MTO,0}\right)^{0.566}$
Main landing gear group	$\left(m_{MTO}/m_{MTO,0}\right)^{0.768}$
Fuel system	$\left(m_{Fuel}/m_{Fuel,0}\right)^{0.726}$
Avionics + instruments	no mass growth
Surface controls	$m_{MTO}/m_{MTO,0})^{0.8}$
Hydraulic system	no mass growth
Electrical system	$\left(m_{Fuelsystem} + m_{Avionics}\right)^{0.51}$
Air cond. system, anti-icing system	no mass growth
Furnishings	no mass growth

Table 4.1: Mass growth factors derived from [4]

Component	**Source for mass estimation**
Internal combustion engine m_{ICE}	section 3.3 and 3.2
Battery system m_{Bat}	section 3.4
Electric motor m_{EM} and generator m_{Gen}	section 3.5
Power distribution m_{PD}	section 3.6
Propeller m_{Prop}	section 3.7

Table 4.2: Component masses of the hybrid-electric propulsion system

4.1.2 Influence of the aircraft mass onto the parasitic and induced drag

As the application of an hybrid-electric propulsion is likely to change the aircraft mass, the interaction of aircraft mass and aerodynamic drag is investigated in the following section. In preliminary aircraft design, the aerodynamic drag D is divided into two components: the parasitic drag D_0 and the drag due to lift D_i.

$$D = D_0 + D_i \tag{4.7}$$

A major driver for the parasitic drag D_0 is the area of the aircraft exposed to the airflow, the so-called "wetted area", which is influenced by the aircraft mass. The design of the hybrid-electric aircraft will be carried out maintaining the same wing

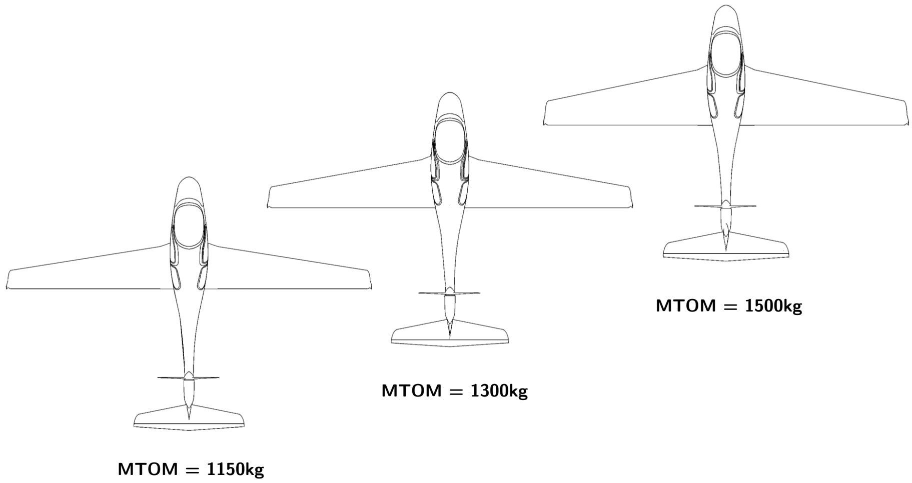

Figure 4.2: Influence of the maximum take-off mass onto the wing area and size of the stabilizers, maintaining a constant wing span and taper ratio

loading of the conventional propelled reference aircraft in order to obtain same stall speeds. Accordingly, the same wing span as the reference aircraft is applied to the hybrid-electric aircraft. As a result, the magnitude of the drag is not influenced by an increased wing span and the effect of the hybridization of the propulsion system is isolated. A further consequence of the same wing span is that the ground handling and hangaring requirements are comparable and corresponding costumer expectations are met.

As a constant wing loading is applied in the design of the aircraft to achieve similar stall speeds, the wing area grows as the take-off mass increases. Due to the increased wing size, more force is necessary to stabilize and control the aircraft and the size of vertical and horizontal stabilizers grow accordingly. The influence on the stabilizers can be determined by the application of tail volume coefficients as defined in [4]. In order to obtain similar manoeuvrability and similar longitudinal and lateral stability as the reference aircraft, the same tail volume coefficients are applied to the hybrid-electric aircraft. As a result, the wetted area of wing and stabilizers grows which leads to increased parasitic drag. The influence of take-off mass onto the size of the wing and the empennage of an aircraft is shown in Fig. 4.2.

The increased parasitic drag is calculated by a component build-up method in equation 4.8, which is valid for subsonic aircraft speeds. The method calculates the drag for each component with its corresponding flat-plate skin friction coefficient C_{fc}, component form factor FF_c, component interference factor Q_c and wetted surface of the component $S_{wet,c}$. With the determination of the skin friction coefficient C_{fc} based on the Reynolds number of the component, the influence of natural laminar flow over a certain percentage of the component can be incorporated [5]. Values for Q_c and FF_c are taken from statistical data found in [4].

$$D_0 = \sum \left(C_{fe} \cdot FF_c \cdot Q_c \cdot S_{wet,c} \right) \cdot q + \left(c_{D,misc} + c_{D,LP} \right) \cdot S_w \cdot q \tag{4.8}$$

Additionally to the parasitic drag, the induced drag increases as well as aircraft mass grows. The formula for the drag due to lift D_i in stationary horizontal flight is given in equation 4.9. The influence of an increased aircraft mass $m_{A/C}$ onto the magnitude of the drag due to lift is shown directly in this equation. The Oswald-factor e can be determined by equation 4.10, where the parameters of the air foil and the wing planform can be found. As the aspect ratio of the wing is reduced, the Oswald factor increases slightly according to equation 4.10. According to [82], the term δ reflects the drag increase due to a non-elliptic lift distribution. $\delta = 0$ indicates an elliptic lift distribution which results in the lowest possible magnitude of wing tip vortices for a specific aspect ratio Λ and aircraft mass. The factor k_p incorporates the lift-dependent drag of the two-dimensional airfoil and is regarded as constant. In Fig. 4.3 the influence of the aircraft mass on the drag is summarized.

$$D_i = \frac{\left(m_{A/C} \cdot g \right)^2}{q \cdot \pi \cdot b^2 \cdot e} \tag{4.9}$$

$$e = \frac{1}{1 + \delta + k_p \cdot \pi \cdot \Lambda} \tag{4.10}$$

4.1.3 Calibration of drag calculation

In order to improve the precision of the drag estimation, the calculation is carried out for the existing, unconventional aircraft e-Genius. The resulting drag polar is compared to the actual drag polar obtained in a flight test campaign with the existing aircraft. By the comparison of the drag polars, a calibration factor for the drag estimation method is obtained, which is used to improve the results of the applied method. Differently to the previous section, the drag components D_0 and D_i are expressed as drag coefficients c_{D0} and c_{Di}. Furthermore, the Oswald factor e and the aspect ratio Λ is translated to the "drag due to lift factor" k [4], which is shown in equation 4.11.

In Fig. 4.4 the drag polar of e-Genius, which was obtained in 2013 in a flight test campaign, is shown. According to [4], a quadratic shape of the drag polar, as shown in equation 4.11, can be assumed in preliminary airplane design. The corresponding fit, along with its prediction bounds, is plotted in Fig. 4.4. It can be observed that

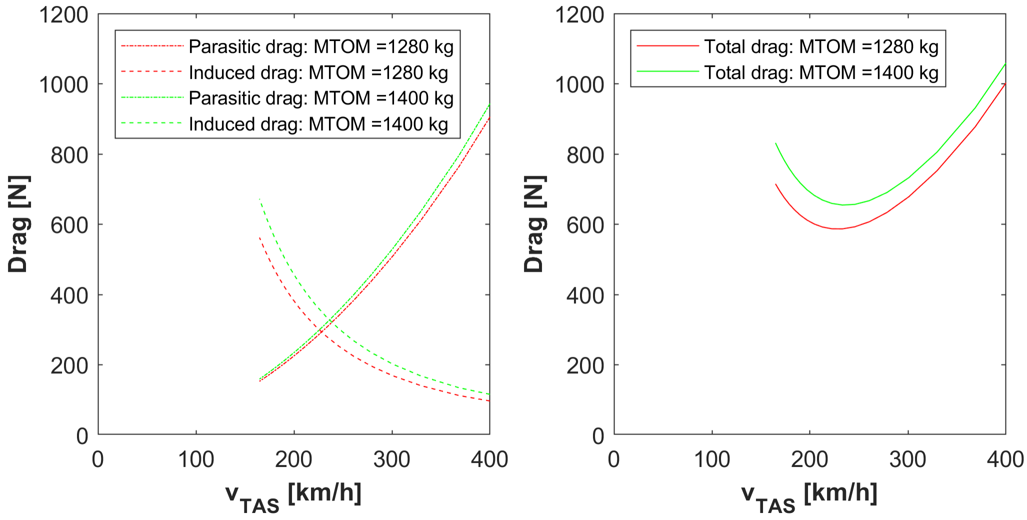

Figure 4.3: Induced and parasitic drag for different aircraft masses (left) and total drag (right)

the fit corresponds well in the range of lift coefficients between $0.4 < c_L < 1.0$ with $R^2_{pred} = 0.998$.

$$c_D = c_{D0} + \frac{{c_L}^2}{\pi \cdot \Lambda \cdot e} = c_{D0} + k \cdot {c_L}^2 \tag{4.11}$$

Symbol	Unit
c_D	[-]
c_L	[-]

Coefficient	Value	p-value
c_{D0}	0.01038	0.0000
k	0.02359	0.0000

Table 4.3: Units and regression coefficients for the trend curve of drag polar fit of the aircraft e-Genius with $R^2_{pred} = 0.998$

The parasitic drag is calculated as described in section 4.1.2. Equation 4.12 for the calculation of the parasitic drag coefficient c_{D0} is a variation of equation 4.8. The applied parameters for the calculation are summarized in table 4.4. With this data the parasitic drag coefficient can be determined to be $c_{DO} = 0.01028$. Additional drag due to leakage and protuberance as well as further miscellaneous drag was not considered at this stage. It can be observed that the estimated parasitic drag coefficient matches well the coefficient obtained in flight test and shows a difference of merely 1 %.

$$c_{D0} = \sum \frac{(C_{fe} \cdot FF_c \cdot Q_c \cdot S_{wet,c})}{S_w} + c_{D,misc} + c_{D,LP} \tag{4.12}$$

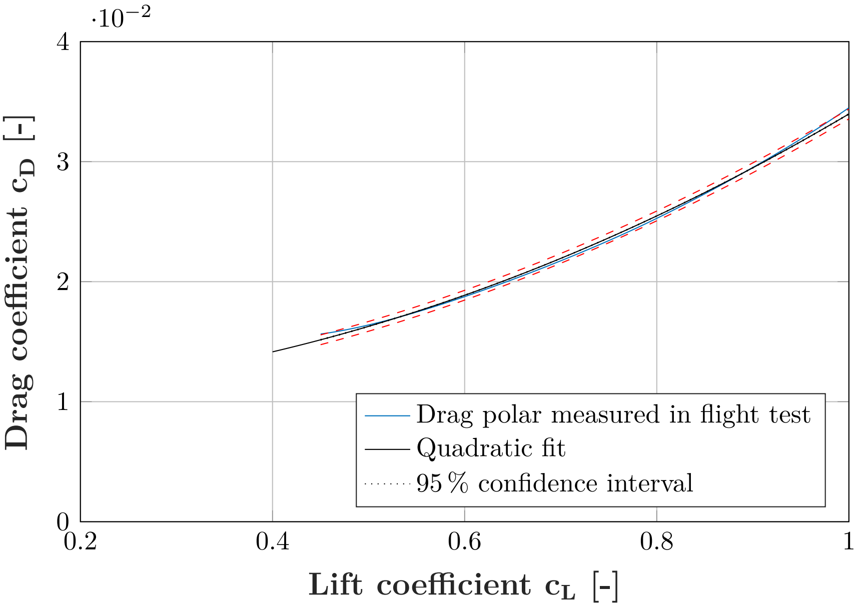

Figure 4.4: Quadratic fit of the drag polar of the aircraft e-Genius measured in flight tests

Component	**Wetted area** $[m^2]$	C_{fe}	**Form factor** FF	Q_c	$c_{D0,c}$
Wing	28.8	0.00215	1.37	1.0	0.00583
Fuselage	15.9	0.00213	1.17	1.0	0.00268
Vertical stabilizer	4.0	0.00223	1.33	1.05	0.00085
Horizontal stabilizer	3.9	0.00247	1.33	1.05	0.00091

Table 4.4: Parameters of parasitic drag estimation of e-Genius according to [4]

The factor k which determines the magnitude of the induced drag is estimated according to [82] with equation 4.13. k_p was determined from the air foil data of the wing of e-Genius. δ is estimated by the aspect ratio and the taper ratio of the wing and was determined to be $\delta = 0.03$ for the wing of the e-Genius with an aspect ratio of $\Lambda = 19$. With the data, the factor $k = 0.02436$ can be calculated, which matches the factor k obtained from flight test with a difference of 3.2 %.

$$k = k_p + \frac{1+\delta}{\pi \cdot \Lambda} \tag{4.13}$$

The calibrated method of sub-sonic drag estimation, described above, will be used in the sizing of hybrid-electric propulsion systems to evaluate the drag of non-existing, unconventional aircraft with the propeller installed in the vertical stabilizer similar to e-Genius. The propeller efficiency η_P and propeller installation efficiency η_I of these aircraft were assumed to be similar to the e-Genius. With data obtained in flight tests the product of η_P and η_{Int} was determined to be $\eta_P \cdot \eta_I = 0.82$ according to [21]. The flight test campaign showed as well that this parameter can be regarded as constant for different cruise speeds [21].

4.1.4 Evaluation of a propeller integration in the vertical stabilizer

In order to evaluate the effect of the integration of an electric motor in the tail, equation 4.1 of the required shaft power P_{sh} for horizontal flight is used. The glide ratio $\frac{L}{D}$, the propeller efficiency η_P and the integration efficiency η_I are part of the formula and can be found as a product in the denominator.

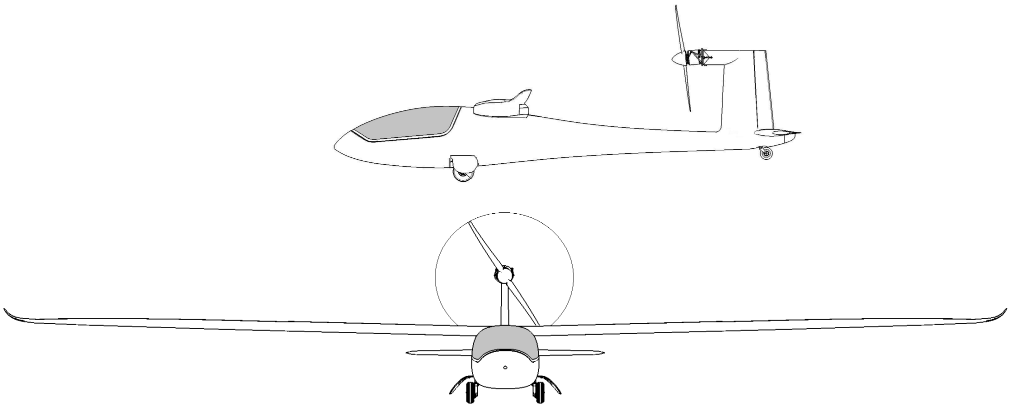

Figure 4.5: Electric aircraft e-Genius with propeller integration in the vertical tail

The term $\frac{L}{D} \cdot \eta_P \cdot \eta_I$ is used as a figure of merit. It is calculated for different conventional aircraft types and compared to the optimized electric aircraft e-Genius. The e-Genius was chosen as its drag calculation is available and validated in a flight test campaign. With this validated drag calculation the influence of different wing areas and wing spans onto the cruise performance can be taken into account.

To isolate the effect of the electric motor in the tail and to compare it to the conventional engine installation in the aircraft nose, all remaining aerodynamic effects had to be equalized. Therefore, the wing area of the e-Genius was altered to the wing area of the respective conventional aircraft in order to achieve the same parasitic drag of the wing. Furthermore, the wing loading of the e-Genius was equalized so that both aircraft would fly with the same lift coefficient. Finally, the wing span was matched, which resulted in the same induced drag. The term $\frac{L}{D} \cdot \eta_P \cdot \eta_I$ of the different reference aircraft was calculated using equation 4.14. The required power, the cruise speed and the mass were taken from the corresponding flight manuals. If a fuel flow was stated in the flight manual, the value was converted into engine power with the specific fuel consumption given by the data sheet of the engine manufacturer [83].

$$\frac{L}{D} \cdot \eta_P \cdot \eta_I = \frac{m_{A/C} \cdot g \cdot v}{P_{sh}} \tag{4.14}$$

The first comparison is made to a "Valentin Taifun 17E II". The Taifun is a two-seated aircraft with similar cruise speed, similar composite material technology and the same certification basis as the e-Genius. It is the most modern aircraft in the class "touring motor glider" and features a retractable landing gear. In the first line of table 4.5 the data from the aircraft according to the flight manual [84] is shown. In second line of table 4.5 the data of the scaled e-Genius is listed. The wing span, wing area and wing loading of the Taifun are similar to the parameters of the original e-Genius. Therefore, the performance figures of the scaled electric aircraft do not differ significantly from the original e-Genius. Comparing table 2.2 and table 4.5 it can be seen that although the wing span of the modified e-Genius has slightly increased compared to the original version, the product $\frac{L}{D} \cdot \eta_P \cdot \eta_I$ has decreased due to higher wetted area of the wing.

	Required power P_{sh}	**Cruise speed** v	**Mass** m_{MTO}	**Product** $\frac{L}{D} \cdot \eta_P \cdot \eta_I$
Valentin Taifun 17E II	33.1 kW	172 km/h	850 kg	12.0
e-Genius mod. 1	17.3 kW	172 km/h	850 kg	23.0

Table 4.5: Valentin Taifun 17E II compared to e-Genius with same wing span (17 m), wing area (17.6 m^2) and wing loading (48.3 $\mathrm{kg/m}^2$)

As a second reference aircraft a "Shark Aero UL" [85] is compared to a modified e-Genius. The Shark is a high performance microlight aircraft, which was made for fast and efficient cruise flight. It has a tandem seat cockpit and a retractable main and nose gear. Wing span, wing area and wing loading of the e-Genius were scaled down to the parameters of the Shark.

	Required power P_{sh}	**Cruise speed** v	**Mass** m_{MTO}	**Product** $\frac{L}{D} \cdot \eta_P \cdot \eta_I$
Shark Aero UL	42.1 kW	200 km/h	472.5 kg	7.8
e-Genius mod. 2	18.9 kW	200 km/h	472.5 kg	13.6

Table 4.6: Shark Aero UL compared to e-Genius with same wing span (7.9 m), wing area (9.5 m^2) and wing loading (49.7 $\mathrm{kg/m}^2$)

As table 4.5 and table 4.6 show, the optimized single engine electric aircraft achieves roughly a 74 % to 92 % increased value for the product $\frac{L}{D} \cdot \eta_P \cdot \eta_I$ compared to the most modern conventional aircraft with a front mounted engine. This effect is a strong benefit for optimized electric aircraft as the required shaft power for cruise flight is reduced considerably. In this consideration more reference aircraft were examined and compared to the optimized electric aircraft. Investigated were an Ellipse LH 10, a Pipistrel Virus and a Dynamic WT9 RG. All comparisons showed similar results. This strong beneficial effect for electric single motor aircraft has to be investigated for multi engine aircraft configurations.

On one hand, the equation for the required shaft power in equation 4.1 shows the beneficial effect of higher glide ratios and better propeller and integration efficiencies. On the other hand, it shows the influence of the aircraft mass – an increased mass leads to an increased power requirement. Electric aircraft tend to be heavier than conventional aircraft, but the influence of the increased glide ratio and the better propeller and integration efficiency will strongly dominate in single engine aircraft configurations. As a consequence, these electric aircraft will need less shaft power for cruise flight and will hence consume less energy.

4.2 Required fuel and battery mass for series hybrid-electric aircraft

The investigated aircraft transport mission, which is shown in Fig. 4.6, consists of a take-off and initial climb ①, a climb phase ②, a cruise flight ③ and a descent phase ④. Additionally, the mission includes a missed approach at the destination airport ⑤ and a climb ⑥, cruise, loiter ⑦ and descent ⑧ to the alternative airport. In preliminary design of conventional aircraft, mass fractions for the individual mission segments are determined, either by historical data or by the Breguet range equation. Consequently, the fuel fraction ξ_{Fuel} of the entire mission can be calculated. An advantage of this approach is that no knowledge of the maximum take-off mass is required for the calculations. This approach is valid as all energy usage of conventional aircraft is associated with a reduction in aircraft mass, as fuel is burnt. This approach is, however, not suitable for the design of a hybrid-electric aircraft, because of the presence of a battery system, where a usage of battery energy is not related to a reduction in aircraft mass, as the discharged battery system stays on-board the aircraft. As a result, the required fuel and battery energy need to be calculated explicitly in each flight segment for the hybrid-electric aircraft, which requires the knowledge of the maximum take-off mass, leading to an iterative calculation process. This, however, can be compensated by the application of programming tools. Because mass fractions enable a direct evaluation of the mass distribution in aircraft design, the required fuel fraction ξ_{Fuel} and battery fraction ξ_{Bat} can be calculated at the end of the iterative process as shown in equation 4.15. With these parameters it can be observed directly which fraction of m_{MTO} is reserved for the energy storage system to perform a certain mission.

$$\xi_{Fuel} = \frac{m_{Fuel}}{m_{MTO}} \qquad \text{and} \qquad \xi_{Bat} = \frac{m_{Bat}}{m_{MTO}} \tag{4.15}$$

The mass of the required fuel $\Delta m_{Fuel,i}$ and battery $\Delta m_{Bat,i}$ for each segment i is calculated with equations 4.16 and 4.17. In equation 4.16 the efficiency η_{ICE}, the fuel mass $\Delta m_{Fuel,i}$ and the specific energy of the fuel $E_{s,Fuel}$ is related to the output power P_{ICE} of the combustion engine which is provided over the time ΔT_i. A similar equation is found for the battery mass, containing the battery integration factor α_{Int} and the capacity fade factor α_{Deg}, which are described in section 3.4. By summing up the required fuel and battery mass for all flight segments, the total required fuel and battery mass can be determined as shown in equation 4.18.

$$\Delta m_{Fuel,i} \cdot E_{s,Fuel} \cdot \eta_{ICE} = P_{ICE} \cdot \Delta t_i \tag{4.16}$$

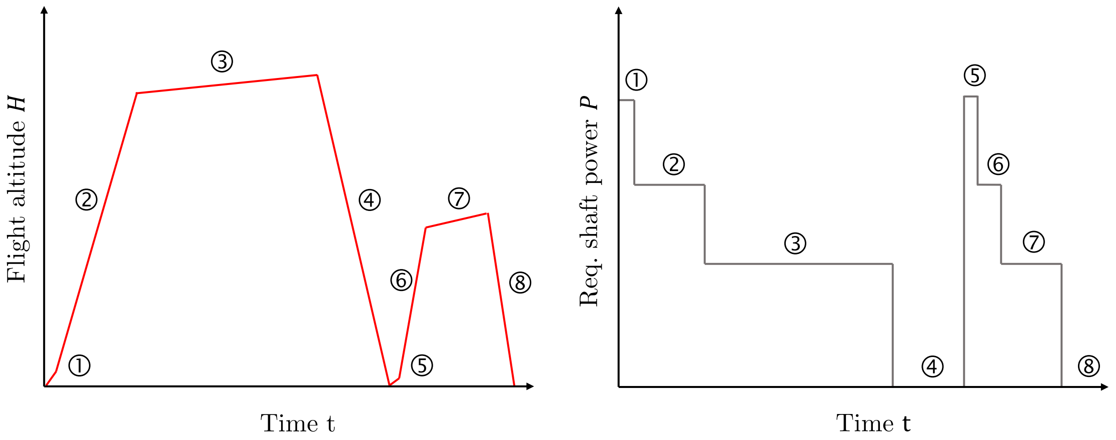

Figure 4.6: Schematic graph of altitude and required power during the flight mission

$$\Delta m_{Bat,i} \cdot E_{s,Bat} \cdot \alpha_{Int} \cdot \alpha_{Deg} = P_{Bat} \cdot \Delta t_i \tag{4.17}$$

$$m_{Fuel} = \sum_{i=1}^{n} \Delta m_{Fuel,i} \qquad \text{and} \qquad m_{Bat} = \sum_{i=1}^{n} \Delta m_{Bat,i} \tag{4.18}$$

The shaft power in a series hybrid-electric aircraft is given by equation 4.19. Based on the required shaft power $P_{sh,req}$ for the current flight segment and the maximum available power of the combustion engine(s) $P_{ICE,max}$, two modes of operation can be identified, under the assumption that as least as possible battery mass shall be required in the corresponding flight segment. In operation mode I the momentary available power of the combustion engine is not sufficient and additional battery power is required, whereas in operation mode II the required power can be covered entirely by the combustion engine. The operation modes are summarized in table 4.7. The described operation strategy corresponds to the minimum battery mass required for the considered flight segment and consequently leads to the minimum battery mass required for the entire mission.

$$P_{sh,req} = \eta_{EM} \cdot (P_{Bat} + \eta_{Gen} \cdot P_{ICE}) \tag{4.19}$$

4.2.1 Take-off

During take-off, the required propulsive power of the aircraft is highest and consequently the combustion engine provides its maximum power (operation mode I). With

Mode	**Condition**	**ICE* power** $\boldsymbol{P_{ICE}}$	**Battery power** $\boldsymbol{P_{Bat}}$
I	$P_{sh,req} \geq P_{ICE,max}(H) \cdot \eta_{EM} \cdot \eta_{Gen}$	$P_{ICE,max}(H)$	variable
II	$P_{sh,req} < P_{ICE,max}(H) \cdot \eta_{EM} \cdot \eta_{Gen}$	variable	0

Table 4.7: Considered modes I and II for the operation of the series hybrid-electric propulsion system (* = internal combustion engine)

equation 4.19 for the shaft power of a series hybrid-electric aircraft and the equation 4.16 for conservation of energy, a formula for the required fuel mass $\Delta m_{Fuel,TO}$ can be deduced as shown on equation 4.20. With equation 4.19 for the shaft power of a series hybrid-electric aircraft, the battery mass can be calculated similarly as shown in equation 4.21, where the difference between required shaft power $P_{sh,TO}$ and provided power of the combustion engine $\eta_{EM} \cdot \eta_{Gen} \cdot P_{ICE,max}$ is considered.

$$\Delta m_{Fuel,TO} = \frac{P_{ICE,max} \cdot \Delta t_{TO}}{\eta_{ICE} \cdot E_{s,Fuel}} \tag{4.20}$$

$$\Delta m_{Bat,TO} = \left(\frac{P_{sh,TO}}{\eta_{EM}} - \eta_{Gen} \cdot P_{ICE,max} \right) \cdot \frac{\Delta t_{TO}}{\alpha_{Int} \cdot \alpha_{Deg} \cdot E_{s,Bat}} \tag{4.21}$$

In equation 4.22 the formula for the take-off field length is shown containing the aircraft design parameters: specific wing loading $({}^{m_{MTO}}/_{S_w})$ and power loading $({}^{P_{sh,max}}/_{m_{MTO}})$. The wing loading $({}^{m_{MTO}}/_{S_w})$ is kept constant in order to achieve a compromise between low stall speed and efficient cruise performance. As a result, it can be deduced from equation 4.22 that the specific power loading $({}^{P_{sh,max}}/_{m_{MTO}})$ has to stay constant as well if a certain take-off field length s_{TOFL} is required for the transport mission, under the assumption that the type of high-lift system with its maximum lift coefficient $c_{L,max,TO}$ and the air density factor $({}^{\rho}/_{\rho_0})$ is kept constant. Consequently, the required take-off shaft power $P_{sh,max}$ increases if the maximum take-off mass m_{MTO} increases, which is described in equation 4.23.

$$s_{TOFL} = k_{TO} \cdot \frac{({}^{m_{MTO}}/_{S_w})}{({}^{\rho}/_{\rho_0}) \cdot c_{L,max,TO} \cdot ({}^{P_{sh,max}}/_{m_{MTO}})} \tag{4.22}$$

$$P_{sh,TO} = ({}^{P_{sh,max}}/_{m_{MTO}}) \cdot m_{MTO} \tag{4.23}$$

4.2.2 Climb flight

A steady climb flight is described by equation 4.24, where a climb flight with a climb angle of γ is related to the required shaft power $P_{sh,Climb}$ [86] [78]. In the climb flight phase various parameters change. If a gas turbine is installed in the hybrid-electric propulsion system the efficiency $\eta_{ICE,max}$ increases with increasing flight altitude as described in section 3.2. Further, the maximum power is reduced with increasing altitude, the aircraft mass decreases as fuel mass is burnt and the glide ratio changes as result of changing air density and aircraft mass. These changes are not covered by the equation 4.24. In order to account for the described effects, a segmentation of the climb flight is implemented which is shown in Fig. 4.7 and the climb phase is split into segments where the parameters ${}^{L}\!/_{D}$, $P_{ICE,max}$, η_{ICE} and the aircraft mass can be regarded constant. The calculation of the segments hereby requires a mean aircraft mass $m_{A/C,Climb,mean}$ – as a result, an iteration within in the calculation of the individual climb segments is necessary.

$$P_{sh,Climb} = \frac{v \cdot m_{A/C,Climb,mean} \cdot g}{\eta_{P+I}} \cdot \left(\frac{1}{{}^{L}\!/_{D}} + \gamma \right) \tag{4.24}$$

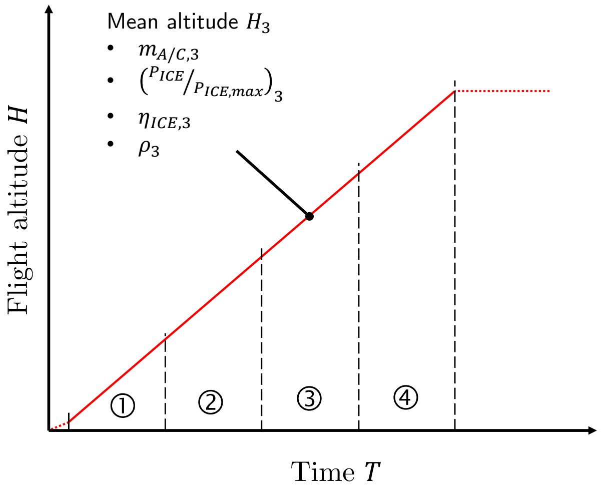

Figure 4.7: Segmentation of climb flight in order to account for changes in aircraft mass, partial engine load, engine efficiency and air density

If the required shaft power exceeds the maximum power of the combustion engine $P_{ICE,max}$ the required fuel mass $\Delta m_{Fuel,Climb}$ and battery mass $\Delta m_{Bat,Climb}$ can be calculated similarly as for take-off.

$$\Delta m_{Fuel,Climb} = P_{ICE,max} \cdot \frac{\Delta t_{Climb}}{\eta_{ICE} \cdot E_{s,Fuel}} \tag{4.25}$$

$$\Delta m_{Bat,Climb} = \left(\frac{P_{sh,Climb}}{\eta_{EM}} - \eta_{Gen} \cdot P_{ICE,max} \right) \cdot \frac{\Delta t_{Climb}}{\alpha_{Int} \cdot \alpha_{Deg} \cdot E_{s,Bat}} \tag{4.26}$$

If the required shaft power in the climb segment is lower than the maximum available power of the combustion engine, the required fuel mass can be calculated using equation 4.16.

$$\Delta m_{Fuel,Climb} = \frac{P_{sh,Climb}}{\eta_{EM} \cdot \eta_{Gen}} \cdot \frac{\Delta t_{Climb}}{\eta_{ICE} \cdot E_{s,Fuel}} \tag{4.27}$$

4.2.3 Cruise flight

The required propulsive power for cruise flight is given in equation 4.28. In cruise flight the glide ratio and the true air speed are regarded as constant, if the cruise altitude is raised slightly over time. As a result, an integration over time is simplified and a variation of the aircraft mass described in equation 4.29 can be taken into account.

$$P_{sh,Cruise} = \frac{m_{A/C} \cdot g \cdot v}{\eta_{P+I} \cdot {}^{L}\!/_{D}} \tag{4.28}$$

$$\frac{dm_{A/C}}{dt} = -\frac{P_{ICE}}{\eta_{ICE} \cdot E_{s,Fuel}} \tag{4.29}$$

If the required power for cruise flight is lower than the available power of the combustion engine ($P_{ICE} = {}^{P_{sh,Cruise}}\!/_{\eta_{EM} \cdot \eta_{Gen}}$ and $P_{Bat} = 0$) a variation of the Breguet's range equation can be deduced, shown in 4.30. Consecutively, the formula for the fuel mass $\Delta m_{Fuel,i}$ is found in equation 4.31. In order to abbreviate to following formulas, the parameter $p_{sh,Cruise}$ is introduced. It can be interpreted as a required power loading for cruise flight.

$$R_{Cruise} = \eta_{P+I} \cdot \eta_{EM} \cdot \eta_{Gen} \cdot \eta_{ICE} \cdot \frac{L}{D} \cdot \frac{E_{s,Fuel}}{g} \cdot \ln \frac{m_{A/C,Cruise,begin}}{m_{A/C,Cruise,begin} - m_{Fuel,Cruise}} \tag{4.30}$$

$$\Delta m_{Fuel,Cruise} = m_{A/C,Cruise,begin} \cdot \left[1 - \mathrm{e}^{\left(\frac{p_{sh,Cruise} \cdot T_{Cruise}}{\eta_{EM} \cdot \eta_{Gen} \cdot \eta_{ICE} \cdot E_{s,Fuel}} \right)} \right] \tag{4.31}$$

$$\text{with} \qquad p_{sh,Cruise} = \frac{g \cdot v}{\eta_{P+I} \cdot {}^{L}\!/_{D}} \tag{4.32}$$

If the hybrid-electric propulsion system cannot cover the cruise power by the power of the combustion engine (operation mode ① with $P_{ICE} = P_{ICE,max}$ and $P_{Bat} = variable$), the required fuel mass can be determined by equation 4.33.

$$\Delta m_{Fuel,Cruise} = P_{ICE,max} \cdot \frac{\Delta t_{Cruise}}{\eta_{ICE} \cdot E_{s,Fuel}} \tag{4.33}$$

The required additional battery energy for the cruise segment can be determined by combining equations 4.19, 4.28 and 4.32 to derive equation 4.34. The resulting equation can be used for a formula describing the needed battery power as shown in equation 4.35.

$$p_{sh,Cruise} \cdot m_{AC}(t) = \eta_{EM} \cdot (P_{Bat} + \eta_{Gen} \cdot P_{ICE,max}) \tag{4.34}$$

$$P_{Bat} = \frac{p_{sh,Cruise}}{\eta_{EM}} \cdot m_{A/C}(t) - \eta_{Gen} \cdot P_{ICE,max} \cdot f(H) \tag{4.35}$$

In order to calculate the required battery energy in the cruise segment, the integral of equation 4.35 is calculated shown in equation 4.36, where terms which remain constant over time can be moved to the front of the integral. The reduced mass of the aircraft due to the combustion of fuel is described by equation 4.37. By introducing the relation, the integral can be solved and the required battery energy can be determined as shown in equation 4.38.

$$E_{Bat,Cruise} = \int_0^{\Delta t} P_{Bat} \cdot dt = \int_0^{\Delta t} \left[\frac{p_{sh,Cruise}}{\eta_{EM}} \cdot m_{A/C}(t) \right] dt - \int_0^{\Delta t} \eta_{Gen} \cdot P_{ICE,max} \, dt \tag{4.36}$$

$$\text{with} \qquad m_{A/C}(t) = m_{A/C,Cruise,begin} - \frac{P_{ICE,max}}{\eta_{ICE} \cdot E_{s,Fuel}} \cdot t \tag{4.37}$$

$$E_{Bat,Cruise} = \frac{p_{sh,Cruise}}{\eta_{EM}} \cdot \left(m_{A/C,Cruise,Begin} \cdot \Delta t - \frac{P_{ICE,max}}{\eta_{ICE} \cdot E_{s,Fuel}} \cdot \frac{\Delta t^2}{2} \right) - \eta_{Gen} \cdot P_{ICE,max} \cdot \Delta t \tag{4.38}$$

The required battery energy can be then converted into a required battery mass $m_{Bat,i}$ for the segment i as shown in equation 4.39.

$$\Delta m_{Bat,Cruise} = \frac{E_{Bat,Cruise}}{\alpha_{Int} \cdot \alpha_{Deg} \cdot E_{s,Bat}} \tag{4.39}$$

4.2.4 Descent

In the descent flight phase no propulsive power is needed, as the drag can be compensated by a component of the gravitational force. However, in conventional aircraft the combustion engines are not shut-down in this phase in order to be quickly able to apply propulsive power to adjust the flight path. As a result, an idle consumption contributes to the required mission fuel. A possible operational advantage of hybrid-electric propulsion systems is that the combustion engine does not necessarily need to run idle in the descent phase of the flight mission. If the battery system is able to provide sufficient propulsive power to adjust the flight path and to execute a traffic pattern ("go around") due to a missed approach at the destination airport, the combustion engine could be switched on only if necessary.

4.2.5 Operational reserves

Energy reserves are legally required for the operation of a fixed-wing aircraft and are required to account for adverse weather conditions and disorder of flight operations at the destination airfield. The annex VII of the European regulation 965/2012 [87] specifies in its paragraph NCO.OP.125 operational reserves which are mandatory for flight operations. The required reserve depends on the type of flight operation: reserves for flights according to "Visual Flight Rules" (VFR) differ from flights using "Instrument Flight Rules" (IFR):

- Reserves for flights according to Visual Flight Rules
  - For flights in airport vicinity: Provide reserve energy for a traffic pattern with a flight time of 10 minutes
  - For cross-country flight during day: Provide reserve energy for a 30 minutes flight at the destination airport
  - For cross-country flight during night: Provide reserve energy for a 45 minutes flight at the destination airport
- Reserves for flights according to Instrument Flight Rules
  - If an alternate airport is required: Provide energy for a flight from the destination airport to the alternate airport and an additional flight reserve of 45 minutes
  - If no alternate airport is required: Provide reserve energy for a 45 minutes flight at the destination airport

The flight segments for the reserves are treated as additional climb, cruise and descent phases. In chapter 5 two hybrid-electric aircraft are investigated which are both intended for cross-country flight. The first one is intended for VFR-flights which are usually carried out during day – consequently, a 30 minute flight reserve will be considered for this aircraft. The second hybrid-electric aircraft is conceived for IFR-flights.

As the majority of IFR-flights require an alternate airport for flight operation, a reserve consisting of a flight to the alternate airfield and an additional flight reserve of 45 minutes is taken into account.

4.2.6 Influence of component failures on power reserves

The considered aircraft in this thesis are subject to the certification specification CS-23 which covers fixed-wing aircraft with a maximum take-off mass of 5618 kg and 8616 kg respectively for commuter class aircraft. The regulation distinguishes between single-engine aircraft and multi-engine aircraft. As no special conditions for hybrid-electric aircraft are established at present of this thesis, a preliminary equivalent level of safety shall be determined. The energy storage system of a series hybrid-electric aircraft can be considered as a multi-engined aircraft. Consequently, it would be subject to the climb requirements specified in paragraph CS 23.2120, which states: "after a critical loss of thrust" a 1% climb angle is required with the landing gear retracted and flaps in the take-off configuration. A critical loss of thrust is produced in this specific application by a loss of combustion engine power or a loss of battery power. A battery system is usually segmented into different battery packs. Consequently, a failure of one battery pack and a failure of one combustion engine have to be considered.

Depending on the airworthiness certification requirements and the failure rates of the propulsion components, different scenarios for power reserves of the hybrid-electric propulsion system are plausible. If the propulsion system contains only one combustion engine, the battery system might be subject to one of the following conditions in case this engine fails:

- No compensation of the ICE-power (similar to current single-engine aircraft of the General Aviation)
- Partial compensation of the ICE-power to achieve a positive climb gradient according to CS 23.2120
- Full compensation of the ICE-power

In a series hybrid-electric propulsion system, at least two electric machines, two converters and a power distribution system are integrated in between the combustion engine and the propeller as shown in Fig. 2.4. These additional components contribute their individual failure rates to the failure rate of the overall propulsion system. Compared to a conventional propulsion system, which consists of a single combustion engine coupled to a propeller, the failure rate of the propulsion system would be increased if no battery system is available as a back-up system. Hence, a equivalent level of safety on preliminary aircraft design level is questionable. The option to not compensate the power loss in case of a combustion engine failure is not considered.

A partial compensation of the ICE-power might require a multi-engine pilot training, as a take-off with merely 1% climb angle requires detailed flight planning and pilot skills. This would handicap the introduction of serial-hybrid aircraft as less pilots would be able to fly these aircraft. As a result, full power compensation is taken as the equivalent level of safety. In equation 4.40 the power split during take-off is defined. It is a design parameter for hybrid-electric aircraft and describes which fraction of the required shaft power during take-off $P_{sh,TO}$ is covered by the power of the battery system $P_{Bat,TO}$. The factor η_{EM} incorporates the losses of the electric machine and its inverter.

$$S_{TO} = \frac{\eta_{EM} \cdot P_{Bat,TO}}{P_{sh,TO}} \tag{4.40}$$

In case of a failure of a combustion engine the power loss during take-off needs to be compensated. The required, increased battery power $P_{Bat,max}$ is determined with equation 4.42, which is significantly influenced by the battery power split S_{TO} and the number of combustion engines n_{ICE}. In case of a single combustion engine with n_{ICE}=1, the battery system is required to be able to provide the entire take-off power.

$$P_{Bat,max} = \frac{P_{sh,TO}}{\eta_{EM}} - \eta_{Gen} \cdot \left(\frac{n_{ICE} - 1}{n_{ICE}}\right) \cdot P_{ICE,max} \tag{4.41}$$

$$P_{Bat,max} = \left(S_{TO} + \frac{1 - S_{TO}}{n_{ICE}}\right) \cdot \frac{P_{sh,TO}}{\eta_{EM}} \tag{4.42}$$

A battery system consists of several battery packs, which are all connected to the same bus bar. In case of a failure of an individual battery pack (e.g. due to a failure of a battery cell) it can be disconnected from the bus bar via a relay. The housing of a battery pack is required to contain a fire and to prevent a pack to pack propagation of it. This can be realized e.g. with an appropriate firewall and separated installation spaces for battery packs.

The excess power of the battery system needed to compensate a failure of a combustion engine, can be used to compensate a failure of a battery pack as well as shown in Fig. 4.8. As a result, no additional battery mass is needed. However, a specific number of segmentation of the battery system into battery packs is necessary. This minimum number of battery packs n_{Bat} can be deduced by requiring that the power loss in case of a battery pack failure is lower than the battery excess power, calculated by the difference of maximum battery power $P_{Bat,max}$ and battery power during take-off $P_{Bat,TO}$.

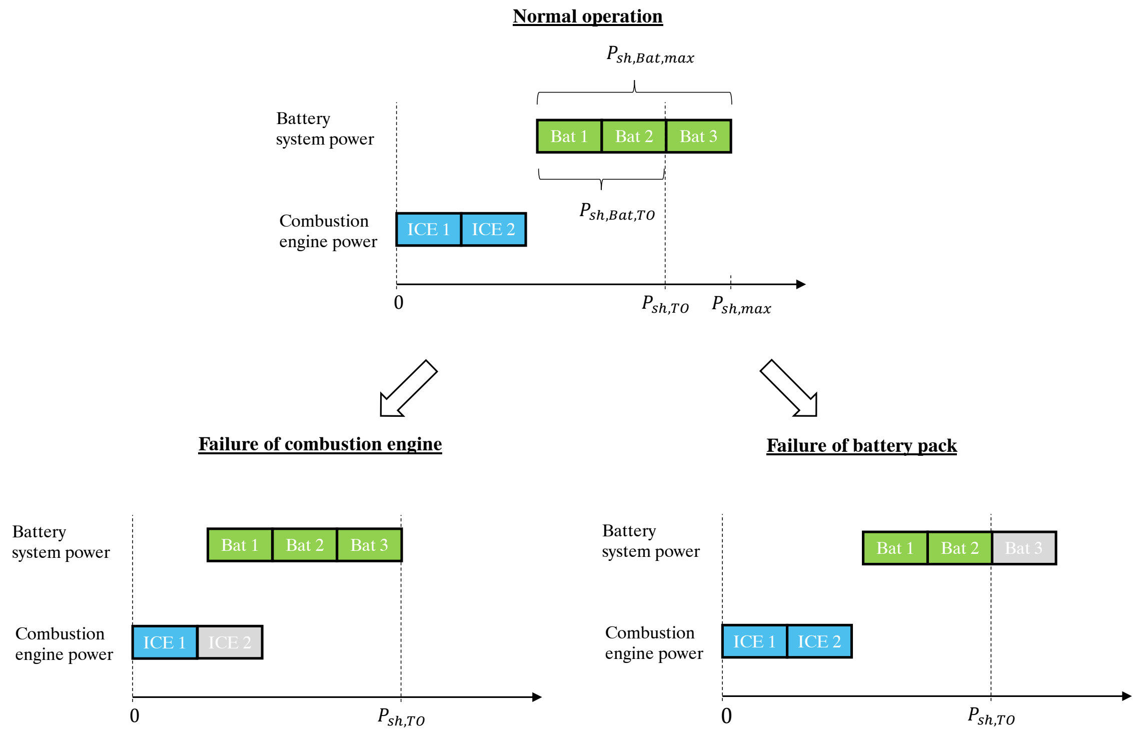

Figure 4.8: Sizing of a hybrid-electric propulsion system, which can compensate the power loss resulting from a combustion engine or a battery pack failure

$$\frac{1}{n_{Bat}} \cdot P_{Bat,max} \leq P_{Bat,max} - P_{Bat,TO} \tag{4.43}$$

$$n_{Bat} \geq \frac{P_{Bat,max}}{P_{Bat,max} - P_{Bat,TO}} \tag{4.44}$$

Consequently, a formulation for the minimum number of battery packs is found in equation 4.44. By substituting the required maximum battery power from equation 4.42 and the battery take-off power from equation 4.40, the relation between the number of combustion engines n_{ICE}, power split S_{TO} and required number of battery packs can be deduced as shown in equation 4.45.

$$n_{Bat} \geq \frac{(n_{ICE} - 1) \cdot S_{TO} + 1}{1 - S_{TO}} \tag{4.45}$$

It is shown in table 4.8 that the required segmentation of the battery system n_{Bat} stays within a feasible range. As only integer values are acceptable for the number of battery packs n_{Bat}, the resulting values from equation 4.45 are brought up to a round figure.

S_{TO}	n_{Bat} for $n_{ICE} = 1$	n_{Bat} for $n_{ICE} = 2$
0.01	2	2
0.2	2	2
0.4	2	3
0.6	3	4

Table 4.8: Minimum number of segmentation of the battery system n_{Bat} in order to compensate a battery pack failure during take-off

4.2.7 Influence of component failures on energy reserves

As described in section 4.2.6 a power loss due to a combustion engine failure shall be compensated in order to achieve an equivalent level of safety on preliminary aircraft design level. In case of a failure of a combustion engine or a battery pack during cruise flight, the energy system should provide sufficient flight time to reach an airfield and to carry out an emergency landing. Generalized data for the distance to such an emergency airfield is not available and an educated assumption is non-trivial. The National Business Aviation Association (NBAA) provides in its range format [88] an assumption for the distance from a destination airfield to an alternate airfield. This range is part of the required reserve for flights according to Instrument Flight Rules and is assumed to be 100 nautical miles (NM) for turbo-prop driven business aircraft and 200 NM for jet business aircraft. However, the intent of the range format was to "provide a standard for prospective aircraft purchasers to use in comparing the performance of various aircraft". It does not state a general existence of an alternate airport within the stated ranges.

The residual range of a hybrid-electric aircraft after a failure of a combustion engine or a battery pack is a design parameter which affects the performance of the aircraft. If the range is longer than required, the mass and, consequently, the fuel consumption of the aircraft will be increased. If the range is below a practical value, the operation of the aircraft would be limited. As a result, a more detailed analysis is needed to determine the required value of this design parameter. The analysis is carried out for Europe and the continental part of the United States of America, which is a key market for general aviation aircraft. According to the General Aviation Manufacturers Association [8] 61.5 % of piston-driven airplanes manufactured worldwide were sold to North America in 2018.

For the determination of the required residual range of a hybrid-electric aircraft, the position data of suitable emergency airports in the investigated region is required. The Aeronautical Information Publication (AIP) with its chapter Aerodromes (AD)

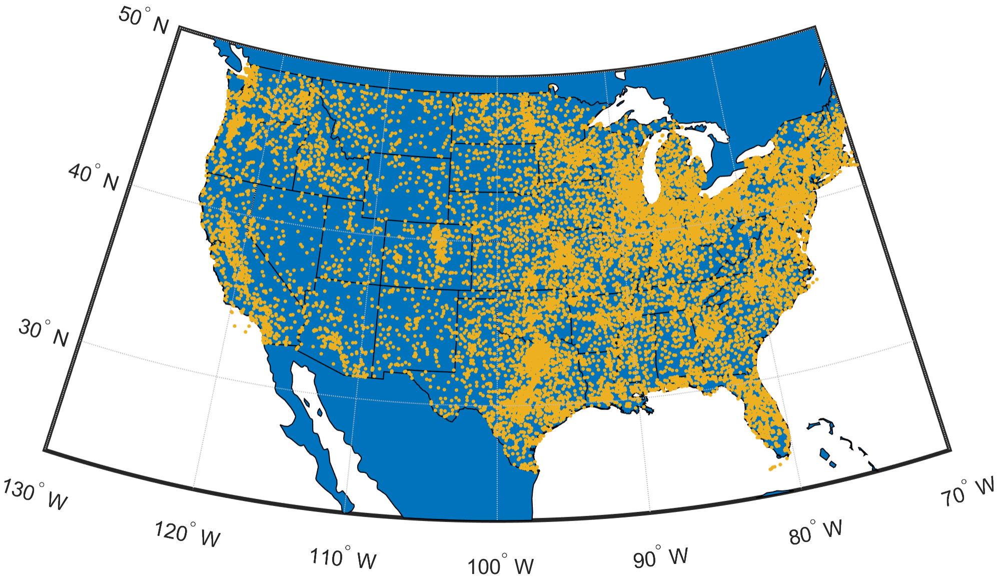

Figure 4.9: Location of suitable emergency airports in the continental part of the USA with a runway length greater than 640 m

contains all relevant information of airports and airfields, which are necessary for pilots to plan and conduct flights. It contains e.g. latitude, longitude and elevation of the airfield, length and width of runways as well as radio frequencies and further operational data. In [89] an electronic version of the AIP data is available, which was converted to a Matlab-compatible format and used for the further investigation. The data base comprises of e.g. 20,671 civil airfields for the United States of America. Filtering the data for heliports, closed airports and seaplane bases leaves 13,283 airports for consideration. The hybrid-electric aircraft investigated in chapter 5 require a landing field length of approx. 640 m of a grass, asphalt or concrete runway. As a result, airports with lower landing field lengths were excluded from the data set as well, leaving 9,561 suitable emergency airports in the USA shown in Fig. 4.9. For the investigated part of Europe shown in Fig. 4.10, the AIP was obtained for the 27 member states of the European Union as well as the United Kingdom, Norway, Switzerland, the Balkans, Ukraine and Belarus. Filtering out heliports, military and closed airports as well as mountain airfields on glaciers and seaplane bases left 3,808 airports. Excluding airports with a runway shorter than 640 m left 2,621 suitable emergency airports for further consideration.

As a next step, a mesh of possible aircraft positions over land was created expressed in latitude ϕ and longitude ψ. Aircraft positions over sea and islands were excluded at this stage. The mesh applied in the calculation consists of positions with a spacing of

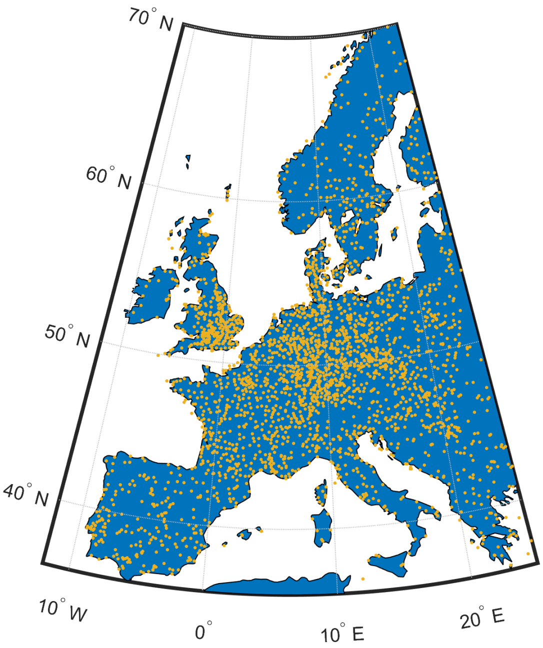

Figure 4.10: Location of suitable emergency airports of the investigated part of Europe with a runway greater than 640 m

$1/60°$ in latitude $\Delta\phi$ and longitude $\Delta\psi$. In Fig. 4.11 an exemplary mesh is shown with a spacing of 1° in latitude and longitude. Consequently, the shortest distance of each aircraft position to the suitable airports is determined, by calculating the length d of the great circle arc to each individual airfield using equation 4.46. In the equation, C_{Earth} denotes the circumference of the Earth and ζ represents the angle of the great circle arc. The angle ζ can be calculated using equation 4.47 [90], where ϕ_A and ψ_A represent latitude and longitude of the aircraft position and ϕ_B and ψ_B denote the coordinates of the airport. The distance to the closest emergency airport is then determined by finding the lowest value of d for each investigated aircraft position.

$$d = \zeta \cdot C_{Earth} \tag{4.46}$$

$$cos(\zeta) = sin(\phi_A) \cdot sin(\phi_B) + cos(\phi_A) \cdot cos(\phi_B) \cdot cos(\psi_A - \psi_B) \tag{4.47}$$

The results of the calculation are shown in the histograms in Fig. 4.12. The results are categorized in bins where each bin covers a certain spectrum of distances. E.g. the first bin contains all distances from zero to five nautical miles. By plotting the

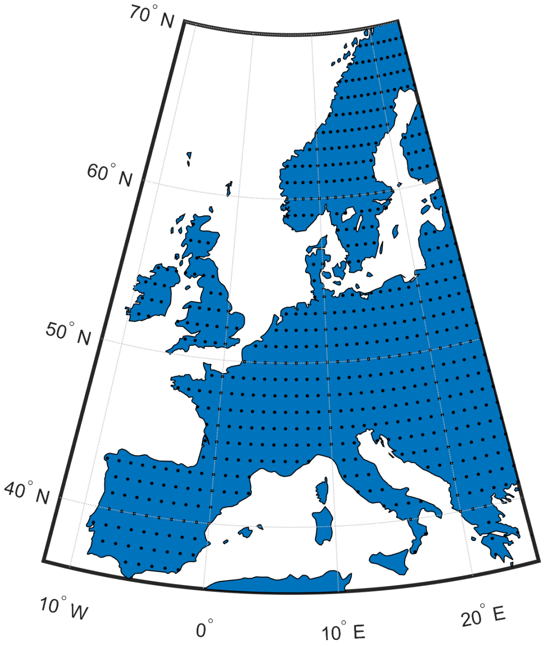

Figure 4.11: Exemplary visualization of investigated aircraft positions in Europe with a spacing of 1° in latitude and longitude – the calculation was carried out with a spacing of $1/60°$, which results in a spacing of approximately 1 nautical mile

number of values contained in each bin, an estimate of the probability distribution of the continuous variable can be shown.

A cumulative frequency analysis can be performed, where it is determined how often, in other words with which frequency, the distance to the nearest emergency airport is below a certain value. For the calculation of the cumulative frequency the results need to be sorted from the lowest to the highest value. Consequently, the cumulative frequency F can be calculated using equation 4.48, where n corresponds to the total number of data and $M(x)$ is the number of data points below the threshold x. In Fig. 4.13 the resulting curve is plotted for the USA and Europe. It can be deduced that for 95 % of the aircraft positions in the USA a suitable emergency airport with a runway of at least 640 m exists within a distance of 23.7 NM. For 99 % of the aircraft positions this distance increases to 33.8 NM. For the investigated part of Europe, 95 % and 99 % of the aircraft positions possess a distance to a suitable airfield of less than 36.0 NM and 48.6 NM respectively. With these results, it can be deduced that less suitable airfields exist in the investigated part of Europe than in the continental part of the USA. In Fig. 4.13 the median for Europe is shown, indicating that for 50 % of the aircraft positions the closest suitable airport is within a radius of 12.6 NM. For a

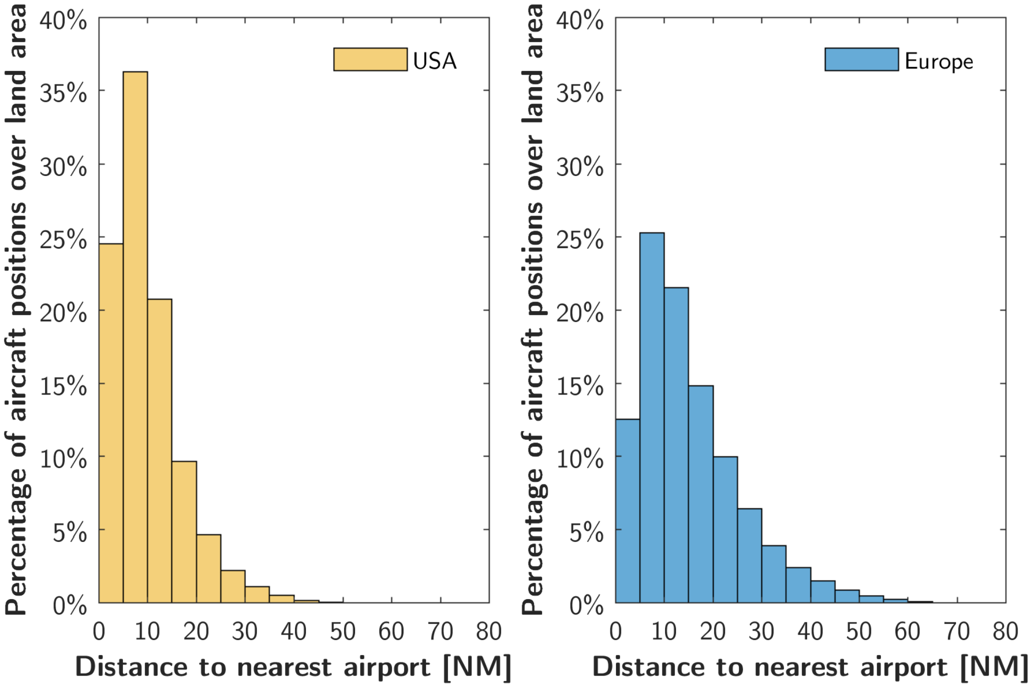

Figure 4.12: Histogram of results for calculation to determine nearest suitable airport for an emergency landing

plausibility check, the mean airport density of the USA is compared to the mean airport density of Europe, which reveals that in the USA 0.97 airports exist per 1,000 km^2 whereas in the investigated part of Europe only 0.44 airports exist per 1,000 km^2.

$$F(x) = {}^{M(x)}\!/_{n} \tag{4.48}$$

The maximum error of the calculation is evaluated by considering the distance of a possible aircraft position, which is located exactly in between the mesh of aircraft positions shown in Fig. 4.11. Furthermore, the distance of the great circle between different longitudes is highest at the equator and decreases to South and North Poles. As a result, the maximum error of the calculation is evaluated at the position which is closest to the equator, which is the southern coast of Florida with a latitude of 25°. As the spacing of the positions in latitude and longitude is $^1\!/_{60}$°, the maximum error of the calculation can be determined to be 0.68 NM.

For the further aircraft design the 95-percentile of the range to an emergency airport was applied, as it covers the significant majority of aircraft positions over land. Further, the range of Europe was used as it is longer than the range of the USA. Furthermore, safety margins are applied in order to derive from the theoretical range of the length

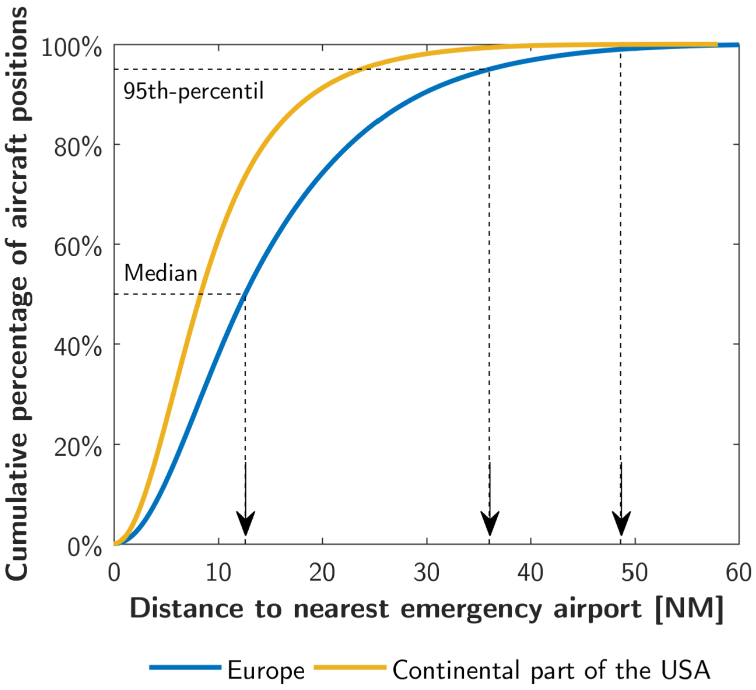

Figure 4.13: Plot of cumulative frequency showing e.g. that for 95 % of aircraft positions in Europe a suitable airport is within a distance of 36.0 nautical miles

of the great circle arc to a practical range, which enables pilots to reach an emergency airport under non-ideal flight conditions. A first safety margin shall be applied in order to account for a delay of the appropriate pilot reaction in case of a failure of a propulsion component. In [91] the response time of 29 general aviation pilots to failures of autopilot has been tested. It was found that response times for the detection of "slow" failure types are in the order of magnitude of 100 seconds. This time gives an indication which safety margin is required to allow for an appropriate pilot response in case of a failure of a combustion engine in a series hybrid-electric aircraft. For an aircraft with a cruise speed of 220 km/h, this equals to a distance of 3.3 NM. A further safety margin should consider adverse head wind conditions, which increase the energy required to reach the diversion airport. If e.g. a "moderate breeze" on the Beaufort Scale [92] is taken as the reference value with wind speeds up to 28 km/h, the flight time of an aircraft with a cruise speed of 220 km/h would be increased by 13 %. Consequently, the required energy to reach the emergency airport is increased accordingly. When the aircraft has reached the airport, further flight time is necessary to carry out a traffic pattern. In [93] approximate values for the individual parts of the traffic pattern of a motorized general aviation airplane are given: departure, crosswind leg, downwind leg, base leg and final approach should be 1.5 km long. Taken the mean runway length of 1,340 m from the filtered airfields in Europe, the length of a complete traffic pattern including take-off and landing is 11.7 km. It is valid to assume that for landing only, half of the flight path is required. Consequently, an additional reserve of 6 km is assumed. Exemplary, the influence of the additional reserves is evaluated for a general aviation aircraft with a cruise speed of 220 km/h. The 95-percentile of the distance to an emergency airport in Europe is 36.0 NM. Adding the described factors, the required flight range would increase to 48 NM. Depending on the type of aircraft and flight profile, flight altitude could be used to reduce the energy necessary to reach the suitable emergency airport.

4.3 Aircraft sizing methodology

In a series hybrid-electric propulsion system the power of the combustion engine does not need to be sized to provide take-off power. Differently to conventional aircraft, the combustion engine can be sized to e.g. the power required for climb or cruise flight, with the battery system providing the remaining power. Furthermore, the required energy for flight can be either stored on-board the aircraft in liquid fuel or in a battery system. Further, the number of applied combustion engines has an impact onto the battery system, as a failure of a combustion engine in a propulsion system equipped with a single combustion engine requires more additional battery power than in a propulsion system which is equipped with multiple combustion engines. Hence, the sizing of a series hybrid-electric propulsion system offers new degrees of freedom. The further objective is to translate these new degrees of freedom into a set of equations suitable for optimization in order to find an optimized sizing of the propulsion system.

4.3.1 Sizing process for hybrid-electric aircraft

A suitable continuous input variable for the sizing of the hybrid-electric propulsion system is the power split S_{TO} and is introduced in equation 4.49. S_{TO} states which fraction of the take-off power can be covered by the battery system and is used in a similar form in the investigation of parallel hybrid-electric aircraft [94]. $S_{TO} = 1$ describes a propulsion system which is capable of a pure battery electric take-off – $S_{TO} = 0$ describes a propulsion system without a battery system, where the generated electricity of the generator is applied instantly to the electric motor which drives the propeller. As in conventional propeller-driven aircraft the power is referenced to the mechanical shaft power. Consequently, the maximum battery output power $P_{Bat,max}$

has to be distinguished from the maximum battery shaft power $(P_{Bat,max})_{shaft}$. As described in section 3.5, η_{EM} includes the efficiency of electric machine and inverter – power cable losses can be neglected at this stage as depicted in section 3.6.

$$S_{TO} = \frac{(P_{Bat,max})_{shaft}}{P_{sh,TO}} = \frac{\eta_{EM} \cdot P_{Bat,max}}{P_{sh,TO}} \tag{4.49}$$

A second suitable continuous input variable for the sizing process is the battery mass fraction ξ_{Bat}. It expresses the mass of the battery system as a fraction of the maximum take-off mass according to 4.50. All other continuous variables of the hybrid-electric propulsion system can be determined in the course of the sizing calculation. Apart from the continuous variables, the number of combustion engines n_{ICE} and the type of the combustion engines are non-continuous input variables for the sizing process.

$$\xi_{Bat} = \frac{m_{Bat}}{m_{MTO}} \tag{4.50}$$

In Fig. 4.14 the individual steps of the calculation are shown, which is implemented in Matlab R2018b. With the power split S_{TO} and the battery mass fraction ξ_{Bat} given, the required specific battery power $P_{s,Bat,max}$ of the battery cells is determined and the corresponding maximum specific energy of the battery cells $E_{s,Bat}$ is calculated as described in section 3.4. In the further iterative design process, a mean specific power $P_{s,Bat,mean}$ is calculated, which is used to determine the actual specific energy $E_{s,Bat,mean}$ of the battery cells achieved in the flight mission. However, as depicted in section 4.2.6, the required battery power $P_{Bat,max}$ increases if a power loss of a failure of one combustion engine has to be considered, where the resulting specific battery power $P_{s,Bat,max}$ depends on the number of combustion engines n_{ICE} as shown in equation 4.51.

$$P_{s,Bat,max} = \frac{\left(S_{TO} + \frac{1-S_{TO}}{n_{ICE}}\right) \cdot \left({}^{P_{max}}/_{m_{MTO}}\right)}{\xi_{Bat} \cdot \alpha_{Bat,int} \cdot \eta_{EM}} \tag{4.51}$$

In a next step, aerodynamic calculations are performed in which the area of the wing and stabilizers are estimated as described in section 4.1.2. Furthermore, the drag polar is calculated by evaluating the parasitic and induced drag according to section 4.1.3. Consequently, the absolute power of the combustion engine is determined, and in case of a gas turbine, the corresponding efficiency is calculated as depicted in section 3.2.1. In a subsequent program module the required fuel mass and battery mass for each flight segment is calculated as described in section 4.2. During this calculation, the minimum amount of required battery mass is determined. However, as ξ_{Bat} is an input value to the sizing process, a separate calculation determines if spare battery energy is

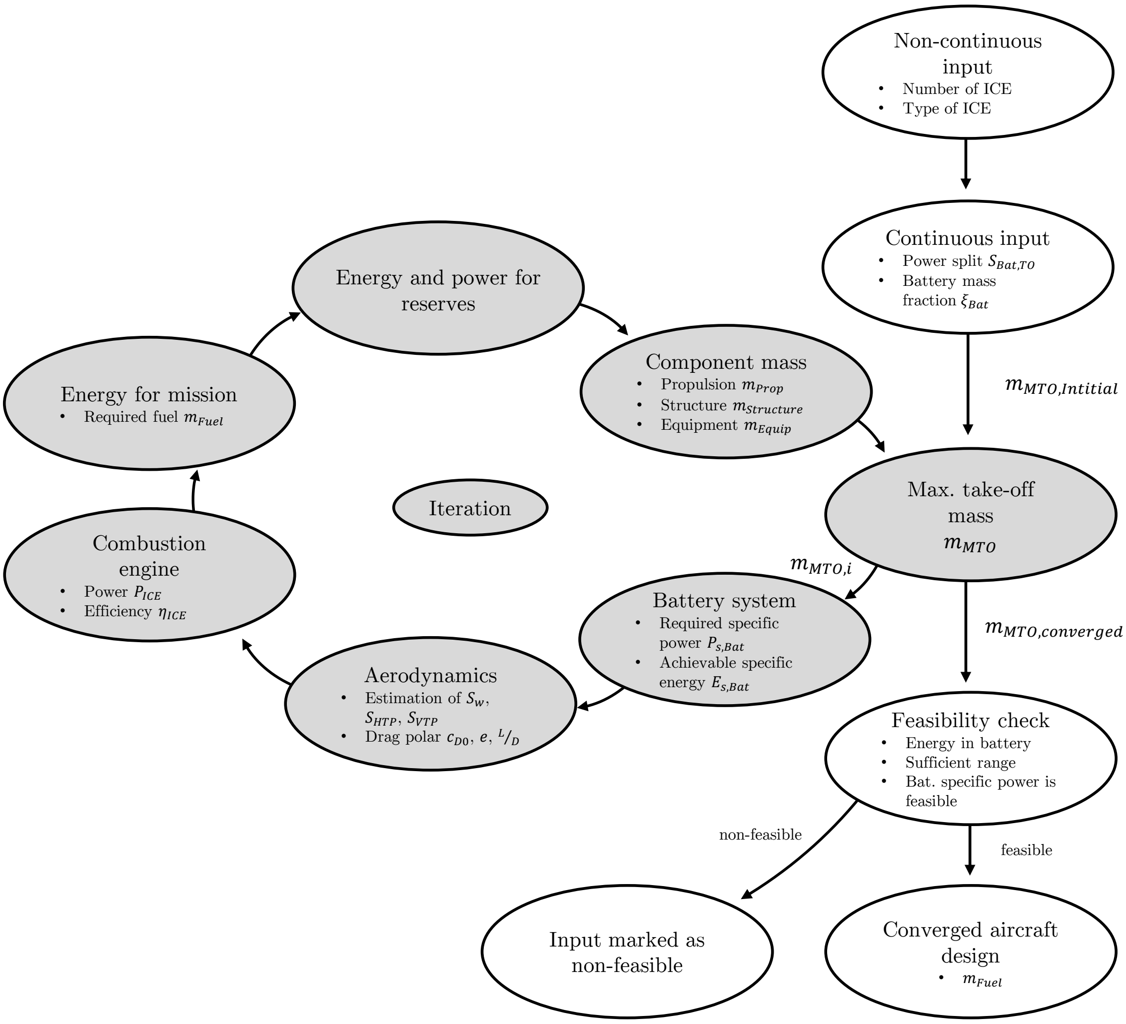

Figure 4.14: Scheme of aircraft sizing process implemented in Matlab

available which is not required for the segments of the mission nor the reserves discussed in sections 4.2.6 and 4.2.7. In case that unallocated battery energy is available, it is applied during flight and the fuel consumption is reduced accordingly. The battery energy is applied firstly to the last flight segments – as a consequence fuel gets used first and a potential advantage due to a lower aircraft mass at the end of the flight mission is incorporated. The same approach is applied when the aircraft is designed for a specific flight range and payload requirement but is evaluated for a shorter flight range in terms of fuel consumption or CO_2 emissions.

In the next section of the program, the empty mass is determined by calculating the mass of all structural components as well as the mass of the fixed equipment and the mass of the propulsion system as depicted in section 4.1.1. Consequently, a new maximum take-off mass m_{MTO} is calculated by adding the required fuel mass and the mass of the specified payload to the empty mass. The calculation is performed until a converged maximum take-off mass is achieved. The criteria to stop the iteration is reached when the change in maximum take-off mass between consequent calculations drops below 0.05%.

In order to derive a feasible aircraft design the following requirements are verified, after a converged maximum take-off mass has been reached. The requirements are discussed in detail in section 5.1.1 – if one or multiple of the requirements cannot be fulfilled, the corresponding pair of input variables of power split S_{TO} and battery mass fraction ξ_{Bat} is marked as part of a non-feasible design space. The requirements are:

- Presence of sufficient energy in battery system to provide additional power in flight segments where the combustion engines cannot cover the entire power demand
- Required specific power on battery cell level stays within the limit of investigated technology as depicted in section 3.4.1
- Maximum take-off mass does not exceed threshold value

4.3.2 Optimization of the hybrid-electric propulsion system

The described calculation process can be used to identify an optimized sizing of the hybrid-electric propulsion system. The continuous variables of power split $S_{ICE,TO}$ and battery mass fraction ξ_{Bat} are suitable for optimization by an gradient-based optimization algorithm. Fig. 4.15 shows how the optimization is implemented into the aircraft sizing calculation. The non-continuous variables number of combustion engines and type of combustion engines are varied manually. The optimal result is then determined by comparing manually the results of the different optimization carried out. If an optima, found by the optimization algorithm, is a global optima, can be verified by comparing the plot of $S_{ICE,TO}$, ξ_{Bat} and m_{Fuel} to the result of the optimization.

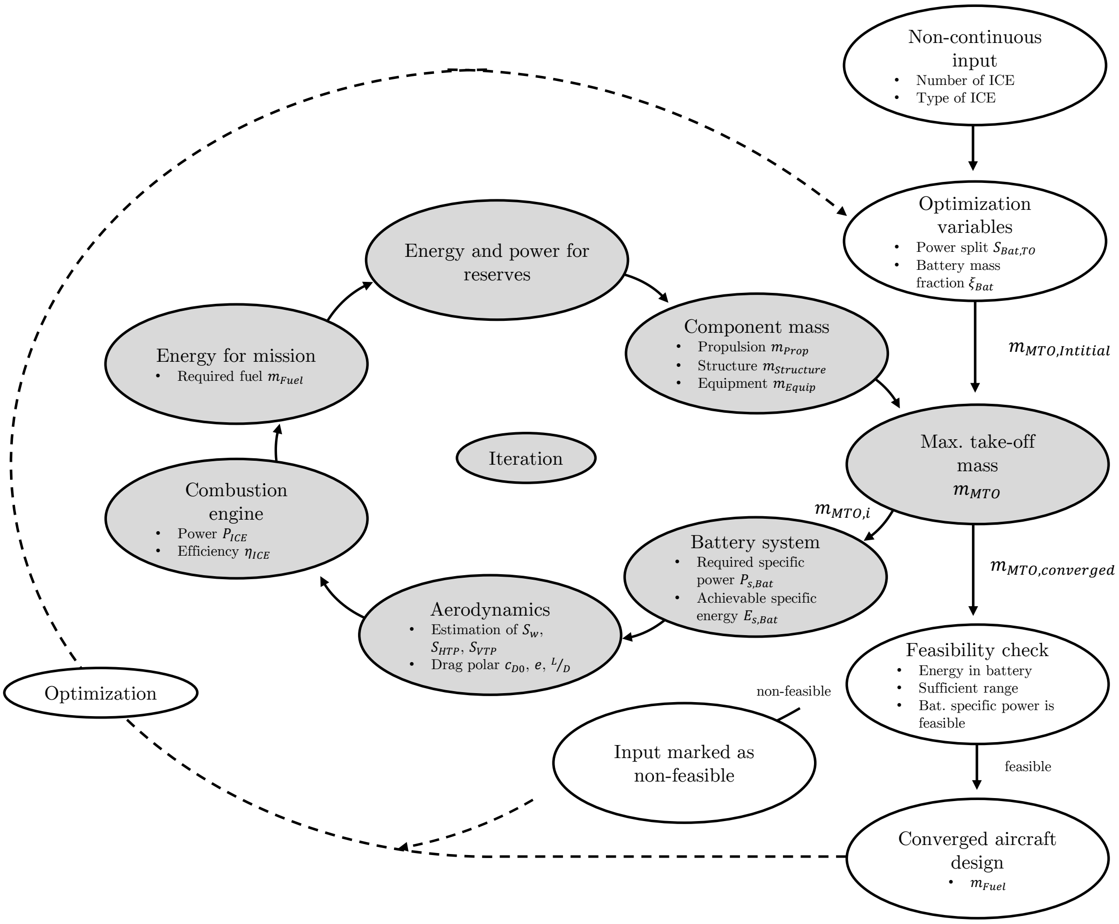

Figure 4.15: Scheme of the optimization of power split and battery mass fraction of the hybrid-electric propulsion system

Chapter 5

Aircraft sizing for different transport missions

The characteristics of the propulsion components discussed in chapter 3, their influence on the aircraft mass and the correlation to the drag of the aircraft described in chapter 4 are now applied to different transport missions. In the first section, a hybrid-electric 4-seat aircraft will be designed which is typically used for flights according visual flight rules. In the second, a hybrid-electric 9-seat aircraft is investigated, where the reserves allow an operation according to instrument flight rules. For each transport mission a modern conventional aircraft is used as a reference airplane to evaluate a possible fuel burn improvement achieved by the application of the hybrid-electric propulsion system. In order to improve the quality of the calculation, the conventional aircraft is sized by the same design calculation as the hybrid-electric aircraft and the results are compared to its existing counterpart. Thereby, confidence in the results is increased.

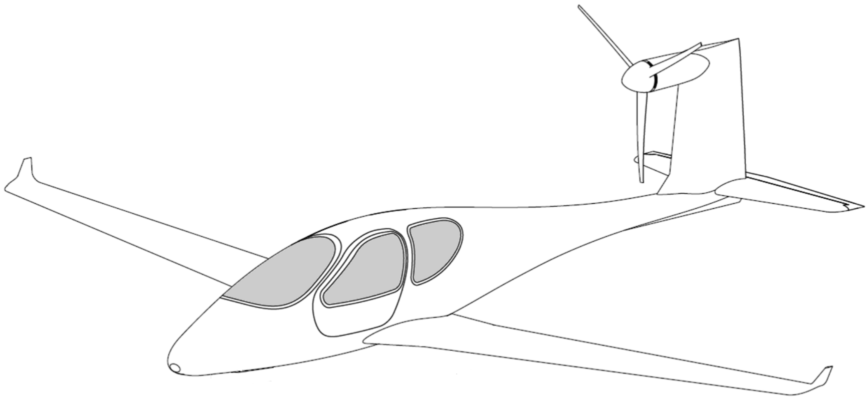

Figure 5.1: Drawing of the preliminary designed hybrid-electric aircraft "Eco4", which was drafted for the Berblinger Competition 2016 by the University of Stuttgart

Parameter	**Value**
Payload	320 kg
Cruise speed	220 km/h
Flight altitude	3,000 m
Range	800 km
Operational reserve	30 minutes
Range after OEI	48 NM (= 89 km)
Wing span	11.63 m
Wing loading	97 kg/m^2
Power loading	96 W/kg

Table 5.1: Data of the investigated transport mission

5.1 Hybrid-electric 4-seat airplane

The following sizing will be carried out for a 4-seat aircraft with a cruise speed of 120 knots (~220 km/h). A visualization of a corresponding preliminary designed hybrid-electric aircraft is shown in Fig. 5.1. In table 5.1 the key data of the investigated transport mission is summarized. The Diamond DA40 NG [95] is chosen as a reference aircraft and is shown in Fig. 5.2 next to the hybrid-electric aircraft. The structure of the DA40 NG is mainly made from fiber reinforced plastics and it possesses an aerodynamically shaped air frame. The model NG of the airplane is equipped with a modern AE-300 diesel engine made by Austro Engines. The engine is equipped with an electronic direct fuel injection and a turbo charger. As described in section 4.1.2 the wing span of the hybrid-electric aircraft is kept constant with respect to the reference aircraft in order to achieve a comparable influence of induced drag and similar handling characteristics. Similarly, the wing and power loading is a fixed design parameter to reach similar flight performances.

5.1.1 Sizing of the propulsion system

As described in section 4.3.1 the independent variables for the preliminary design of the hybrid-electric aircraft can be reduced to the battery power split during take-off S_{TO} and the battery mass fraction ξ_{Bat} if the type and the number of combustion engines is fixed. Consequently, the results of the sizing algorithm can be plotted into a chart with these two variables. S_{TO} reflects which portion of the take-off power is provided by the battery system. The battery fraction ξ_{Bat} expresses the mass of the battery system as a fraction of the maximum take-off mass according to equation 5.1.

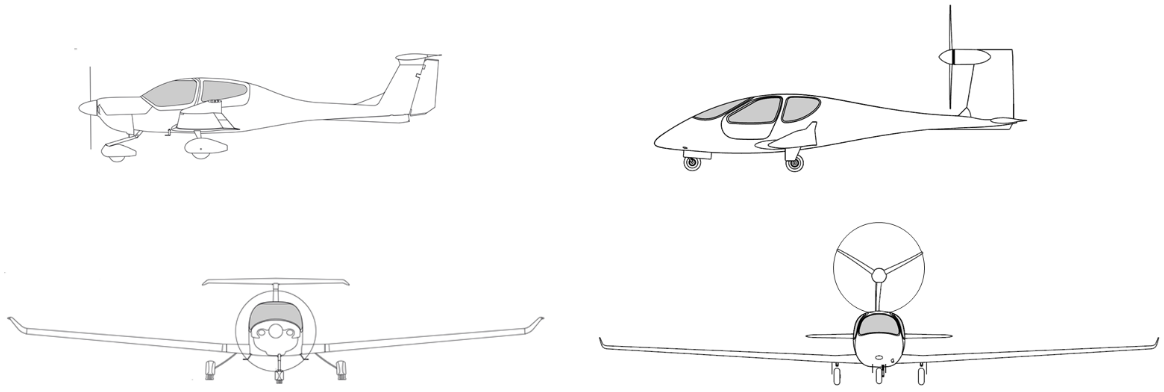

Figure 5.2: Side and front view of a DA40 NG (left) and the preliminary designed hybrid-electric Eco4 (right)

$$S_{TO} = \frac{\eta_{EM} \cdot P_{Bat}}{P_{sh,TO}} \qquad \text{and} \qquad \xi_{Bat} = \frac{m_{Bat}}{m_{MTOM}} \tag{5.1}$$

There are several constraints which limit the design space of S_{TO} and ξ_{Bat} which are plotted in Fig. 5.3. For the battery mass fraction two minimum and one maximum constraint can be deduced. The first minimum constraint, plotted in blue, shows the minimum battery fraction which is needed to provide the battery energy needed for the considered battery power split for take-off and the subsequent flight phases. It can be observed that the magnitude of this constraint raises as the battery power split is increased. The constraint has two discontinuities. Between $S_{TO} = 0$ and the first discontinuity located at about $S_{TO} = 0.52$, battery power is required only during take-off. The required power for climb and cruise flight is provided by the combustion engine. However, if the battery power split is increased further, the combustion engine is only able to provide a fraction of the power required for climb flight. Hence, the battery system needs to provide power in this phase as well and the required battery fraction grows with a steeper gradient. If the battery power split is increased beyond the second discontinuity located at about $S_{TO} = 0.6$, the battery system needs to provide power in cruise flight because the combustion engine power is not sufficient. As a result, the minimum required battery fraction rises with an even steeper gradient. The second minimum constraint, plotted in yellow, reflects the minimum battery fraction which is needed to achieve the required battery power during take-off. It can be observed that in the investigated application, this minimum constraint is located below the minimum constraint for the required battery energy. Hence, this constraint does not limit the design space.

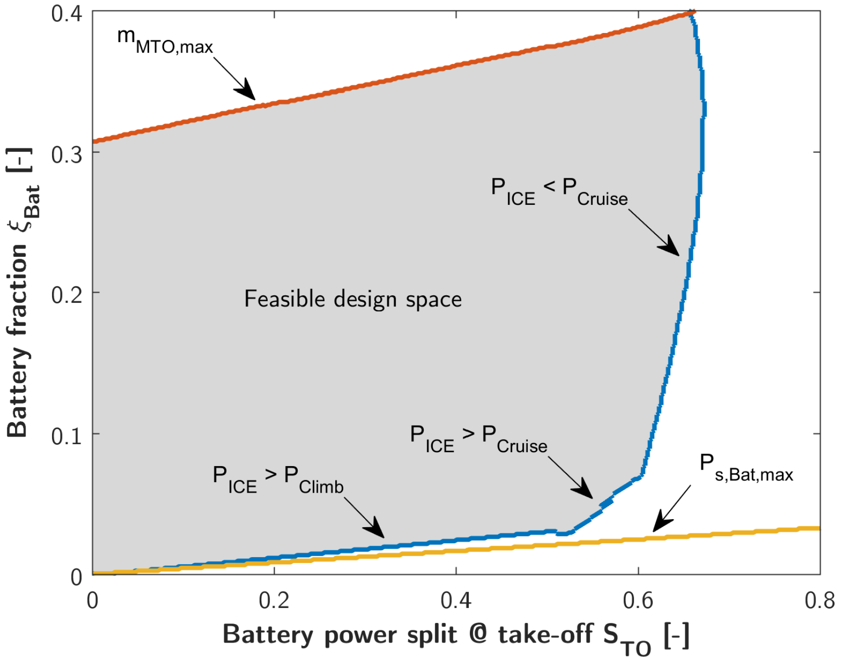

Figure 5.3: Minimum and maximum restrictions of the battery fraction ξ_{Bat} plotted versus the battery power split S_{TO}

In Fig. 5.3 a third constraint is plotted in red which represents the maximum permissible take-off mass applied in the calculation. If the battery fraction would be increased over this restriction, the maximum take-off mass would be required to be higher than the threshold value for the aircraft in order to reach its design range. With the described restrictions, the design space of S_{TO} and ξ_{Bat} is reduced to a feasible design space plotted in grey in Fig. 5.3.

In Fig. 5.4 the same constraints as described in the section above are plotted – however, a requirement regarding a malfunction of the combustion engine is applied. In case of a failure of the combustion engine during take-off, the battery system shall compensate the missing power of the combustion engine as described in section 4.2.6. Additionally, the battery system shall provide sufficient energy for 48 nautical miles of flight range, in order to safely land the aircraft after a combustion engine failure during cruise as deduced in section 4.2.7. As a result, the power and the energy of the battery system has to be increased to be able to fulfill this requirement. Consequently, the constraints for the minimum battery fraction are shifted toward higher battery fractions ξ_{Bat} and reduce the feasible design space. Again, the constraint which represents the minimum battery fraction for the battery power requirement stays below the constraint for the battery energy requirement and does not limit the design space.

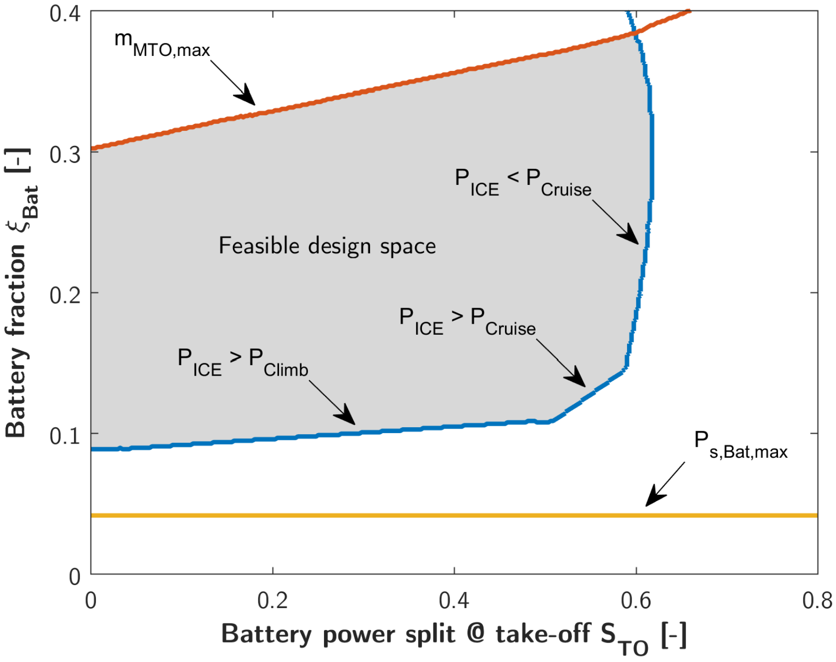

Figure 5.4: Minimum and maximum restrictions of the battery fraction ξ_{Bat} plotted versus the battery power split S_{TO} with sufficient battery energy for a 48 NM flight reserve after a failure of a combustion engine during cruise flight

At a later stage, a second scenario is investigated, where the required reserve flight time after a combustion engine failure during cruise flight is reduced to 10 minutes, which is the minimum VFR-reserve for flights in the vicinity of airfields and the influence of this requirements on the final aircraft will be shown.

In order to identify combinations of S_{TO} and ξ_{Bat} with the lowest fuel consumption, the fuel burn per 100 passenger kilometers is plotted into the remaining design space in Fig. 5.5 and is visualized by a color map. As a further evaluation parameter the resulting maximum take-off mass for each combination of S_{TO} and ξ_{Bat} is calculated and plotted as isolines into the design space. In Fig. 5.5 the results for a hybrid-electric propulsion system are plotted in which a diesel engine is applied as a combustion engine. The optimum with lowest fuel consumption is located at $S_{TO} = 0.50$ and $\xi_{TO} = 0.108$ with a fuel consumption per passenger of 1.40 kg/100 km and a maximum take-off mass of $m_{MTO} = 1449\,\mathrm{kg}$. According to [4], optima found in aircraft design using conventional propulsion are constrained optima, in a sense that the optima is located right at an edge of a constraint. The objective function, in this case the fuel consumption, can only be reduced further if the constraint is violated. Furthermore, [4] describes that in aircraft design with conventional propulsion system, a minimum

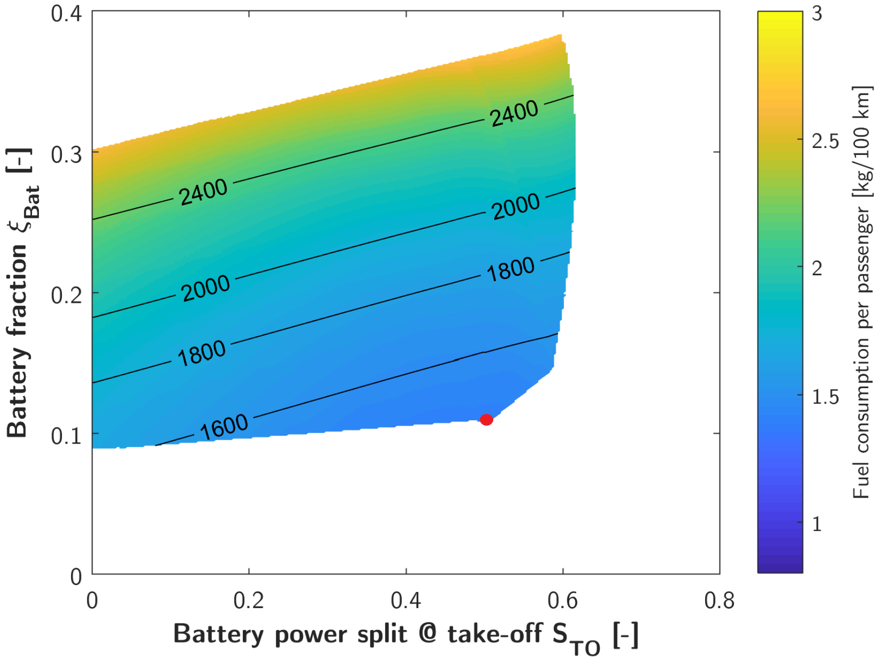

Figure 5.5: Fuel consumption of a diesel hybrid-electric propulsion system plotted versus power split and battery fraction, minimum fuel consumption marked with a red dot

in required fuel is achieved at lowest aircraft mass m_{MTO}. The optima found for the hybrid-electric aircraft in Fig. 5.5 possesses both attributes.

The further scope is to identify the type of combustion engine which is most suitable for the application. In Fig. 5.6 the design diagrams are shown where a diesel engine, a petrol engine and a gas turbine were applied. It can be observed that lower maximum take-off masses of the hybrid-electric aircraft can be achieved when a gas turbine is applied. However, as the overall pressure ratio of the applied gas turbine stays low in the investigated transport mission, the fuel consumption is increased. It can be observed that the lowest fuel consumption of the gas turbine hybrid aircraft is found similarly at a battery power split of $S_{TO} \sim 0.5$. However, the optima can be found at a propulsion system design, where the maximum continuous power of the gas turbine is nearly equal to the required cruise power. As described in section 3.2, the gas turbine is operated therefore approximately at its best efficiency. If the battery power split of S_{TO} is reduced, the gas turbine will be able to deliver higher fraction of the take-off power – however, it will be operated at a part power setting in cruise, which is associated with a decreased efficiency. Hybrid-electric aircraft which use petrol and diesel engines achieve lower fuel consumptions but have an increased maximum take-off mass. The diagram for the petrol-hybrid propulsion system in Fig. 5.6 shows a line of discontinuity

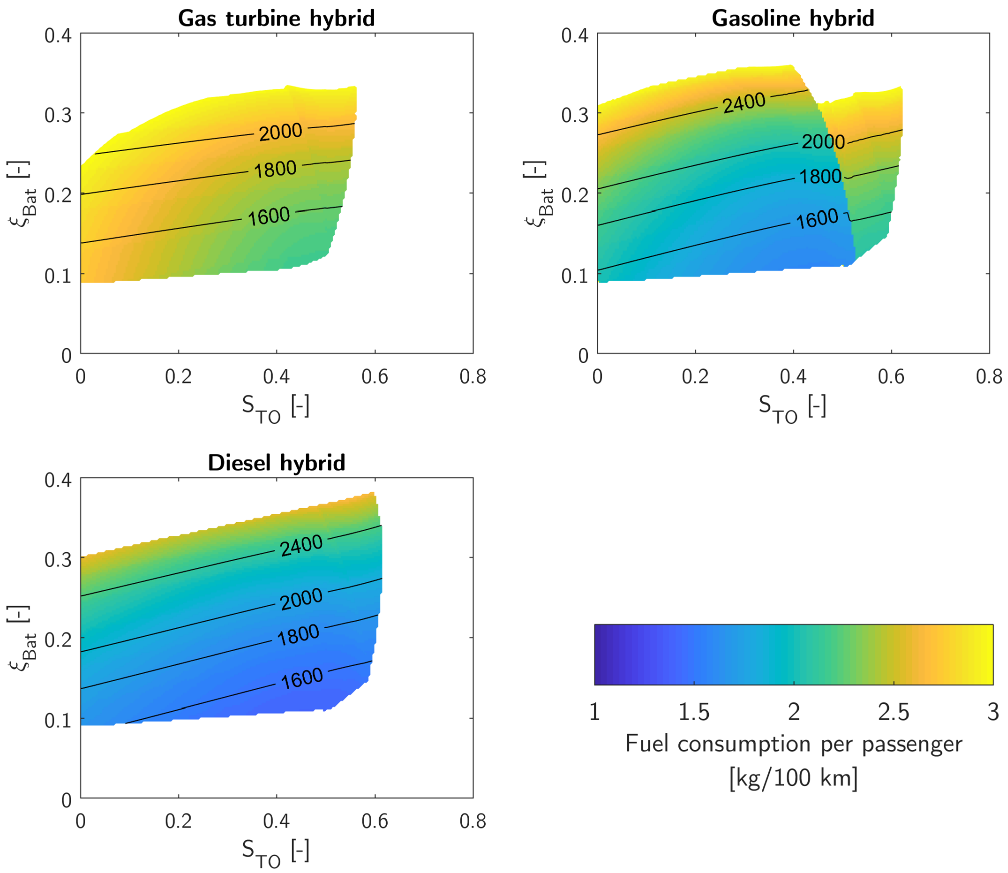

Figure 5.6: Fuel consumption plotted versus power split and battery fraction for hybrid-electric propulsion systems with different combustion engines applied

beginning approximately at $S_{TO} \sim 0.53$ and $\xi_{Bat} = 0.11$. This discontinuity is the result of a gasoline engine which is sized in a way that it is operated in the fuel rich mode in cruise flight. Consequently, the efficiency drops as described in section 3.3.2 and the fuel consumption of the aircraft increases.

5.1.2 Results of optimization

In the design diagram, a combination of S_{TO} and ξ_{Bat} can be found which corresponds to the lowest fuel consumption. As only one global minimum is present in the diagram, a gradient-based optimization algorithm can be applied. The results of the optimized hybrid-electric aircraft for the different types of applied combustion engines are given in Fig. 5.7. Additionally, the data of the conventional reference aircraft, which was designed with the same sizing algorithm, is presented. It can be observed that the maximum take-off mass of the hybrid-electric aircraft is increased compared to the conventional aircraft. In case of the hybrid-electric aircraft using petrol and diesel engines, the increased maximum take-off mass is overcompensated and the resulting fuel consumption is reduced compared to the conventional reference aircraft. This is mainly the result of the increased propeller and integration efficiency and the better aerodynamic shape of the fuselage as described in section 2.3. The product $^{L}/_{D} \cdot \eta_P \cdot \eta_I$ was determined with the methodology described in section 4.1.3. A further factor which contributes to the increased fuel efficiency is the better matching of aerodynamic and engine performance in cruise flight. The latter means that in cruise flight the power required for flying the aircraft at its best glide ratio matches the power where the combustion engine achieves its best efficiency. Typically aircraft of the general aviation do not achieve this match, as the combustion engine is sized for take-off and is oversized for cruise flight as a result. The hybrid-electric aircraft which is equipped with a gas turbine leads in this particular application to the highest fuel consumption. This is a result of the low efficiency of the gas turbine, which is associated with the low overall pressure ratio in this power class.

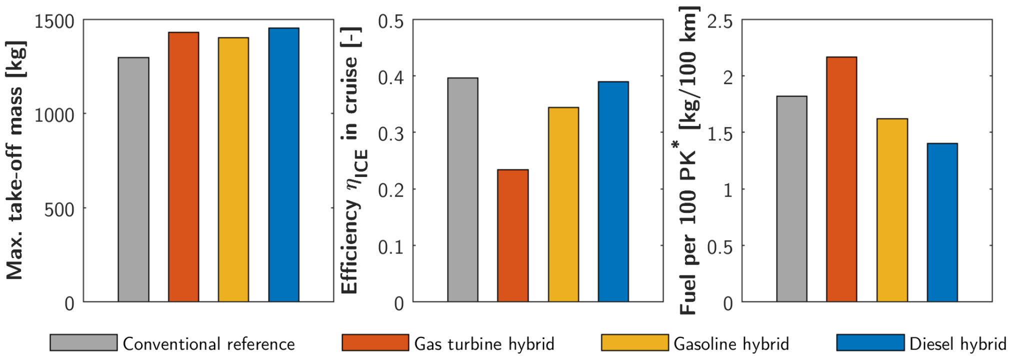

Figure 5.7: Comparison of results for different optimized aircraft: maximum take-off mass, efficiency of the combustion engine in cruise and fuel consumption (* = passenger kilometer)

The mass of the individual components of the aircraft are compared in Fig. 5.8. As expected, the mass of the internal combustion engine lowers as it is not sized to take-off power as in conventional aircraft. However, the overall mass of the propulsion system mass increases as the mass of battery system, electric machines, inverters and power distribution is added. Additionally, the empty mass, which includes the mass of the aircraft's structure and systems, but excludes the propulsion system, is increased for all hybrid-electric aircraft. The empty mass is calculated as described in section 4.1.1 using the component mass data of the Rockwell Commander 112 TCA as the corresponding

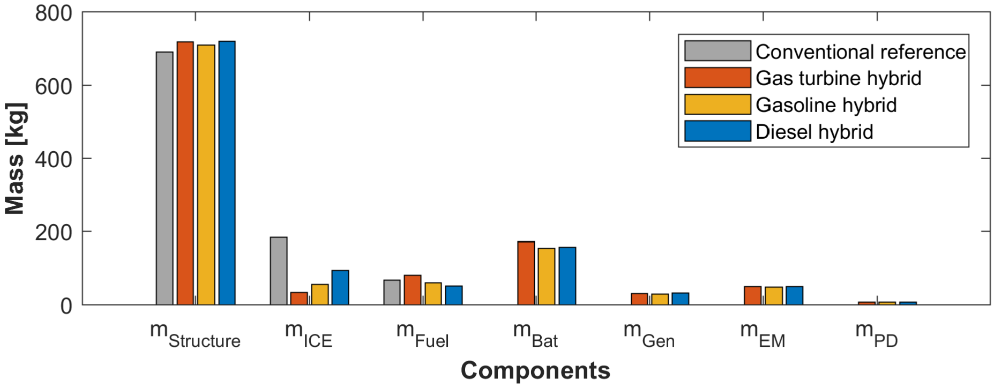

Figure 5.8: Comparison of the component mass of different, optimized hybrid-electric aircraft to the component mass of the conventional reference aircraft

Parameter	DA-40 NG	Hybrid-electric #1	#2
Battery reserve after OEI	-	10 min. (= 37 km)	48 NM (= 89 km)
Applied combustion engine	Diesel	Diesel	Diesel
Maximum take-off mass	1280 kg	1333 kg	1449 kg
Fuel consumption per hour	19.3 l/h	13.6 l/h	15.1 l/h
Fuel consumption per 100 km	8.8 l/100 km	6.2 l/100 km	6.9 l/100 km
Direct CO_2 emissions per passenger	57 gr/km	40 gr/km	45 gr/km
${}^{L}/_{D} \cdot \eta_P \cdot \eta_I$	10.5	18.6	18.2
Efficiency of ICE in cruise	39.5 %	38.7 %	39.0 %
Battery power split S_{TO}	-	0.49	0.50
Battery mass fraction ξ_{Bat}	-	0.064	0.108

Table 5.2: Comparison of the reference aircraft to both hybrid-electric aircraft

mass breakdown of the DA40 NG is not available. The Rockwell Commander 112 TCA is structurally comparable as it features a cantilever low wing, similar certification specification (CS23/FAR23), the same number of passengers, a similar take-off mass, empty mass fraction, type of propulsion system and overall dimensions.

In table 5.2 the results of the propulsion system with optimized S_{TO} and ξ_{Bat} are compared to the data of the reference aircraft DA40 NG. It can be observed that the fuel consumption is reduced, if a diesel engine is applied in the serial hybrid propulsion chain. The main driver for this result are the effects which are associated with the

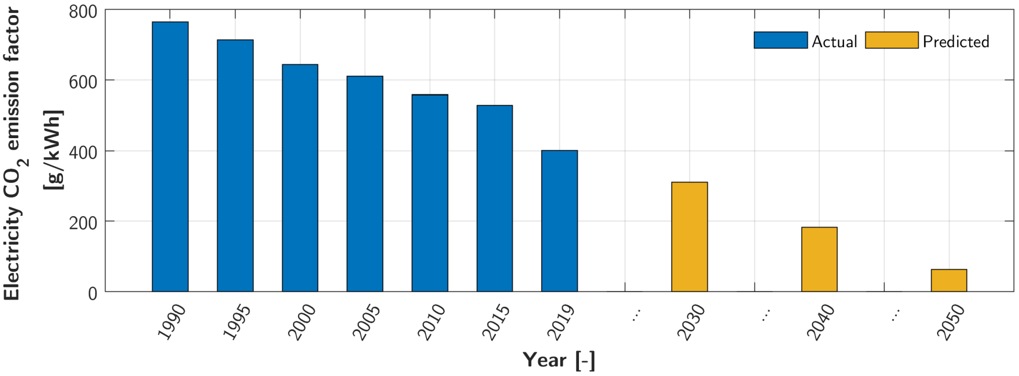

Figure 5.9: Present [99] and predicted [100] CO_2 emission factors of German electricity versus time

electric motor being positioned in the aircraft's empennage as described in section 2.3 and leads e.g. to a significantly increased propeller integration efficiency η_{Int}. The influence of the mass of the additional propulsion components is compensated by this effect even if the battery is sized to carry a power and energy reserve in order to cover a failure of the combustion engine.

Another relevant measure to evaluate an aircraft are the emissions of carbon dioxide (CO_2). Direct CO_2 emissions are the result of burnt fuel – according to [96], diesel contains 270 g/kWh of CO_2, taken the lower heating value as a reference, whereas gasoline and kerosene contain 250 g/kWh and kerosene 260 g/kWh CO_2. To calculate the direct CO_2 emissions, which are referenced to the mechanical energy delivered by the output shaft, the efficiency of the combustion engines needs to be taken into account. Further indirect emissions due to extraction, refining, transport, etc. of the fossil fuel are added to the direct CO_2 emissions. Therefore, primary energy factors [97] of 1.1 for gasoline and 1.2 for diesel are applied [98]. Accordingly, the indirect CO_2 emissions of the generation of electricity have to be included into the evaluation of the hybrid-electric aircraft. In order to quantify this CO_2 emissions, emission factors are used to calculate the mass of emitted CO_2 per used electric energy. In Fig. 5.9 the emission factors of the German electricity are given for different years – the emission factor of the year 2019 is used for the evaluation, which is 47 % lower than the value of the year 1990, but 29 % higher than the expected value in the year 2030.

In Fig. 5.10 the CO_2 emissions of the hybrid-electric aircraft as well as the reference aircraft is shown in a stacked bar plot. The reduced portion of the CO_2 emissions contributed by the electric energy shows that the influence of the electric energy has very limited influence on the optimized design of the hybrid-electric aircraft with the requirements given in table 5.1. This can be confirmed by comparing the plot of the

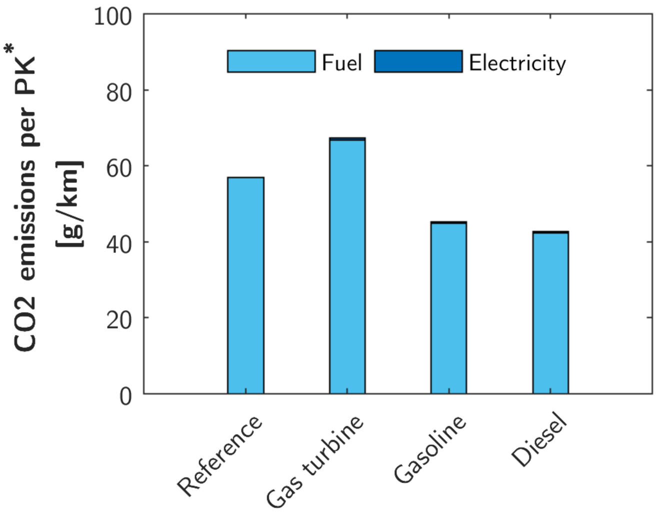

Figure 5.10: Total emissions of CO_2 for different optimized hybrid-electric aircraft including the CO_2 generated by used electricity (* = passenger kilometer)

CO_2 emissions in Fig. A.6 to the plot of the fuel consumption in Fig. 5.6, which possess a high degree of similarity. However, if the evaluation range is lowered from the maximum range of 800 km to 200 km, the lowest CO_2 emissions are achieved for a higher battery mass fraction which is associated with a significantly increased maximum take-off mass as shown in Fig. A.7.

5.1.3 Sensitivity analysis

In this section the impact of hypothetical technology improvements of the components onto the fuel consumption and the maximum take-off mass of the aircraft is investigated. This sensitivity analysis is done by varying the component parameters which are inputs to the aircraft design optimization and comparing the resulting fuel consumption and the maximum take-off to the results with the established reference technology level of the components described in section 3.

The influence of an improvement of the following component parameters was investigated: the specific power $P_{s,EM}$ and the efficiency η_{EM} of electric machines – η_{EM} includes in this consideration the efficiency of the inverter. Furthermore, the specific power $P_{s,ICE}$ and the efficiency of diesel engines η_{ICE} as well as the impact of an improved specific energy $E_{s,Bat}$ and an improved maximum specific power $P_{s,Bat,max}$ of the battery cells is evaluated. In Fig. 5.11 the influence of an 1 % improvement of the component parameters is correlated to the resulting reduction in aircraft fuel burn and aircraft mass. It can be observed that an 1 % improvement of the efficiency

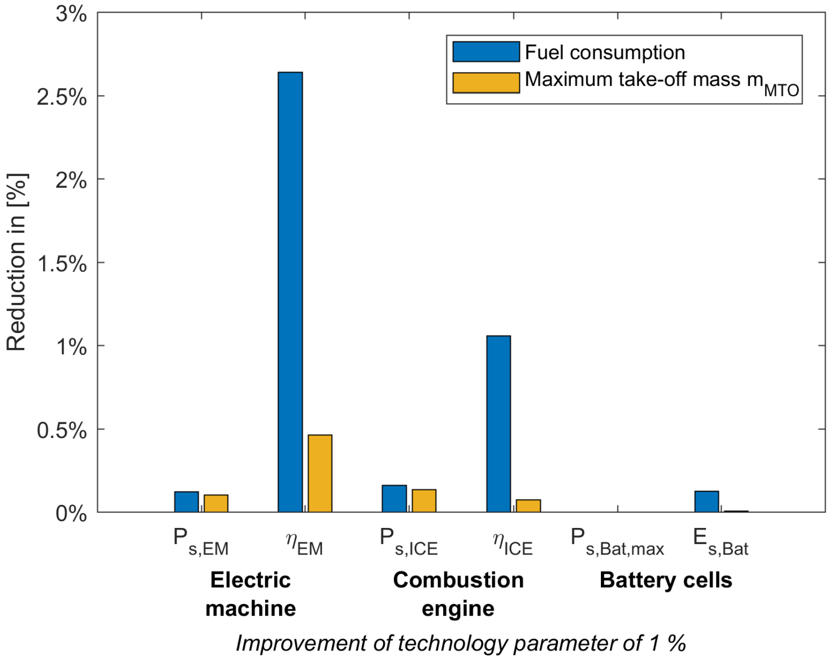

Figure 5.11: Impact of technology improvements onto fuel burn and MTOM

of the combustion engine η_{ICE} reduces the fuel burn similarly by 1.06 %. The slight over-proportional improvement is the result of a typical snowball effect in aircraft design. In this case, the increased combustion engine efficiency leads to a slightly lighter aircraft as less fuel mass is required, which again reduces the fuel burn. Furthermore, it can be observed that a 1 % improvement of the efficiency of the electric machines η_{EM} influences the resulting fuel burn by 2.6 %. The significant impact of η_{EM} can be explained with the presence of two electrical machines in the serial hybrid-electric propulsion architecture. Further, an increased efficiency η_{EM} leads to lighter electric machines as less electric power is required in order to achieve the same shaft power for the propeller. Although an improvement of the efficiency of the electric machine has a significant impact onto the fuel consumption of the aircraft, its realization is challenging as an 1 % improvement, which is referenced to the value $\eta_{EM} = 0.938$, would lead to an efficiency of $\eta_{EM} \sim 0.947$. This would imply that the losses of the electric machine and its inverter are lowered by 15 %.

The mass specific energy of battery cells depends on the applied mass specific power as discussed in section 3.4. The improvement of the specific energy of the battery cells is therefore modelled as a shift of the envelope of both parameters in the Ragone plot as shown in Fig. 5.12. It can be observed that a 1 % improvement in specific energy of battery cells results in merely 0.1 % fuel burn reduction. The low numeric

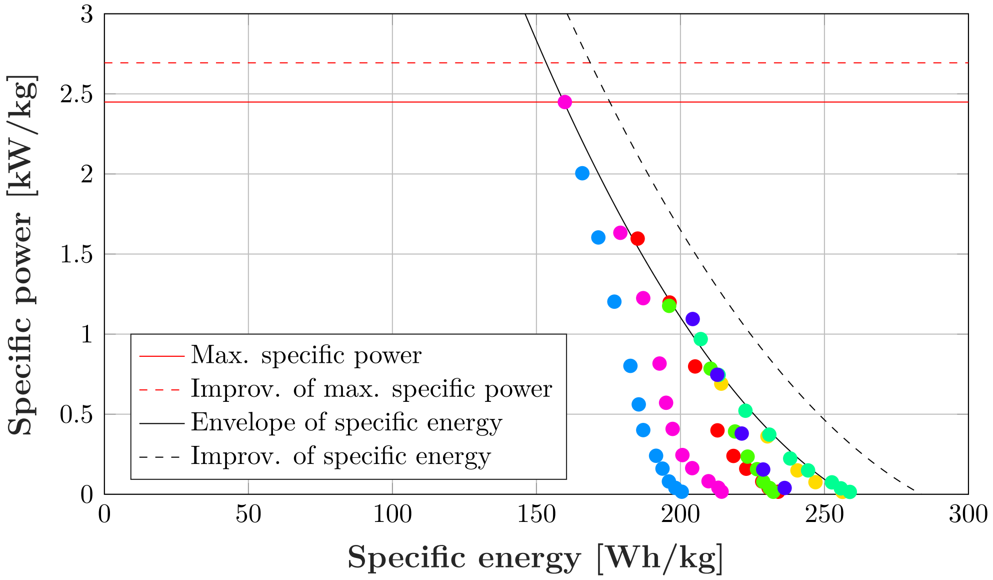

Figure 5.12: Visualization of an improvement in battery cell technology in the Ragone plot

influence of an improvement of the specific energy of the battery cells is plausible, as the battery system contributes about 10 % to the overall aircraft mass – as a result, a 1 % reduction in system mass leads to a mass reduction of 0.1 % on aircraft level. This lowers consequently the fuel consumption by about 0.1 %. In a second scenario, a pure improvement of the maximum specific power of the battery cells is investigated, which extends the envelope in Fig. 5.12 to higher values for the specific power. This technology improvement has no influence on aircraft fuel burn or aircraft mass, as the battery cell applied in the optimized hybrid-electric aircraft possesses a maximum specific power of ∼1.4 kW/kg.

The gathered data can be used to evaluate component design parameters, which can be in conflict to each other. E.g. in the development of an electric machine a point in the design may be reached where either the mass-specific power or the efficiency can be improved. Which of the parameters shall be pursued in order to achieve the lowest fuel consumption on aircraft level can be identified with the present data. The inverse of the percentage shown in Fig. 5.11 can be calculated, resulting in a required improvement of the component parameter, which is needed to realize a reduction of

1 % in fuel burn. In table 5.3 these percentages are summarized. It can be deduced that if an improvement of 0.4 % in efficiency of the electric machine would result in a deterioration of 8.0 % of its mass specific power, no gain in fuel burn would be reached on aircraft level. This specific point is called Pareto optima. If, however, the deterioration in specific power would be lower than 8.0 %, the aircraft fuel burn would benefit, even though the specific power would have been decreased, resulting in a heavier electric machine.

Component	**Design variable**	**Reference value**	**Req. improvement for 1 % reduction in fuel burn**
Electric machine	$P_{s,EM}$	2.34 kW/kg	8.0 %
	η_{EM}	0.938	0.4 %
Combustion engine	$P_{s,ICE}$	0.72 kW/kg	6.2 %
	η_{ICE}	0.39	0.9 %
Battery system	$P_{s,Bat,max}$	2.449 kW/kg	Inf
	$E_{s,Bat}$	233 Wh/kg	7.8 %

Table 5.3: Trade-off for component design parameters

5.2 Hybrid-electric 9-seat airplane

The application of a hybrid-electric propulsion system to an airplane, which is designed to carry nine passengers and possesses a cruise speed of 220 knots ($\sim 400\,\text{km/h}$) with a range of 3,200 km, is investigated in the following section. The PC-12 NG made by Pilatus, shown in Fig. 5.13, is chosen as a modern reference aircraft. The PC-12 NG is equipped with the turbo-prop engine PT6A-67B made by Pratt & Whitney Canada. Its maximum shaft power rating is 895 kW and its efficiency is $\eta_{GT} = 0.25$ at sea level [101]. At a flight altitude of 30,000 ft this efficiency increases to $\eta_{GT} = 0.28$ according to [41].

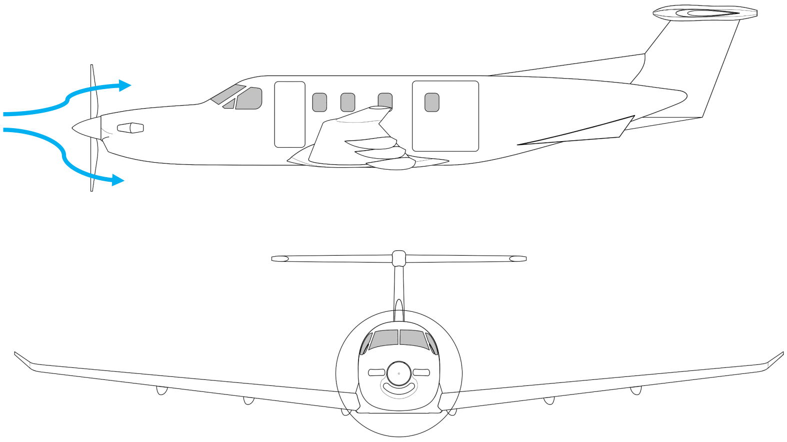

Figure 5.13: Side view and front view of the reference aircraft

For similar reasons as described in chapter 2, the turbo-prop engine has to be installed in the front of the pilots as shown in Fig. 5.13 and the same aerodynamic disadvantages are associated with this aircraft configuration. In order to quantify the effects, the product of glide ratio $^{L}/_{D}$, propeller efficiency η_P and integration efficiency η_I is calculated, using the data listed in table B.11. Therefore, the equation of the required shaft power is transformed for the parameter of the specific air range, which is given in the flight manual of the PC-12 NG [102]. To achieve this, the cruise speed is replaced by the quotient of flown distance in horizontal flight and flight time. With the resulting equation 5.2, the product $^{L}/_{D} \cdot \eta_P \cdot \eta_I$ of the PC-12 NG can be determined to be 11.7 in its most efficient cruise flight. The magnitude of this value is similar to other conventional single engine aircraft. A vision of a hybrid-electric aircraft with an optimized fuselage is presented in Fig. 5.14.

$$^{L}/_{D} \cdot \eta_P \cdot \eta_I = \frac{\Delta R}{\Delta m_{Fuel}} \cdot \frac{m_{A/C,Cruise} \cdot g}{\eta_{ICE} \cdot E_{s,Fuel}} \tag{5.2}$$

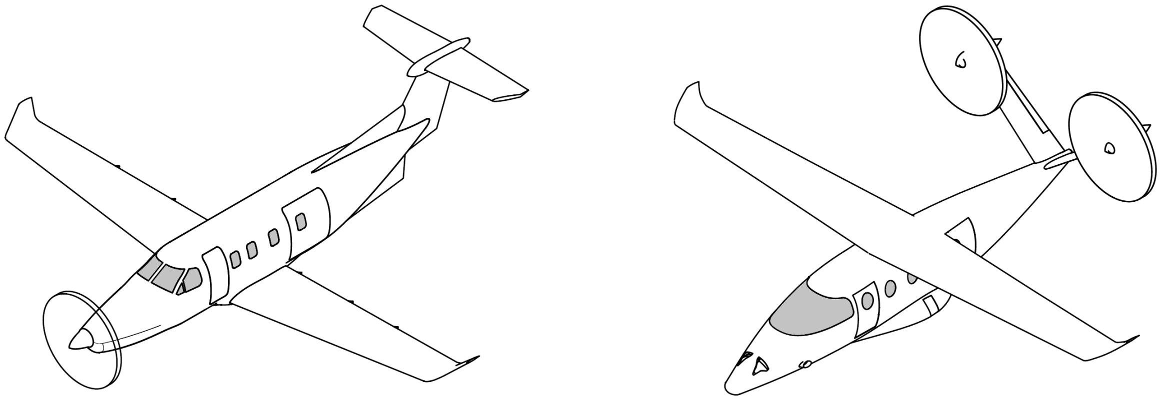

Figure 5.14: View of a multi-purpose airplane similar to the PC-12 NG (left), vision of an optimized aircraft "HyBird Mod" propelled by a hybrid-electric propulsion system (right) [103]

In this section the number of combustion engines will be introduced as a further design parameter. In particular, it will be investigated if a single combustion engine configuration or a twin engine configuration is more suitable to reduce fuel consumption. In table 5.4 the parameters of the investigated flight mission are summarized, where it can be observed that payload, cruise speed and range are increased significantly compared to the investigated 4-seat aircraft. As described in section 4.1.2, the wing span, the wing loading and the power loading on aircraft level is kept constant in order to achieve comparable flight performance, induced drag and handling characteristics. The energy reserve required after a failure of a combustion engine during cruise flight is 48 nautical miles of flight range. The range is similar to the 4-seat aircraft described in section 5.1 because the same landing field length is required – furthermore, the safety margin is similar: on the one hand, the range for the detection of the malfunction is increased due to the higher cruise speed. On the other hand, the unfavorable influence of head wind is decreased in the same order of magnitude. Similarly to the 4-seat aircraft, the battery can compensate the power loss of a failed combustion engine during take-off.

Two variations of the transport missions will be investigated: in the first scenario the aircraft will be equipped with a gas turbine and will be operated at a cruise altitude of 9,000 m. In the second scenario the aircraft possesses a piston engine and its cruise altitude will be reduced to 3,000 m. The reason for this variation is that the efficiency

Parameter	**Value**
Payload	810 kg
Cruise speed	407 km/h
Flight altitude	3,000 m or 9,000 m
Range	3,200 km
Operational reserves	Distance to alternate airport + 45 minutes
Range after OEI	48 NM (= 89 km)
Wing span	16.28 m
Wing loading	184 kg/m^2
Power loading	189 W/kg

Table 5.4: Data of the investigated transport mission

of gas turbines increases with increasing flight altitude, which is not the case for the investigated piston engines. The power of piston engines simply decreases above the "critical altitude" as described in section 3. In order to achieve a fair comparison for both types of combustion engines, the cruise altitude is varied according to the applied combustion engines.

5.2.1 Sizing of the propulsion system

In the following consideration a propulsion system with one gas turbine is compared to a system with two gas turbines. The hybrid-electric system which possesses one gas turbine is equipped with a larger battery system as this needs to cover all required energy and power reserves in case of a combustion engine failure. As a result, the required battery mass fraction increases. However, the efficiency of the gas turbine is increased as it possesses a higher rated power as described in section 3.2. Similarly as in section 5.1.1 the fuel consumption is plotted over battery power split S_{TO} and battery mass fraction ξ_{Bat} as shown in Fig. 5.15. It can be observed that in this specific design case, the aircraft equipped with two gas turbines possesses an slightly, increased fuel consumption. The situation is reversed if an increased diversion range after a failure of a combustion engine is required as the effects almost balance each other.

In Fig. 5.16 the fuel consumption is plotted over battery power split S_{TO} and the battery mass fraction ξ_{Bat} for three different propulsion systems, which are all equipped with piston engines. It can be observed that the fuel consumption for the aircraft equipped with a gasoline engine is higher than the fuel consumption of the hybrid-electric aircraft equipped with a diesel engine. In this specific case, the increased

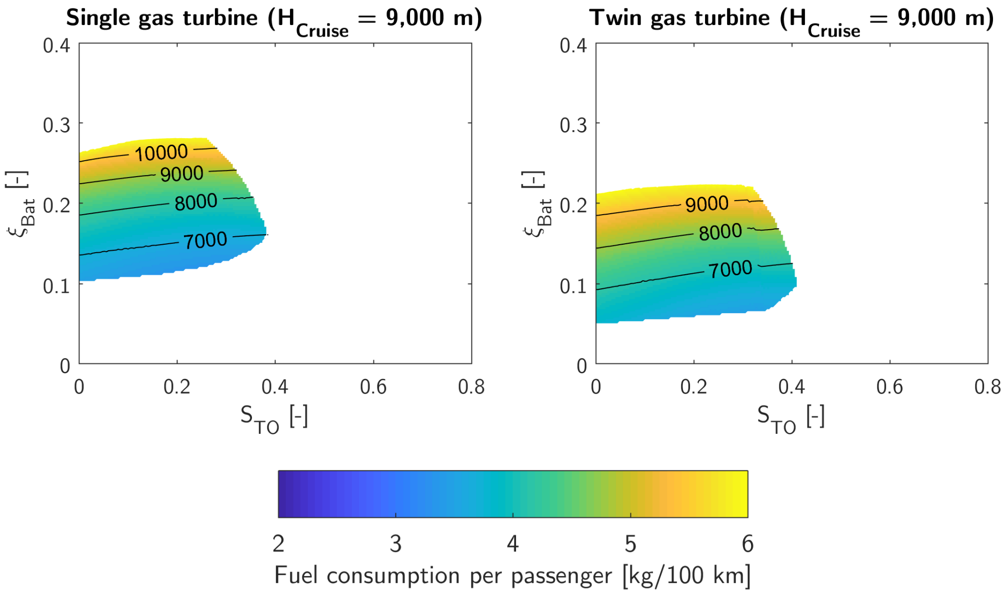

Figure 5.15: Fuel consumption plotted versus power split and battery fraction for a hybrid-electric propulsion system equipped with a single gas turbine (left) and a twin gas turbine system (right)

efficiency of the diesel engine compensates its increased relative weight and achieves a lower fuel consumption on aircraft level. In the last plot, a specific combustion engine called "High Power Density Engine" (HPDE) is applied, which is currently under development by the company Safran S.A. as described in section 3.3.1. With this type of combustion engine the lowest fuel consumption is achieved in the investigated transport mission.

All hybrid-electric propulsion systems, which are shown in Fig. 5.16, are equipped with two piston engines as no advantage in efficiency results from an increased power rating of the engine – in contrast to the efficiency of gas turbines. Hybrid-electric propulsion systems with only one piston engine result in a higher required battery mass fraction ξ_{Bat} which increases consequently the maximum take-off mass and increases the fuel consumption.

5.2.2 Results of optimization

With an optimization algorithm the combination of S_{TO} and ξ_{Bat} with the lowest fuel consumption is identified for the different types of combustion engines. The results of the hybrid-electric propulsion systems with the lowest fuel consumption for each

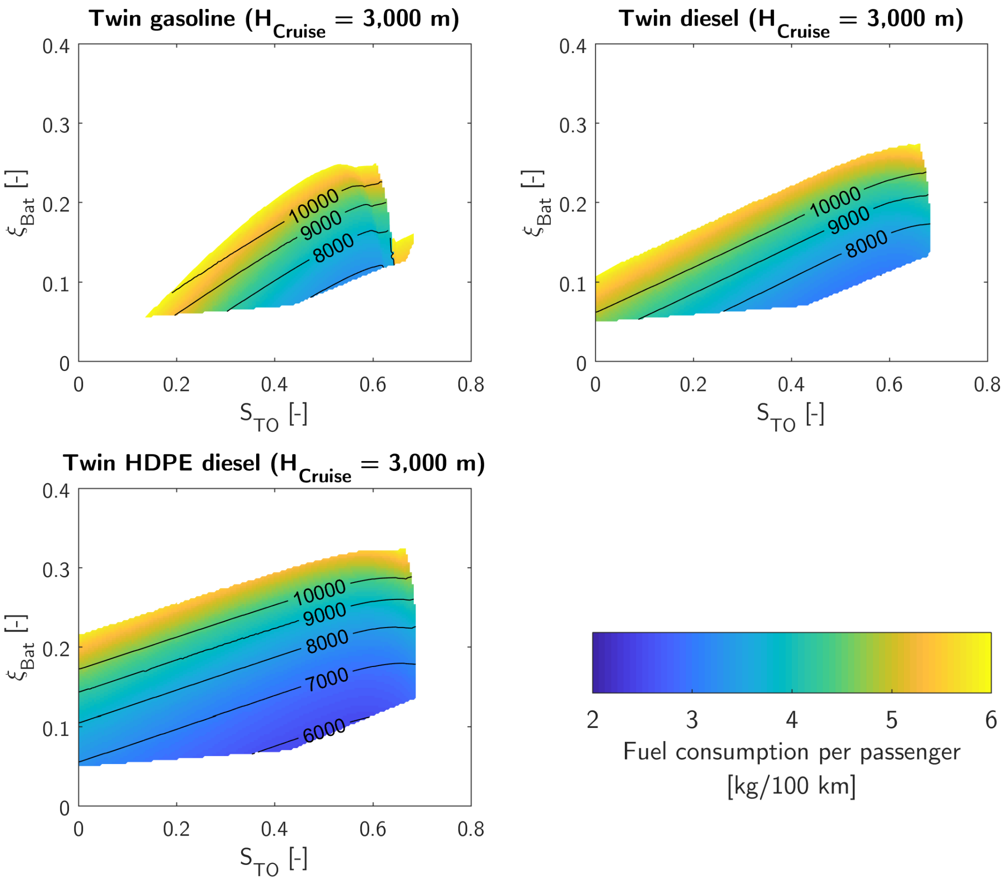

Figure 5.16: Fuel consumption plotted versus power split and battery fraction for a gasoline, diesel and HPDE diesel hybrid-electric propulsion system

type of combustion engine is presented. In case of the gas turbine, the aircraft is equipped with only one combustion engine – in case of the piston engines, the aircraft are equipped with two engines. In Fig. 5.17 the resulting maximum take-off mass, the efficiency of the applied combustion engine in cruise flight and the resulting fuel consumption per 100 km and passenger are summarized. Additionally, the data of the re-calculated reference aircraft is given, which was obtained by the same calculation in order to ensure plausibility. It can be observed that only the fuel consumption of the hybrid-electric aircraft which are equipped with a conventional diesel engine and a HPDE diesel engine achieve a lower fuel consumption than the conventionally propelled PC-12 NG. The reason why the hybrid-electric aircraft, which is powered by a gas turbine, does not possess a reduced fuel consumption is that the beneficial effect of the optimized, electrically powered fuselage is compensated by the increased mass of the

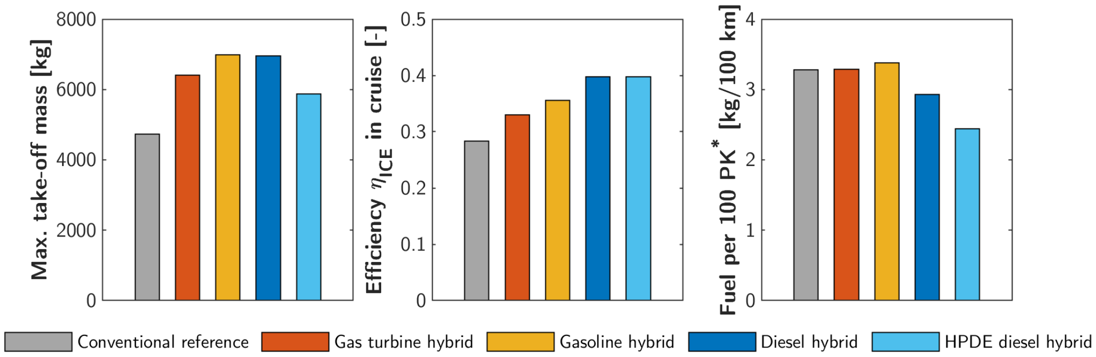

Figure 5.17: Comparison of maximum take-off mass, efficiency of the combustion engine in cruise and fuel consumption (* = passenger kilometer)

hybrid-electric propulsion system, which is associated with further mass growth of the aircraft structure as described in section 4.1.1. The mass of the hybrid-electric aircraft, which is equipped with gasoline engines, is increased even more, which compensates the increased efficiency of the applied piston engines. Only the hybrid-electric aircraft equipped with the diesel engines increase the aircraft mass in a way that the adverse weight growth is compensated by the increased efficiency of the combustion engine and the beneficial effect of the optimized shape of the fuselage.

In Fig. 5.18 a detailed mass breakdown of the different hybrid-electric propulsion systems is given together with the data of the conventional reference aircraft. It can be observed, how the hybrid-electric aircraft equipped with a conventional diesel engine possesses the highest mass of the combustion engine m_{ICE}. Consequently, the structural empty mass $m_{Structure}$, which does not include the mass of the propulsion system, is increased as well as described in section 4.1.1. Contrary, the hybrid-electric aircraft equipped with a single gas turbine possesses the lightest combustion engine but is equipped with the heaviest battery system m_{Bat} as this has to provide the full power and energy reserves in case of a failure of the combustion engine. The lowest structural empty mass is achieved by the hybrid-electric aircraft, which is equipped with the mass-optimized HPDE diesel engine, as it combines a low mass of the combustion engine with a low required fuel mass. It can be further observed, how the mass contribution of the power distribution system m_{PD}, which is investigated in section 3.6, is in the order of magnitude of the generator mass and cannot be neglected.

In table 5.5 the data of the reference aircraft is compared to the data of the two hybrid-electric aircraft with lowest fuel consumption. These are equipped with conventional diesel engines and HPDE diesel engines. It can be observed, how an increased take-off mass is overcompensated by an increased efficiency of the combustion engine in

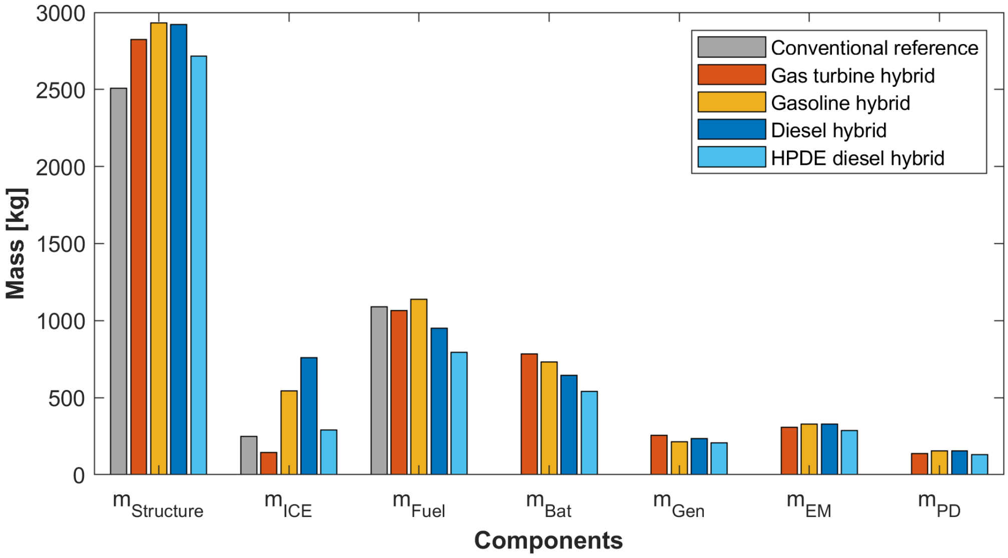

Figure 5.18: Comparison of the mass of the aircraft components (EM = electric motor, PD = power distribution)

cruise flight and an increased product of glide ratio, propeller and propeller integration efficiency $L/D \cdot \eta_P \cdot \eta_I$. Consequently, a reduction in fuel burn of 9 % and 24 % can be achieved for the hybrid-electric aircraft. Similarly, the direct CO_2 emissions of the hybrid-electric aircraft are reduced.

5.2.3 Sensitivity analysis

In Fig. 5.19 the results for the sensitivity analysis of the hybrid-electric aircraft, which is equipped with a HPDE diesel, is summarized. Similar as in the sensitivity analysis carried out for the 4-seat aircraft in section 5.1.3, the influence of an improved efficiency of the electric machine is magnified in the serial hybrid-electric propulsion system and an efficiency improvement of 1 % leads to an reduction of 2.8 % in fuel burn. An 1 % increase in efficiency of the combustion engine translates into a reduction in fuel consumption of 1.2 %. The slight over proportional reduction is the result of the resulting reduced maximum take-off mass of the aircraft as less fuel is required. According to the results, the influence of an 1 % increase in specific energy of the battery cells results to a merely reduced fuel burn. A purely increased specific power of the battery cells as shown in Fig. 5.12 does not lead to a fuel burn reduction.

In table 5.6 the inverse values of the sensitivities are given. The values can be used to evaluate trade-offs between different component parameters. E.g. if a derivative development of an electric machine results in 0.3 % improvement in efficiency η_{EM} but

Parameter	**PC-12 NG**	**Hybrid-electric**	
		#1	**#2**
Applied combustion engine	Gas turbine	Diesel	HPDE diesel
Number of combustion engines	1	2	2
Maximum take-off mass	4726 kg	7001 kg	5892 kg
Mean fuel flow in mission	109 kg/h	100 kg/h	83 kg/h
Direct CO_2 emissions per passenger	104 g/km	95 g/km	79 g/km
$L/D \cdot \eta_P \cdot \eta_I$	11.6	16.0	16.1
Efficiency of ICE in cruise	28.3 %	39.7 %	39.7 %
Battery power split at take-off S_{TO}	-	0.55	0.51
Battery mass fraction ξ_{Bat}	-	0.010	0.089

Table 5.5: Comparison of the reference aircraft to optimized hybrid-electric aircraft equipped either with conventional diesel engines or mass optimized HPDE diesel engines

at the same time decreases its specific power $P_{s,EM}$ by 5.2 %, no advantage on aircraft level would be given. In Fig. A.8 and table B.12 the results are given for the sensitivity analysis for the hybrid-electric aircraft, which is equipped with a conventional diesel engine.

Component	**Design variable**	**Reference value**	**Req. improvement for 1 % reduction in fuel burn**
Electric machine	$P_{s,EM}$	3.84 kW/kg	5.4%
	η_{EM}	0.94	0.4 %
Combustion engine	$P_{s,ICE}$	2.00 kW/kg	8.1%
	η_{ICE}	0.39	0.8 %
Battery system	$P_{s,Bat,max}$	2.449 kW/kg	Inf
	$E_{s,Bat}$	216 Wh/kg	39.3 %

Table 5.6: Trade-off for component design parameters for a hybrid-electric aircraft with installed HDPE diesel engines

5.2.4 Influence of a single engine operation of a twin engine aircraft

In the following section, the possible advantage of a hybrid-electric aircraft is investigated, which is equipped with two gas turbines but turns off one gas turbine in cruise

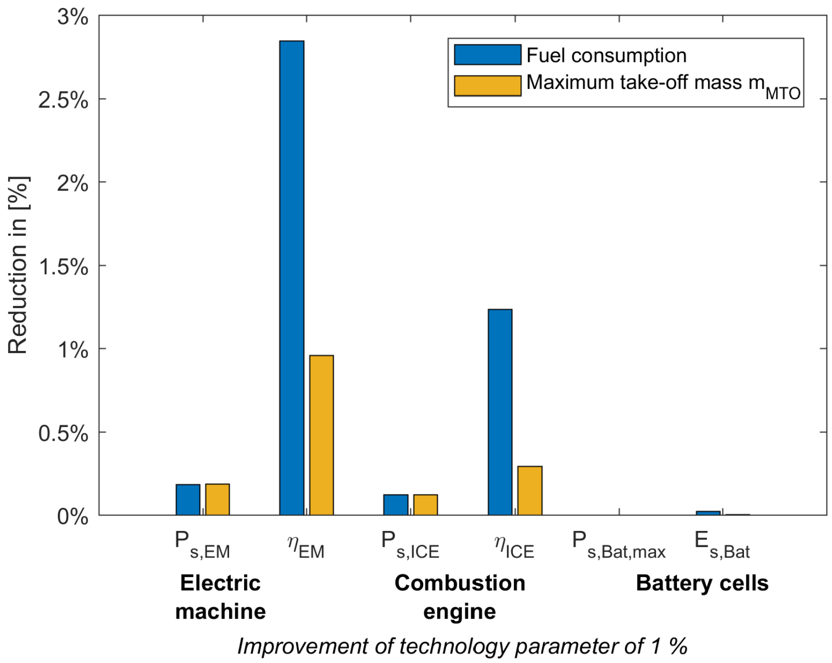

Figure 5.19: Impact of technology improvements onto fuel burn and MTOM of a hybrid-electric aircraft with installed HDPE diesel engines

flight in order to increase the efficiency of the remaining gas turbine in operation – a practice which is currently not done in aviation. In the operation of a conventional aircraft with two combustion engines, a shut-down of one engine would result in an unsymmetrical thrust which would have to be compensated by control surfaces leading to higher trim drag. In addition, an in-flight restart of a combustion engine is not considered to be part of a reliable normal operation strategy. As a result, the combustion engines operate during the entire flight of a conventional aircraft. Contrary, in a serial hybrid-electric propulsion system, the shutdown of one combustion engine does not lead to unsymmetrical thrust. Furthermore, an in-flight restart of a combustion engine coupled to a generator might be regarded similar to an in-flight restart of a auxiliary power unit (APU) of a conventional aircraft, which is common practice in the operation of conventional airliners. As a result, a scenario will be investigated where an in-flight shutdown of one of the gas turbines in cruise flight is part of the normal operation strategy of the twin-engine hybrid-electric aircraft. This can be beneficial as the efficiency of two gas turbines running at e.g. 40 % power setting is lower than the efficiency of one gas turbine, which is operated at 80 % power setting as shown in Fig. 5.20.

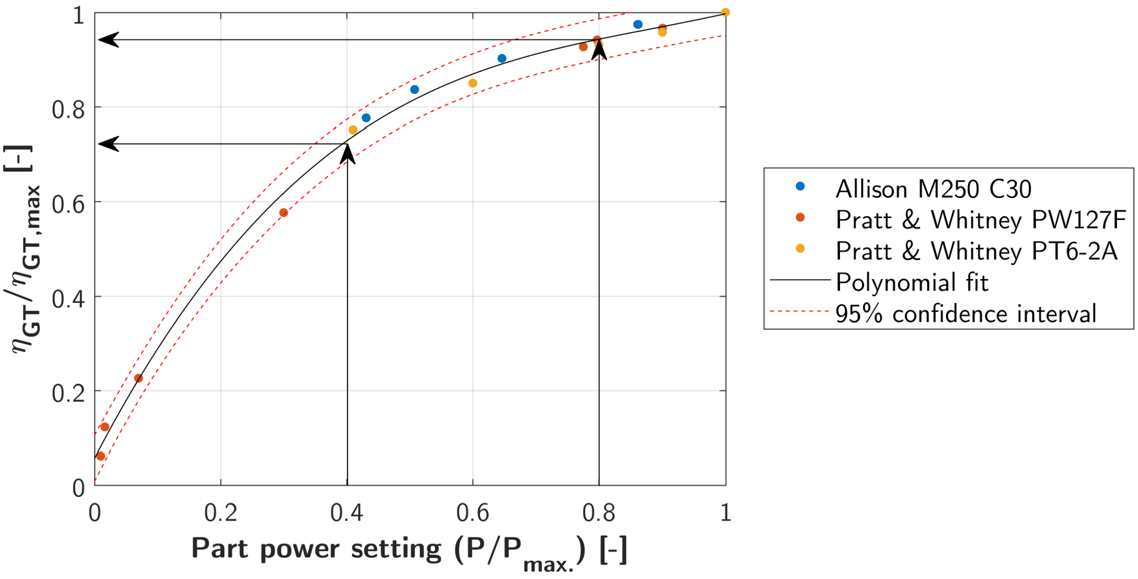

Figure 5.20: Influence of two part power settings onto the efficiency of a gas turbine

When investigating a hybrid-electric propulsion system with two gas turbines for a cruise altitude of 9,000 m, no in-flight shutdown of one of the gas turbines is feasible. The reason is that the power of the gas turbines is decreased significantly due to the increased cruise altitude. As a result, both gas turbines are needed in order to provide power for the cruise flight. However, if a hybrid-electric aircraft with a non-pressurized fuselage, similar to the Dornier Do-228 NG, is investigated, an in-flight shutdown of one gas turbine becomes feasible. Due to the non-pressurized fuselage, the cruise altitude is reduced to 3,000 m. As a result, the remaining power of a single gas turbine is sufficient for cruise flight.

In Fig. 5.21 the difference in the fuel consumption plot can be assessed. In the first plot, the hybrid-electric aircraft was equipped with a single gas turbine – the results are given as a reference. In the second plot, the aircraft is equipped with two gas turbines, however, the option of the engine shutdown was deactivated. In the last plot, a shutdown is considered by the algorithm. Consequently, if the required power can be generated by a single gas turbine, the remaining engine was shutdown in cruise flight. In this plot a new, additional design space is created in which a lower fuel consumption and a lower take-off mass can be achieved. This is a result of the increased efficiency of the remaining gas turbine in cruise flight and its associated beneficial effect of e.g. reduced fuel mass and reduced structural mass as described in section 4.3.1. However, when comparing the plot of the fuel consumption to the plot of the hybrid-electric propulsion system which is equipped with a single gas turbine but a cruise altitude of

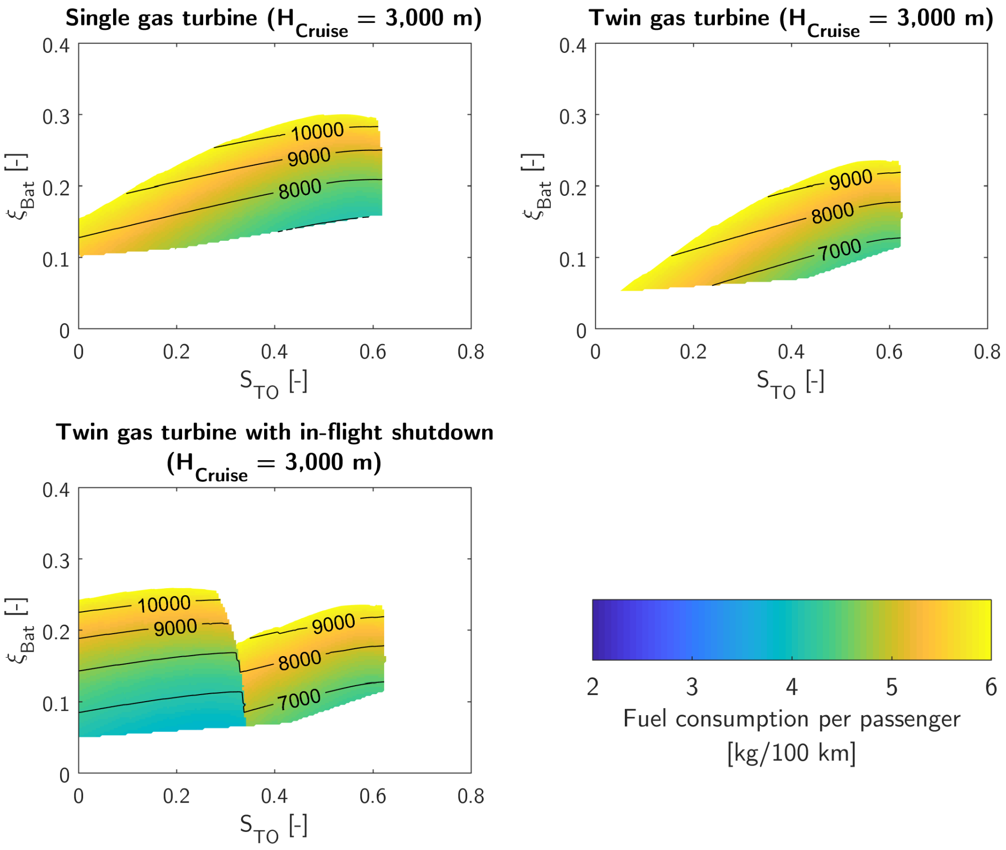

Figure 5.21: Influence of an in-flight shutdown of one gas turbine depending of the flight altitude of the transport mission

9,000 m, it can be observed that this aircraft achieves a lower fuel consumption than all aircraft operated at 3,000 m. This is the result of the beneficial effect of flight altitude on the efficiency of a gas turbine. For reference, the results of the optimized propulsion systems are summarized in table 5.7.

Parameter	**Hybrid-electric**		
	#1	**#2**	**#3**
Applied combustion engine	Gas turbine	Gas turbines	Gas turbines with shutdown
Number of combustion engines	1	2	2
Maximum take-off mass	7126 kg	6734 kg	6293 kg
Mean fuel flow in mission	140 kg/h	145 kg/h	127 kg/h
Direct CO_2 emissions in cruise per passenger	134 gr/km	139 gr/km	121 gr/km
$^{L}/_{D} \cdot \eta_P \cdot \eta_I$	15.8	15.8	15.9
Efficiency of ICE in cruise	28.3 %	25.4 %	27.2 %
Battery power split at take-off S_{TO}	0.54	0.56	0.24
Battery mass fraction ξ_{Bat}	0.160	0.104	0.059

Table 5.7: Comparison of hybrid-electric aircraft, which are equipped with gas turbines and are operated at a cruise altitude of 3,000 m. Hybrid-electric aircraft #3 is able to shut down one gas turbine in cruise flight to increase the efficiency of the remaining engine

Chapter 6

Conclusion

The investigated series hybrid-electric aircraft show a potential to possess a reduced fuel consumption compared to modern reference aircraft. Optimized propulsion systems were obtained by a sizing program, implemented in MATLAB, which incorporates the scaling laws of the propulsion components as well as the influence of an increased propulsion system mass on aerodynamic drag and required structural mass. Scaling laws for power, efficiency, mass and altitude characteristics of the components of the propulsion system were derived from modern, existing components. The masses of auxiliary systems, which are needed to operate the hybrid-electric propulsion system were taken into account as well: e.g. cooling systems for electric machines, appropriate cables and relays for the distribution of electric power. Additionally, an integration factor and a capacity fade factor for battery cells were included in the sizing of the propulsion system. Lastly, a mass-optimized diesel engine, which is currently being developed by the company Safran S.A., was used as a technology scenario.

The continuous sizing variables of the hybrid-electric aircraft could be reduced to the battery power split during take-off S_{TO} and the fraction between mass of the battery system and maximum take-off mass ξ_{Bat} of the aircraft. Consequently, optimized values for S_{TO} and ξ_{Bat} could be identified for different transport missions and combustion engines. In case of a 4-seat aircraft with a cruise speed of 120 knots (~220 km/h) and a range of 800 km, the fuel consumption can be lowered by 21 % compared to a modern reference aircraft, which is equipped with a state-of-the-art diesel engine. This was achieved by a battery mass fraction of $\xi_{Bat} = 0.108$ and a power split of $S_{TO} = 0.50$, which implies that 50 % of the take-off power is contributed by the battery system. The reduced fuel consumption is achieved although power and energy reserves are designed into the propulsion system in order to compensate a failure of the combustion engine during take-off and to provide a reserve of 89 km to mitigate the effects of a engine failure in cruise flight and to reach a suitable diversion airport. The application of a diesel engine leads to the lowest fuel consumption compared to a gasoline engine or a gas turbine.

Furthermore, a 9-seat aircraft with a cruise speed of 220 knots (~400 km/h) and a range of 3,200 km was investigated. It was shown that the fuel consumption can be lowered by 24 % through the application of a mass-optimized diesel engine. The corresponding, optimized values for power split and battery mass fraction are $S_{TO} = 0.51$

and $\xi_{Bat} = 0.089$. The lower required battery mass fraction is the result of a propulsion system which consists of two combustion engines, where in case of a failure of one combustion engine, one remaining engine can be used to contribute power and energy to reach a suitable airport for an emergency landing. If a conventional aviation diesel engine is applied in the 9-seat hybrid-electric aircraft, its increased engine mass leads to a significantly higher mass of the propulsion system, which is associated with further structural mass growth. Additionally, the parasitic aerodynamic drag of the aircraft increases, as larger wings and stabilizers are required and the induced drag grows due to the increased aircraft mass. As a consequence, the airplane possesses an fuel consumption which is only reduced by 9 %, compared to the conventional reference aircraft, which is equipped with a turbo-prop engine. In this case, the beneficial effect of the increased efficiency of the combustion engine and the beneficial effect of the propeller integration into the stabilizer of the aircraft is nearly compensated by the increased aircraft mass and the increased aerodynamic drag. Similar results were obtained for hybrid-electric propulsion systems consisting of gasoline engines or gas turbines.

As described, the data of existing propulsion components was applied in the sizing calculation of the hybrid-electric propulsion system. This approach aims to ensures a feasibility of the preliminary designed aircraft. In order to assess the impact of technology improvements of the propulsion components, a sensitivity study was carried out. A result of the study is, that an improvement of the efficiency of the electric machines contributed significantly to a fuel burn reduction, which can be explained by the presence of generator and electric motor in the hybrid-electric propulsion chain. Naturally, an improvement of the efficiency of the combustion engine led to an improved fuel consumption in the same order of magnitude. Hence, a possible improvement of the efficiency of a combustion engine, which is optimized for one operating point would lower the fuel consumption of the hybrid-electric aircraft. In addition, the aircraft's fuel consumption is influenced by the required range of 89 km after a failure of a combustion engine in cruise flight, which was determined by an evaluation of the location of suitable diversion airports in Europe and the USA. If a lower range can be justified by certification considerations, a lower fuel consumption could be achieved as a result of the lighter propulsion system.

A factor of uncertainty is the remaining structural empty mass of the aircraft. The mass growth of the individual structural components was evaluated with statistical equations from literature with respect to changed aircraft parameters such as maximum take-off mass, fuel mass and reference area of wing and stabilizers. In a possible realization of the proposed hybrid-electric aircraft, a focus should be set to reduce the structural empty mass, as it has a significant impact on the fuel consumption. In a further investigation possible beneficial effects to reduce structural mass could be addressed by e.g. installing battery systems in the wing structure to relief wing bending and thereby reducing structural mass.

Bibliography

[1] Specification for NCR18650GA. Technical report, Panasonic Corporation, 2015.

[2] E. Hahne. *Technische Thermodynamik: Einführung und Anwendung*. Oldenbourg Verlag, 2010. ISBN 978-3486592313.

[3] R. van Basshuysen. *Internal Combustion Engine Handbook*. SAE International, 2016. ISBN 978-0768080247.

[4] D. P. Raymer. *Aircraft Design: A Conceptual Approach*. American Institute of Aeronautics and Astronautics, 1992. ISBN 0-930403-51-7.

[5] F. Müller. *Flugzeugentwurf: Entwurfssystematik, Aerodynamik, Flugmechanik und Auslegungsparameter für kleinere Flugzeuge*. TFT-Verlag, 2003. ISBN 3-931776-19-0.

[6] Operators Manual for Rotax Engine Type 912 i Series. Technical report, BRP-Rotax GmbH & Co KG, 2015.

[7] M. Filipenko. Hybrid-electric Propulsion Systems for eVTOL and Fixed-wing Commuter Aircraft. In *e2 Symposium Stuttgart*, 2019.

[8] General Aviation Manufacturers Association. 2018 Annual Report.

[9] D. Scholz. *Skript zur Vorlesung - Flugzeugentwurf*. HAW Hamburg, 1999.

[10] B. Propfe, M. Redelbach, D. J. Santini, and H. Friedrich. Cost analysis of Plug-in Hybrid Electric Vehicles including Maintenance and Repair Costs and Resale Values. In *EVS26 International Battery, Hybrid and Fuel Cell Electric Vehicle Symposium*, 2012. doi: 10.3390/wevj5040886.

[11] M. H. Snyder and G. W. Zumwalt. *Effects of a Wingtip-mounted Propeller on Wing Lift and Induced Drag*. PhD thesis, Journal of Aircraft, 1969.

[12] J. C. Patterson and R. G. Bartelett. Evaluation of Installed Performance of a Wing-Tip-Mounted Pusher Turboprop on a Semispan Wing. Technical report, National Aeronautics and Space Administration, 1987.

[13] T. Sinnige, N. van Arnhem, T. Stokkermans, and G. Eitelberg. Wingtip-Mounted Propellers: Aerodynamic Analysis of Interaction Effects and Comparison with Conventional Layout. In *Journal of Aircraft*, 2018. doi: 10.2514/1.C034978.

[14] T. C. A. Stokkermans, S. Nootebos, and L. L. M. Veldhuis. Analysis and Design of a Small-Scale Wingtip-Mounted Pusher Propeller. In *AIAA Aviation 2019 Forum, Dallas*, 2019. doi: 10.2514/6.2019-3693.

[15] L. L. M. Veldhuis. Review of Propeller-Wing Aerodynamic Interference. In *24th International Congress of the Aeronautical Sciences*, 2004.

[16] M. D. Patterson, J. M. Derlaga, and N. K. Borer. High-Lift Propeller System Configuration Selection for NASA's SCEPTOR Distributed Electric Propulsion Flight Demonstrator. In *AIAA Aviation Technology, Integration, and Operations Conference, Washington, D.C.*, 2016. doi: 10.2514/6.2016-3922.

[17] K. A. Deere, J. K. Viken, S. A. Viken, M. B. Carter, and D. Cox. Computational Component Build-up for the X-57 Distributed Electric Propulsion Aircraft. In *AIAA SciTech 2018, Kissimmee*, 2018. doi: 10.2514/6.2018-1275.

[18] A. Bolonkin. A High Efficiency Fuselage Propeller ("Fusefan") for Subsonic Aircraft. In *SAE Technical Paper 1999-01-5569*, 1999. doi: 10.4271/1999-01-5569.

[19] A. Seitz and C. Gologan. Parametric design studies for propulsive fuselage aircraft concepts. In *CEAS Aeronautical Journal*, 2015. doi: 10.1007/s13272-014-0130-3.

[20] R. H. Jansen, M. L. Celestina, and H. D. Kim. Electrical Propulsive Fuselage Concept for Transonic Transport Aircraft. Technical report, National Aeronautics and Space Administration, 2019.

[21] L. Schumann. *Reduktion des Energiebedarfs mittels eines batterieelektrischen Antriebs am Beispiel eines Kleinflugzeugs.* PhD thesis, University of Stuttgart, 2017.

[22] N. K. Borer, M. D. Patterson, J. K. Viken, M. D. Moore, S. Clarke, M. E. Redifer, R. J. Christie, A. M. Stoll, A. Dubois, J. Bevirt, A. R. Gibson, T. J. Foster, and P. G. Osterkamp. Design and Performance of the NASA SCEPTOR Distributed Electric Propulsion Flight Demonstrator. In *AIAA Aviation Technology, Integration, and Operations Conference, Washington, D. C.*, 2016. doi: 10.2514/6.2016-3920.

[23] J. Ludowicy, R. Rings, F. D. Finger, C. Braun, and C. Bil. Impact of Propulsion Technology Levels on the Sizing and Energy Consumption for Serial Hybrid-Electric General Aviation Aircraft. In *Asia Pacific International Symposium on Aerospace Technology*, 2019.

[24] G. Atanasov, J. van Wensveen, F. Peter, and T. Zill. Electric Commuter Transport Concept Enabled by Combustion Engine Range Extender. In *German Aerospace Congress*, 2019.

[25] K. R. Antcliff and F. M. Capristan. Conceptual Design of the Parallel Electric-Gas Architecture with Synergistic Utilization Scheme (PEGASUS) Concept, 18th AIAA/ISSMO Multidisciplinary Analysis and Optimization Conference. 2017. doi: 10.2514/6.2017-4001.

[26] J. Hoelzen, Y. Liu, B. Bensmann, C. Winnefeld, A. Elham, J. Friedrichs, and R. Hanke-Rauschenbach. Conceptual Design of Operation Strategies for Hybrid Electric Aircraft. *Energies*, 2018. doi: 10.3390/en11010217.

[27] Martin Hepperle. Electric Flight - Potential and Limitation. *STO-MP-AVT-209*, 2012.

[28] D. Urban and J. Mayerl. *Angewandte Regressionsanalyse: Theorie, Technik und Praxis.* Springer VS, 2018. ISBN 978-3-658-01915-0.

[29] *Luftfahttechnisches Handbuch*, chapter Anwendung der Regressions- und Korrelationsanalyse.

[30] L. Fahrmeir, T. Kneib, S. Lang, and B. Marx. *Regression - Models, Methods and Applications.* Springer, 2013. ISBN 978-3-642-34333-9.

[31] J. Frost. *Regression Analysis: An Intuitive Guide for Using and Interpreting Linear Models.* 2019. ISBN 978-1735431185.

[32] G.E. Welch, D. E. Paxson, J. Wilson, and P. H. Snyder. Wave-Rotor-Enhanced Gas Turbine Engine Demonstrator. Technical report, Nasa Glenn Research Center, 1999.

[33] Avions de Transport Regional. ATR: The Optimum Choice for a Friendly Environment. Technical report, Avions de Transport Regional, 2001.

[34] PT6 Exceeds Its Estimated Performance. *Aviation Week and Space Technology*, 1961.

[35] W. H. Press, S. A. Teukolsky, W. T. Vetterling, and B. P. Flannery. *Numerical Recipes in C: The Art of Scientific Computing.* Cambridge University Press, 2007. ISBN 978-0521880688.

[36] H. G. Münzberg. *Flugantriebe - Grundlagen, Systematik und Technik der Luft- und Raumfahrtantriebe.* Springer-Verlag, 1972. ISBN 978-0387056265.

[37] H.I.H. Saravanamuttoo, G.F.C. Rogers, and H. Cohen. *Gas Turbine Theory.* Pearson Education, Ltd., 2001. ISBN 978-81-7758-902-3.

[38] J. Welc and P. J. Rodriguez Esquerdo. *Applied Regression Analysis for Business: Tools, Traps and Applications.* Springer International Publishing, 2018. ISBN 978-3-319-71156-0.

[39] *Aerospace Source Book 2009.* Aviation Week & Space Technology, 2009.

[40] Élodie Roux. *Turboshaft, Turboprop & Propfan - Database Handbook.* lulu.com, 2011. ISBN 978-2-9529380-3-7.

[41] J. D. Anderson, Jr. *Aircraft Performance and Design.* WCB/McGraw-Hill, 1999. ISBN 0-07-001971-1.

[42] M. Saarlas. *Aircraft Performance.* John Wiley & Sons, 2007. ISBN 978-0-470-04416-2.

[43] Deutscher Wetterdienst. ICAO-Standardatmosphäre (ISA). Technical report, 2020.

[44] H. Sigloch. *Technische Fluidmechanik.* Springer Vieweg, 2017. ISBN 978-3-662-54466-2.

[45] Safran S.A. Compression ignition engines for aeronautical applications, 2020. URL `https://www.smaengines.com/our-product/hpde`.

[46] J. Roskam. *Airplane Design: Part V - Component Weight Estimation.* DARcorporation, 2017. ISBN 978-1-118-41478-1.

[47] AE300 Key Benefits. Technical report, Austro Engines GmbH, 2019.

[48] Detailed Technical Description of Turbo Diesel Aircraft Engine Centurion 2.0s. Technical report, Continental Motors, Inc., 2013.

[49] W. Eifler, E. Schlücker, U. Spicher, and G. Will. *Küttner Kolbenmaschinen.* Vieweg+Teubner, 2009. ISBN 978-3-8351-0062-6.

[50] P. R. Hakenesch. *Technische Thermodynamik.* Lecture Notes - Munich University of Applied Sciences, 2020.

[51] W. Geller. *Thermodynamik für Maschinenbauer.* Springer Berlin Heidelberg, 2006. ISBN 978-3-540-32320-4.

[52] E. Götsch. *Luftfahrzeug-Technik.* Motorbuch Verlag, 2003. ISBN 978-3-613-02006-1.

[53] K. Mollenhauer and H. Tschoeke. *Handbook of Diesel Engines.* Springer-Verlag Berlin Heidelberg, 2010. ISBN 978-3-540-89083-6.

[54] TSIO-550-B/C/E/G Installation and Operation Manual. Technical report, Continental Motors, Inc., 2006.

[55] TEO-540-C1A Engine Installation and Operation Manual. Technical report, Lycoming Engines, 2018.

[56] D. Doerffel and S. Abu Sharkh. A critical review of using the Peukert equation for determining the remaining capacity of lead-acid and lithium-ion batteries. *Journal of Power Sources*, 155, 2005. doi: 10.1016/j.jpowsour.2005.04.030.

[57] R. Korthauer, editor. *Handbuch Lithium-Ionen-Batterien.* Springer Vieweg, 2013. ISBN 978-3-642-30652-5.

[58] J. Jiang and C. Zhang. *Fundamentals and Application of Lithium-ion Batteries in Electric Drive Vehicles.* John Wiley & Sons Singapore Pte. Ltd., 2015. ISBN 978-1-118-41478-1.

[59] R. Bugga, C. Krause, K. Billings, J. P. Ruiz, E. Brandon, E. Darcy, and C. Iannello. Performance of Commercial High Energy and High Power Li-Ion Cells in Jovian Missions Encountering High Radiation Environments. In *NASA Battery Workshop*, 2019.

[60] L. William. *Fundamentals of Geophysics.* Cambridge University Press, 2007. ISBN 978-05-2185-902-8.

[61] T. Danner, M. Singh, S. Hein, J. Kaiser, H. Hahn, and A. Latz. Thick electrodes for Li-ion batteries: A model based analysis. *Journal of Power Sources*, (334): 191–201, 2016. doi: 10.1016/j.jpowsour.2016.09.143.

[62] J. Roskam. *Airplane Design: Part I - Preliminary Sizing of Airplanes.* DARcorporation, 2015. ISBN 978-1884885426.

[63] M. Ceraolo and G. Pede. Techniques for estimating the residual range of an electric vehicle. *IEEE Transactions on Vehicular Technology*, 2001. doi: 10.1109/25.917893.

[64] J.-M. Kang, S. Seo, and J. W. Hong. Personalized Battery Lifetime Prediction for Mobile Devices based on Usage Patterns. *Journal of Computing Science and Engineering*, 2011. doi: 10.5626/JCSE.2011.5.4.338.

[65] G. Müller, K. Vogt, and B. Ponick. *Berechnung elektrischer Maschinen.* Wiley - VCH Verlag, 2008. ISBN 3-527-40525-9.

[66] X. Ding, J. Cheng, and F. Chen. Impact of Silicon Carbide Devices on the Powertrain Systems in Electric Vehicles. *Energies*, 2017. doi: 10.3390/en10040533.

[67] DMC5 - High Power Inverter. Technical report, Brusa Elektronik AG, 2015.

[68] magniX Technologies Pty Ltd. magnidrive, August 2019. URL `www.magnix.aero`.

[69] B. Weigand and J. v. Wolfersdorf. *Wärmeübertragung.* University of Stuttgart, 2007.

[70] Automotive products - RADOX cables and system solutions. Technical report, Huber + Suhner GmbH, 2018.

[71] F. Mitschke. *Fiber Optics.* Springer Verlag, 2016. ISBN 978-3-662-52762-7.

[72] Datenblatt E-Kupfer. Technical report, Isabellenhütte Heusler GmbH & Co. KG, 2014.

[73] Kilovac EV200 Series Contactor With 1 Form X (SPST-NO) Contacts Rated 500+ Amps, 12-900 Vdc. Technical report, TE Connectivity Ltd., 2019.

[74] Gigavac 1000V GV350 Series Automotive Contactor. Technical report, Sensata Technologies, Inc., 2018.

[75] High-Voltage Connector Systems. Technical report, Rosenberger Hochfrequenztechnik GmbH & Co. KG, 2019.

[76] Type-Certificate Data Sheet: No.: P.001 MTV-16-1. Technical report, EASA, 2007.

[77] Type-Certificate Data Sheet: No. IM.P.133 for HC-D4, HC-E4 series propellers. Technical report, EASA, 2018.

[78] S. Gudmundsson. *General Aviation Aircraft Design: Applied Methods and Procedures*. Butterworth-Heinemann, 2014. ISBN 978-0-12-397308-5.

[79] D. Stinton. *The Design of the Aeroplane*. BSP Professional Books, 1993. ISBN 0-632-01877-1.

[80] J. Dankert and H. Dankert. *Technische Mechanik*. Teubner Verlag, 2006. ISBN 3-8351-0006-8.

[81] Egbert Torenbeek. *Synthesis of subsonic airplane design*. Delft University Press, 1976. ISBN 90-247-2724-3.

[82] B. W. McCormick. *Aerodynamics, Aeronautics and Flight Mechanics*. John Wiley & Sons, Inc., 1995. ISBN 978-0471110873.

[83] BRP-Rotax. Operator Manual for Rotax Engine Type 912i Series. Technical report, BRP-Rotax, 2012.

[84] Korff Luftfahrt. Flight Manual Taifun 17 EII. Technical report, Korff Luftfahrt, 2006.

[85] Shark.Aero. Shark Performance Data Sheet. Technical report, Shark.Aero, 2012.

[86] Laurence K. Loftin. *Subsonic Aircraft - Evolution and the Matching of Size to Performance*. National Aeronautics and Space Administration, 1980.

[87] European Commission. Commission Regulation (EU) No 965/2012, October 2012.

[88] National Business Aviation Association. NBAA Management Guide. Technical report, 2011.

[89] openAIP - Worldwide aviation database, December 2019. URL `www.openaip.net`.

[90] I. Agricola and T. Friedrich. *Elementargeometrie*. Springer Spektrum, 2015. ISBN 978-3-658-06730-4.

[91] D. B. Beringer. Automation in General Aviation: Responses of Pilots to Autopilot and Pitch Trim Malfunctions. In *Proceedings of the Human Factors and Ergonomics Society 40th Annual Meeting*, 1996.

[92] H. Watter. *Regenerative Energiesysteme - Grundlagen, Systemtechnik und Analysen ausgeführter Beispiele nachhaltiger Energiesysteme.* Springer Vieweg, 2019. ISBN 978-3-658-23487-4.

[93] Nachrichten für Luftfahrer Teil II - 37/00. Technical report, Deutsche Flugsicherung, 2000.

[94] M. Voskuijl, J. van Bogaert, and A. G. Rao. Analysis and design of hybrid electric regional turboprop aircraft. In *CEAS Aeronautical Journal*, volume 9, page 15–25, March 2018. doi: 10.1007/s13272-017-0272-1.

[95] Airplane Flight Manual DA 40 NG. Technical report, Diamond Aircraft GmbH, 2010.

[96] V. Quaschning. *Regenerative Energiesysteme, Technologie - Berechnung - Klimaschutz.* Carl Hanser Verlag München, 10 edition, 2019. ISBN 978-3-446-46113-0.

[97] DIN EN ISO 52000-1:2018-03 Energieeffizienz von Gebäuden - Festlegungen zur Bewertung der Energieeffizienz von Gebäuden - Teil 1: Allgemeiner Rahmen und Verfahren (ISO 52000-1:2017). Technical report, Beuth Verlag, 2018.

[98] G. Kalt. Primärenergiefaktoren von fossilen und erneuerbaren Energieträgern, Strom und Fernwärme im Zeitraum 2000 bis 2011. Technical report, Austrian Energy Agency, 2013.

[99] P. Icha and G. Kuhs. Entwicklung der spezifischen Kohlendioxidemissionen des deutschen Strommix in den Jahren 1990 - 2019. Technical report, Umweltbundesamt, 2019.

[100] Treibhausgasneutraler Verkehr 2050: Ein Szenario zur zunehmenden Elektrifizierung und dem Einsatz stromerzeugter Kraftstoffe im Verkehr. Technical report, Ökoinstitut e.V., 2013.

[101] Jane's Information Group. *Jane's All The World's Aircraft (1989-90).* Jane's Information Group, 1989. ISBN 978-0710608963.

[102] Pilot's Information Manual PC-12 Series 10 and 10A. Technical report, Pilatus Aircraft Ltd., 2010.

[103] J. Mangold, M. Lang, J. Stober, F. Ladwein, and F. Will. NASA/ DLR Design Challenge 2019 - HyBird Aircraft Concept. Technical report, University of Stuttgart, 2019.

[104] Type Certificate Data Sheet: No. E. 104 for Technify Motors GmbH Centurion 3.0 series engines. Technical report, EASA, 2017.

[105] Type Certificate Data Sheet: No. E.014 for Centurion 4.0 series engines. Technical report, EASA, 2015.

[106] Centurion Engines: Centurion retrofit kits for Cessna 172, 206, 340, 414, and Piper PA28. Technical report, Thielert Aircraft Engines GmbH, 2007.

[107] Type-Certificate Data Sheet: E.200 for Austro Engine E4 series engines. Technical report, EASA, 2019.

[108] AE300/AE330 Key Benefits. Technical report, Austro Engines GmbH.

[109] Spritverächter - Smart CDI Diesel von Flyeco. Technical report, Fliegermagazin 06/2013, 2013.

[110] Type Certificate Data Sheet: E.150 for RED A03 series engines. Technical report, EASA, 2018.

[111] RED A03 V12 6100 cc / 374 cu in. Technical report, RED aircraft GmbH, 2018.

[112] Type Certificate Data Sheet: No. EASA E.076 for Engine SR305 Series. Technical report, EASA, 2019.

[113] SR305 General Aviation Engines. Technical report, Safran S.A., 2018.

[114] SMA Debuts Its High Power Density Engine, 2016. URL `https://www.aviationpros.com/engines-components/aircraft-engines/piston-engines-parts/article/12232319/sma-debuts-its-high-power-density-engine`.

[115] IO-550-A/B/C/G/N/P/R Installation and Operation Manual. Technical report, Continental Motors, Inc., 2011.

[116] (L)IO-360-M1A Operation and Installation Manual. Technical report, Lycoming Engines, 2008.

[117] Operator's Manual O-360, HO-360, IO-360, AIO-360, HIO-360 & TIO-360 Series. Technical report, Lycoming Engines, 2005.

[118] IO-390-C Series Engine Installation and Operation Manual. Technical report, Lycoming Engines, 2017.

[119] Technical Information of LG 18650HG2 (3.0Ah). Technical report, LG Chem Mobile Battery Division, 2014.

[120] Introduction of INR18650-30Q. Technical report, Samsung SDI Co., Ltd., 2014.

[121] Technical Report of INR18650-35E. Technical report, Samsung SDI Co., Ltd., 2015.

[122] Lithium Ion Rechargeable Battery Technical Information, Model Number US18650VTC6. Technical report, Sony Corporation, 2015.

[123] Lithium Ion Rechargeable Battery Technical Information, Model Number US18650VC7. Technical report, Sony Corporation, 2016.

[124] Lithium Ion Rechargeable Battery Technical Information, Model Number US18650VTC5A. Technical report, Sony Corporation, 2015.

[125] magniX Technologies Pty Ltd. magni250, August 2019. URL `www.magnix.aero`.

[126] EMRAX d.o.o. Technical Data and Manual for EMRAX Motors / Generators V5.1. Technical report, 2018.

[127] HVLP Inverter Data Sheet. Technical report, Sevcon Inc., 2016.

[128] Gen4 Size 10 Data Sheet. Technical report, Sevcon Inc., 2016.

[129] Gen5 Size 7 & Size 9 Data Sheet. Technical report, Sevcon Inc., 2016.

[130] Manual Digitaler Drehstrom Servoverstärker BAMOCAR-PG-D3. Technical report, Unitek Industrie Elektronik GmbH, 2018.

[131] SAC51 Motor controller for vehicles and boats. Technical report, Piktronik d.o.o., 2019.

[132] F. Anton, O. Otto, J. Hetz, and T. Olbrechts. Siemens eAircraft - Disrupting the way you fly! 2018.

[133] WaveSculptor 200 Motor Drive User's Manual. Technical report, Tritium Pty. Ltd., 2012.

[134] emDrive H300 BLDC motor controller datasheet V1.7. Technical report, Emsiso d.o.o., 2019.

[135] MTV-1 Propeller-Kennblatt Nr. 32.130/53. Technical report, Luftfahrt-Bundesamt, 2002.

[136] MTV-17 Type Certificate EASA P.008. Technical report, EASA, 2005.

[137] MTV-20 Type Certificate EASA.P.100. Technical report, EASA, 2017.

[138] MTV-7 Musterzulassungsschein Nr.: 32.130/84. Technical report, Luftfahrt-Bundesamt, 1992.

[139] MTV-18 Musterzulassungsschein Nr.: 32.130/75. Technical report, Luftfahrt-Bundesamt, 1990.

[140] MTV-10 Musterzulassungsschein Nr.: 32.130/77. Technical report, Luftfahrt-Bundesamt, 1991.

[141] MTV-25 Musterzulassungsschein Nr.: 32.130/97. Technical report, Luftfahrt-Bundesamt, 1997.

[142] MTV-27 Type Certificate EASA.P.104. Technical report, EASA, 2014.

[143] MTV-5 Musterzulassungsschein Nr.: 32.130/103. Technical report, EASA.

[144] MTV-36 Type Certificate EASA.P.044. Technical report, EASA, 2015.

[145] MTV-22 Musterzulassungsschein Nr.: 32.130/82. Technical report, Luftfahrt-Bundesamt, 1991.

[146] MTV-16 Type Certificate EASA.P.001. Technical report, EASA, 2007.

[147] MTV-14 Type Certificate EASA.P.017. Technical report, EASA, 2006.

[148] MTV-34 Type Certificate EASA.P.049. Technical report, EASA, 2013.

[149] MTV-12 Type Certificate EASA.P.013. Technical report, EASA, 2005.

[150] MTV-9 Propeller-Kennblatt Nr. 32.130/65. Technical report, Luftfahrt-Bundesamt, 2003.

[151] MTV-6 Type Certificate EASA.P.094. Technical report, EASA, 2008.

[152] MTV-21 Type Certificate EASA.P.101. Technical report, EASA, 2019.

[153] MTV-15 Type Certificate EASA.P.098. Technical report, EASA, 2017.

[154] MTV-11 Type Certificate EASA.P.007. Technical report, EASA, 2005.

[155] Type Certificate No. IM.P.133 for HC-D4, HC-E4 series propellers. Technical report, EASA, 2018.

[156] Type Certificate Data Sheet P8BO. Technical report, U.S. Department of Transportation Federal Aviation Administration, 1995.

[157] Type Certificate Data Sheet P7NE. Technical report, U.S. Department of Transportation Federal Aviation Administration, 2002.

Appendix A

Additional plots

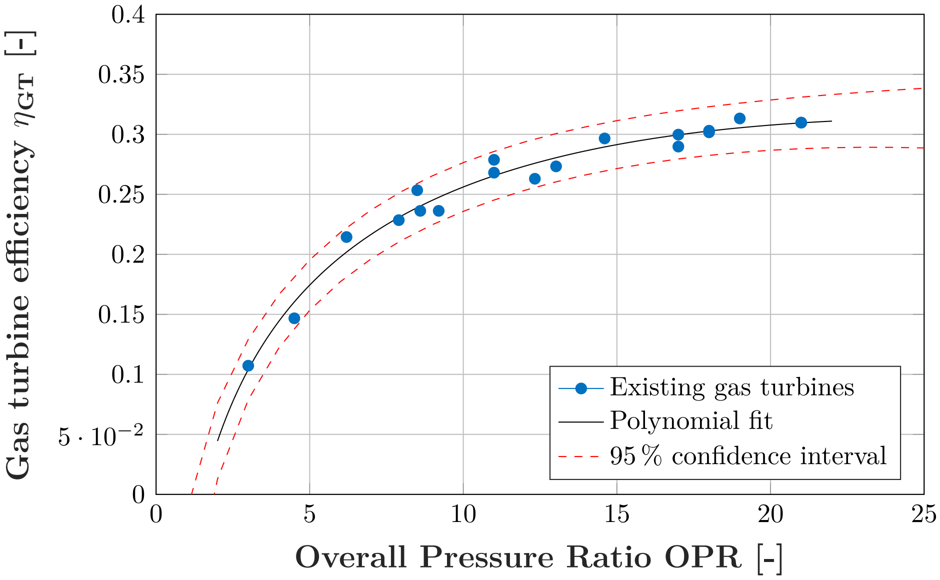

Figure A.1: Engine efficiency at sea level plotted over corresponding overall pressure ratio of considered turboshaft engines

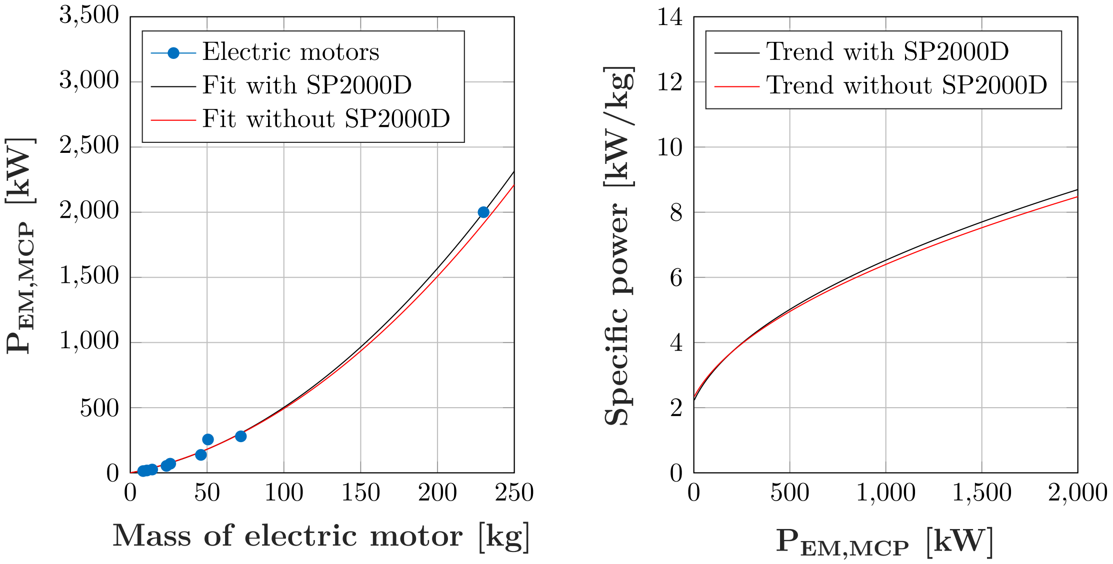

Figure A.2: Influence of the electric motor SP2000D on the mass trend curve

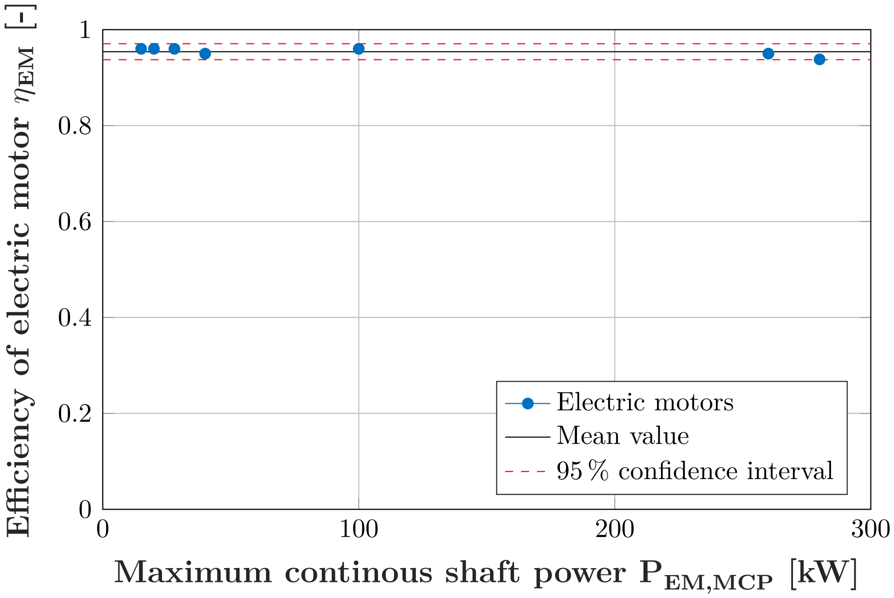

Figure A.3: Efficiency plotted of power of investigated electric motors

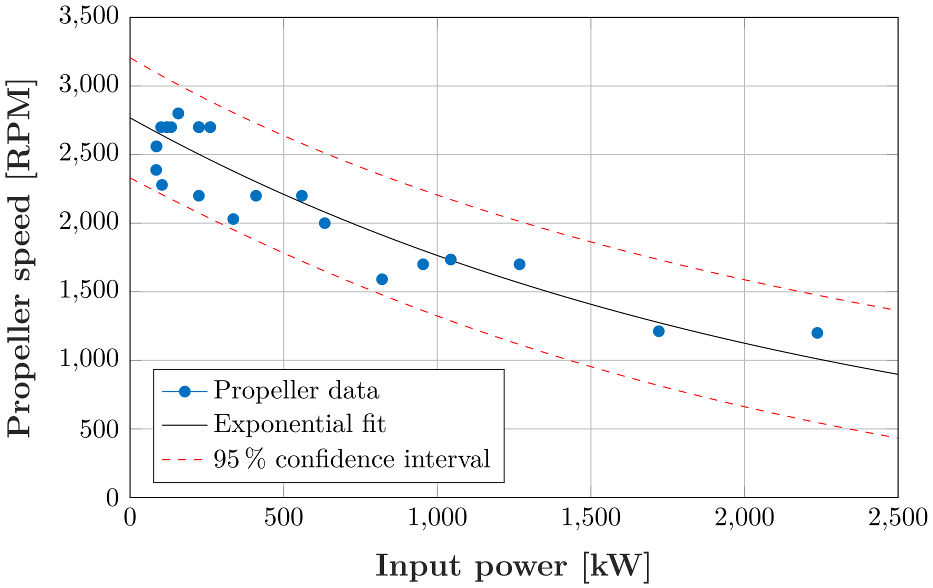

Figure A.4: Revolution at highest power rating plotted over corresponding power

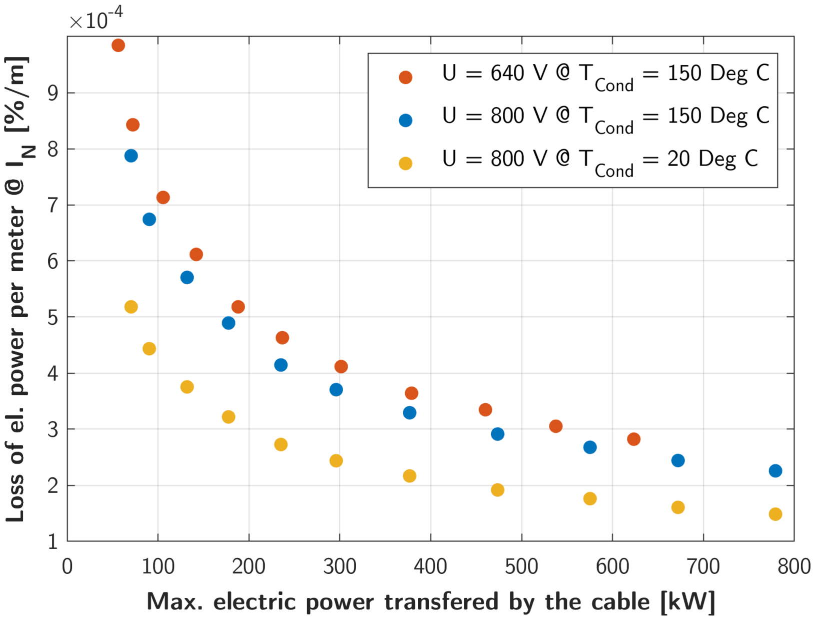

Figure A.5: Loss of electric power per meter expressed as a fraction of the maximum rated power at two different voltage levels and two different conductor temperatures

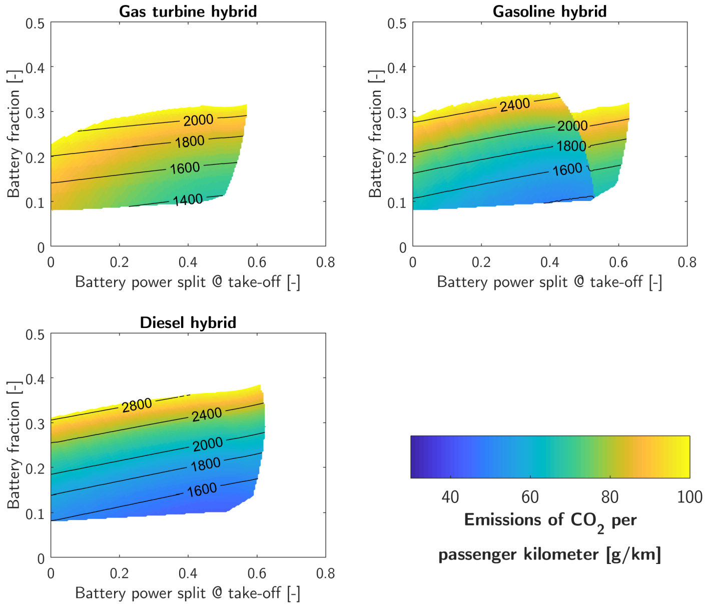

Figure A.6: Total CO_2 emissions for an evaluation range of 800 km considering CO_2 emissions for German electricity in 2019

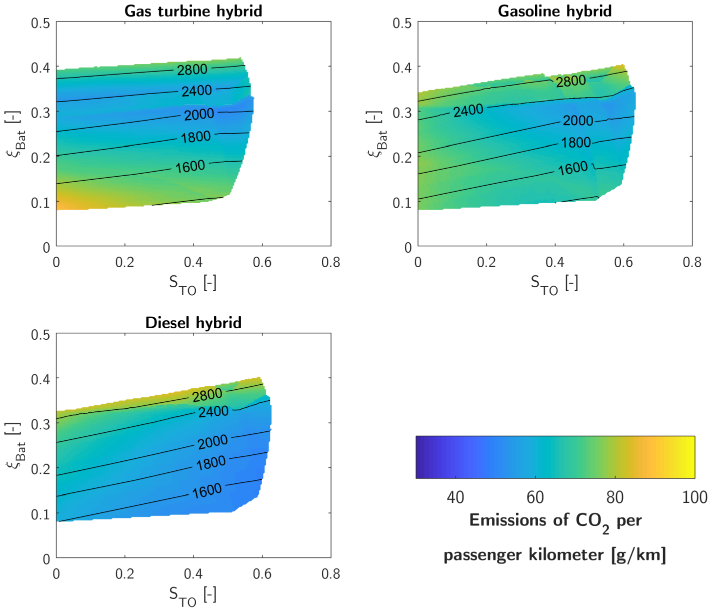

Figure A.7: Total CO_2 emissions for an evaluation range of 200 km considering CO_2 emissions for German electricity in 2019

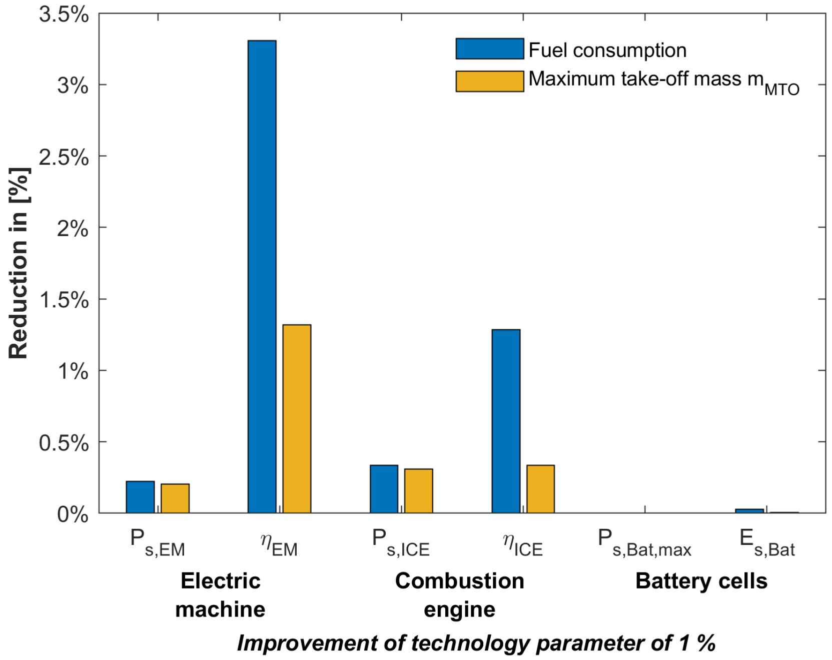

Figure A.8: Impact of technology improvements on fuel burn and MTOM of hybrid-electric aircraft with installed conventional diesel engine

Appendix B

Additional tables

Gas turbine	**EIS** [year]	**OPR** [-]	$\boldsymbol{P_{max}}$ [kW]	$\boldsymbol{\eta_{ICE,max}}$ [-]	**Mass** [kg]
General Electric T700-GE-700	-	17	1193	0.300	198
General Electric CT7-2A	1981	17	1269	0.290	195
General Electric T700-GE-401C	1976	18	1324	0.303	208
General Electric T700-GE-701C	1973	18	1390	0.302	207
General Electric T700/T6A1	1973	19	1578	0.313	224
General Electric CT7-8	2000	21	1853	0.310	244
General Electric CT7-8E	2004	21	1859	0.310	246
Jakadofsky PRO X	2000	3	10	0.107	4
LHTEC CTS800-4N/4K	2003	14.6	1001	0.297	185
Mitsubishi TS1-M-10	1998	11	691	0.268	152
Mitsubishi CT63-M-5A	1961	6.2	233	0.214	63
Mitsubishi MG5-110	1999	11	644	0.279	154
Rolls Royce Gem 42	1987	13.02	824	0.273	183
Rolls Royce Model 250-C20R	1989	7.9	331	0.228	78
Rolls Royce Model 250-C30L/P/R/S/U	1983	8.6	478	0.236	114
Rolls Royce Model 250-C30R/3	1997	9.2	478	0.236	124
Rolls Royce Gem 1004	1983	12.33	749	0.263	167
Safran Arrius 2F	1997	8.5	371	0.253	103

Table B.1: Data of the investigated gas turbines from [39] and [40]

Diesel engine	$\boldsymbol{P_{max}}$ **[kW]**	$\boldsymbol{\eta_{ICE,max}}$ **[-]**	**Wet mass [kg]**	**Comp. ratio***	**Source**
Continental CD-155	114	39.6 %	173	15.5	[48]
Continental CD-300	221		271†	15.5	[104]
Continental Centurion 4.0	257	39.2 %	313†	18.5	[105] [106]
Austo Engines AE330	132	42.8 %	199†	17.5	[107] [108]
Flyeco OM660	50	40.4 %	89	18.5	[109]
Lycoming DEL-120	153	40.4 %	183†	16.5	
RED Aircraft A03	368	40.4 %	403†		[110] [111]
SMA SR305	196	38.5 %	222†	15	[112] [113]
SMA HPDE	597	40.4 %	288		[45] [114]

Table B.2: Data of the investigated diesel engines (* = compression ratio; †= engine fluids estimated)

Petrol engine	**TC***	**ECU**	$\boldsymbol{P_{max}}$ **[kW]**	**Mass [kg]**	$\boldsymbol{\eta_{ICE,max}}$ **[-]**	**Comp. ratio**	**Source**
Cont. IO-550-N	-	yes	231	204	0.37	9.0	[115]
Cont. TSIO-550-E	yes	yes	261	257	0.37	7.5	[54]
Cont. TSIO-550-C	yes	yes	231	237	0.37	7.5	[54]
Ly. IO-360-M1A	-	no	134	136	0.35	8.5	[116]
Ly. IO-360-L2A	-	no	119	126	0.36	8.5	[117]
Ly. IO-390-C	-	no	157	136	0.36	8.9	[118]
Ly. i2 TEO-540-C1A	yes	yes	280	251	0.34	7.3	[55]
Rotax 912 iS Sport	-	yes	73.5	72	0.36	10.8	[6]

Table B.3: Data of the investigated petrol engines (* = turbo charger)

Brand	**Cell**	**Nominal capacity**	**Max. discharge current***	**Source**
LG	18650 HG2	3,000 mAh	20 A	[119]
Panasonic	NCR18650GA	3,450 mAh	10 A	[1]
Samsung	18650-30Q	3,000 mAh	15 A	[120]
Samsung	INR18650-35E	3450 mAh	8 A	[121]
Sony/Murata	US18650 VTC6	3,120 mAh	30 A	[122]
Sony/Murata	US18650 VC7	3,500 mAh	8 A	[123]
Sony/Murata	US18650 VTC5D	2,800 mAh	35 A	[124]

Table B.4: Data of the investigated battery cells (* = maximum continuous)

Brand	**Battery cell**	$\boldsymbol{R^2}$	**Error in predicted** $\boldsymbol{E_{s,Bat,max}}$
LG	18650 HG2	0.921	2.2 %
Panasonic	NCR18650GA	0.970	-0.4 %
Samsung	18650-30Q	0.937	0.4 %
Samsung	INR18650-35E	0.986	0.4 %
Sony/Murata	US18650 VTC6	0.975	1.0 %
Sony/Murata	US18650 VC7	0.982	-1.0 %
Sony/Murata	US18650 VTC5D	0.986	-1.3 %

Table B.5: Coefficient of determination R^2 and error in predicted $E_{s,Bat,max}$ for investigated battery cells

Electric machine	$\boldsymbol{P_{MCP}}$ **[kW]**	**RPM [-]**	**Mass [kg]**	$\boldsymbol{\eta_{EM,max}}$ **[-]**	**Prop. flange**	**Source**
MagniX Magni250	280	1900	72	0.938	yes	[125]
Emrax 188	15	3000	7.3	0.96	no	[126]
Emrax 208	20	3000	9.4	0.96	no	[126]
Emrax 228	28	3000	12.4	0.96	no	[126]
Emrax 268	60	3000	20.5	0.95	no	[126]
Emrax 348	150	2800	40	0.96	no	[126]
Siemens SP70D	70	2600	26	-	yes	[7]
Siemens SP260D-A	260	2500	44	0.95	no	[7]
Siemens SP2000D	2000	-	200	-	-	[7]

Table B.6: Data of the investigated electric motors

Flight phase	**Torque [%]**	**Revolution speed [RPM]**	**Efficiency** η_{EM} **[-]**
Take-off	70	2000	0.937
Climb	60	1600	0.938
Cruise	30	1200	0.945

Table B.7: Efficiency in specific operating points during flight of the synchronous electric machine Sineton A0911 applied in the electric aircraft e-Genius

Inverter	$\boldsymbol{U_{max}}$ **[V]**	**Max. cont. current [I]**	$\boldsymbol{P_{MCP}}$ **[kW]**	**Mass [kg]**	**Source**
Sevcon HVLP-20	800	33	26*	2.30	[127]
Sevcon Gen4 Size10	800	200	150	10.90	[128]
Sevcon Gen5 Size9	450	200	90*	6.80	[129]
Unitek Bamocar-PG-D3	700	200	140*	8.50	[130]
Piktronic SAC52-510-HP	444	400	205	14.70	[131]
Siemens NextGen Si	450	250	130	9.80	[132]
Tritium WaveSculptor 200	450	-	107	8.50	[133]
Emsiso emDrive H300	450	300	135	7.50	[134]
MagniX MagniDrive	800	-	170	12.00	[68]

Table B.8: Data of the investigated inverters ($*$ = estimated values)

Component	**Mass**
AKG heat exchanger	1.1 kg
CWA50 pump	1.0 kg
Silicon hoses (approx. 2 m length)	0.3 kg
Equalizing tank	0.3 kg
Cooling fluid	2 kg

Table B.9: Approximate mass of cooling system components for the electric motor Sineton A0911 and its inverter which are applied in the electric aircraft "e-Genius"

Name	**Power [kW]**	**Mass [kg]**	**RPM**	**Dia. [cm]**	**Material**	**Source**
MT MTV-1	85	11	2388	180	Natural Comp.*	[135]
MT MTV-17	120	16	2700	190	Natural Comp.	[136]
MT MTV-20	224	21	2700	210	Natural Comp.	[137]
MT MTV-7	101	14,5	2700	190	Natural Comp.	[138]
MT MTV-18	224	20	2700	203	Natural Comp.	[139]
MT MTV-10	157	17.5	2800	174	Natural Comp.	[140]
MT MTV-25	261	25.5	2700	170	Natural Comp.	[141]
MT MTV-27-J	1268	68	1700	300	Natural Comp.	[142]
MT MTV-5	410	39	2200	220	Natural Comp.	[143]
MT MTV-36	86	11.5	2560	180	Natural Comp.	[144]
MT MTV-22	157	17	2800	175	Natural Comp.	[145]
MT MTV-16	954	45	1700	270	Natural Comp.	[146]
MT MTV-14	261	30	2700	195	Natural Comp.	[147]
MT MTV-34-1	86	9.5	2560	178	Natural Comp.	[148]
MT MTV-12	224	25	2700	203	Natural Comp.	[149]
MT MTV-9	336	29	2030	250	Natural Comp.	[150]
MT MTV-6	134	17.5	2700	160	Natural Comp.	[151]
MT MTV-21	104	12	2279	203	Natural Comp.	[152]
MT MTV-15	224	25	2200	260	Natural Comp.	[153]
MT MTV-11	120	16	2700	190	Natural Comp.	[154]
Hartzell E10950	1044	59.9	1735	279	Aramid Comp.	[155]
Hartzell E8190	559.3	54.4	2200	208	Aramid Comp.	[155]
Hartzell NC9208+2	633.8	52.2	2000	241	Carbon Comp.	[155]
Hartzell NC10904-0	820.3	60.8	1591	279	Carbon Comp.	[155]
Hamilton Std. 568F-1	2237	159	1200	198	Kevlar/Graphite	[156]
Hamilton Std. 14SF	1721	142	1212	198	Fiberglass/alu.	[157]

Table B.10: Data of the investigated propellers (* = composite)

Parameter	Symbol	Value	Source
Specific air range	$\frac{\Delta R}{\Delta m_{Fuel}}$	0.78 nm/lb	[102]
Aircraft weight at cruise	m_{Cruise}	4717 kg	[102]
Cruise speed (TAS)	v_{Cruise}	220 knots	[102]
Cruise altitude	-	30000 ft	[102]
Efficiency PT6A-67B, 0 ft	$\eta_{ICE,0ft}$	0.25	[101]
Efficiency PT6A-67B @ 30000 ft	η_{ICE}	0.29	[41]

Table B.11: Data of the PC-12 NG from flight manual

Component	Design variable	Reference value	Req. improvement for 1 % reduction in fuel burn
Electric machine	$P_{s,EM}$	3.84 $^{kW}/_{kg}$	4.5 %
	η_{EM}	0.94	0.3 %
Combustion engine	$P_{s,ICE}$	2.00 $^{kW}/_{kg}$	3.0 %
	η_{ICE}		0.8 %
Battery system	$P_{s,Bat,max}$	2.449 $^{kW}/_{kg}$	Inf
	$E_{s,Bat}$	216 $^{Wh}/_{kg}$	36.9 %

Table B.12: Trade-off for component design parameters on hybrid-electric aircraft with installed conventional diesel engines